A Thesis Submitted for the Degree of PhD at the University of Warwick

Permanent WRAP URL:

http://wrap.warwick.ac.uk/153849

warwick.ac.uk/lib-publications

Numerical Modelling of Waves
in the Solar Atmosphere

Jamon D. Pennicott

B. Sc. (Hons)

Numerical Modelling of Waves
in the Solar Atmosphere

A thesis submitted in fulfilment of the requirements for the joint degree of
Doctor of Philosophy

by

Jamon D. Pennicott

B. Sc. (Hons)

School of Mathematics
Monash Centre for Astrophysics
Monash University
Australia

Centre for Fusion, Space and Astrophysics
University of Warwick
United Kingdom

Main Supervisors: Prof. Paul S. Cally & Prof. Tony D. Arber
Co Supervisors: Dr. Alina C. Donea & Prof. Valery M. Nakariakov

May 2020

Copyright notice

Abstract

The Sun is the closest star to Earth and the bringer of life for all of us. Remove the Sun and Earth is rendered a lifeless, icy rock floating in outer space. It stands to reason that a thorough understanding of the workings of the Sun would be high priority in the scientific world, and beyond. The outer-most layer of the interior of the Sun comprises of what is known as the convection zone. This chaotic zone produces innumerable pressure waves, which propagate through the Sun. These waves carry the energy of the Sun to its atmosphere and beyond, and are thought to be responsible for the infamous 'coronal heating problem'. The magnetic nature of the Sun allows both acoustic and magnetic waves, or various combinations of the two, to exist. This is where the complexity lies, with so many different types of waves being produced and exchanging energy between themselves, it is extremely difficult to pinpoint which waves are responsible for the observations we make.

Observations and mathematical/physical theories of ever improving quality are used to understand the details of waves in the Sun, however they often lack a bridge to connect them, which is where numerical simulations come in. The work presented here provides a combination of 1.5, 2.5 and 3 dimensional simulations looking to explain how a variety of waves propagate and carry energy through the internal and external layers of the Sun.

When a wave reaches a layer in the Sun's atmosphere where the sound and Alfvén speeds coincide, it splits into two 'modes', a fast and slow mode. Recent mathematical findings suggested an incoming shock wave would not only split into its fast and slow components, but that both wave modes would be smoothed as they exit this area. Numerical simulations herein show that only the slow wave is smoothed, with the fast wave propagating unhindered.

Within the Sun's atmosphere, various steep gradients of its physical components are found. These gradients have been proposed to act as barriers to incoming waves, which can be partially reflected off them. Multiple reflection sites suggests cavities can be created that acoustic waves can resonate within. Numerical simulations herein show a stark increase in the velocity of frequencies proposed to be characteristic of a cavity within the chromosphere. This suggests cavities can exist within the Sun's atmosphere and the amplitude of velocity observations from within these areas must be partially attributed to the resonant effects of the cavities themselves.

Following the onset of some solar flares, ripples are observed on the Solar surface emanating from the flare site. These ripples show strong anisotropies in their appearance, a characteristic not well studied. Numerical simulations herein show that these anisotropies can be attributed to both the strength and inclination of the magnetic field but even more so by the nature of the impacting source. A source with motion perpendicular to the solar surface causes constructive interference and higher amplitude ripples are created along the axis of motion.

Declaration

I hereby declare that this thesis contains no material which has been accepted for the award of any other degree or diploma at any university or equivalent institution and that, to the best of my knowledge and belief, this thesis contains no material previously published or written by another person, except where due reference is made in the text of the thesis.

This thesis includes (1) original paper published in peer reviewed journals and (2) manuscripts in preparation or submitted status. The core theme of the thesis is Numerical Modelling of Waves in the Solar Atmosphere. The ideas, development and rewriting up of all the papers in the thesis were the principal responsibility of myself, the student, working within the School of Mathematics, Monash University, and the School of Physics, University of Warwick, under the supervision of Prof. Paul S. Cally, Prof. Tony D. Arber, Dr. Alina C. Donea and Prof. Valery M. Nakariakov.

The inclusion of co-authors reflects the fact that the work came from active collaboration between researchers and acknowledges input into team-based research.
My contribution to the work involved the following:

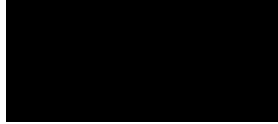| (1)	(2)	(3)	(4)	(5)	(6)
2	Smoothing of MHD Shocks in Mode Conversion	Published in Astrophysical Journal Letters	60%: numerical work; draft writing;	Prof. P. Cally 40%: concept; draft writing and review.	no
3	Chromospheric Resonances in Sunspot Umbrae	Not Submitted	80%: concept development; numerical work; draft writing;	Prof. T. Arber 20%: concept; draft revisions; discussions	no
4	Anisotropies of Solar Quakes	Not submitted	70%: concept development; numerical work; draft writing	Dr. Alina Donea 20%: concept; draft revision; discussions Prof. Paul Cally 10%: theoretical work; discussions	no

*(1) Thesis Chapter; (2) Publication Title; (3) Publication Status; (4) Student's nature and % of contribution; (5) Co-authors nature and % of contribution; (6) Monash student co-author.

I have rewritten, reordered, and renumbered sections of submitted or published papers in order to generate a consistent presentation within the thesis.

Student Signature: ███████████   Date: October 5, 2020

The undersigned hereby certify that the above declaration correctly reflects the nature and extent of the student's and co-authors' contributions to this work. In instances where I am not the responsible author I have consulted with the responsible author to agree on the respective contributions of the authors.

Main Supervisor Signature: ████████   Date: October 5, 2020

Acknowledgements

I would like to thank my myriad of supervisors at both Monash University and University of Warwick: Prof. Paul S. Cally, Prof Tony D. Arber, Dr. Alina C. Donea, and Prof Valery M Nakariakov. A special extra thank you goes to my main supervisor Paul; there's no way I could have completed this body of work without his constant guidance and support and I'm forever grateful.

A further thank you goes to all my friends and family who have been there to support me along the way. Again, a special thank you must go out to my mum, there is no person in this world who has sacrificed as much as she has for me. Any and all of my achievements in life can surely be traced back to the love she has provided me with since day one.

Contents

CHAPTER 1

Introduction

This chapter aims to introduce the reader to the key topics, ideas and concepts needed to appreciate the research contained within. This work traverses through areas of the solar atmosphere that are significantly varied, not only in the physics that govern them but also in the way they are observed and modelled by researchers alike. Consequently, the overview provided in this chapter shall be kept brief and notably broad in scope. Owing to this, an introductory section is provided for each chapter, individually developed to give a greater insight into the particulars of each area of research. This chosen pathway aims to give the reader an initial appreciation of the work as a whole, whilst allowing each chapter to be viewed as individual pieces of work, if so desired. The numerical codes used to conduct the research are also presented at the end of this chapter. Brief overviews of each code are given, highlighting the main features and limitations imposed by each.

1.1 The Solar Atmosphere

The solar atmosphere has long been a key environment for studying the formation, evolution and impact of not only solar but also stellar magnetic fields. Its main advantage as a stellar atmosphere laboratory is its proximity to Earth, with the Sun being over 250 000 times closer than our next nearest star. Owing to this, and recent advances in observational technology, the solar surface and atmosphere are unique in being the only components of any star that can be currently resolved. A vast array of observed and/or theorised physical processes have long been linked to the solar magnetic field and thus its importance has long been recognised. However, there still remains a long thread of unanswered questions. What are the mechanisms which drive the solar dynamo thought to be responsible for generating the solar magnetic field? Why do we observe the appearance of an 11-year sunspot cycle? What causes the formation of various surface magnetic flux phenomena such as intergranular lanes or knots? And perhaps the biggest question of all, what role do magnetic fields play in heating the chromosphere and corona?

To answer some of these questions relies on an understanding of what is happening beneath the solar surface, beyond what even the highest resolution observations can meaningfully provide. This is generally tackled through the study of solar oscillations, a process known as helioseismology and similar to the more widely recognised geoseismology. These oscillations are observed at the surface whilst having been excited by natural convective motions in the outer layers of the solar interior. Helioseismology provides a proven method for measuring solar structure, subsurface flows and solar convection. Solar oscillations were first detected as far back as the early 1960s by Leighton et al. (1962) and later confirmed by Evans and Michard (1962a,b), but it wasn't until much later that these oscillations were used to infer information about the workings and structure of the solar interior (Stein and Leibacher, 1974; Deubner, 1975; Ulrich and Rhodes, 1977; Rhodes et al., 1977). From this spawned the two persisting strands of helioseismology that we know today - global helioseismology, which focuses on large scale global properties of the Sun, and local helioseismology, where smaller features in more complex areas are investigated.

The Sun oscillates in what are known as its three global modes. The acoustic p-modes, which have pressure as their dominant restoring force, the g-modes, which have buoyancy as their restoring force, and the f-modes, which are essentially surface gravity modes. The analysis of these modes gives rise to global helioseismology, of which has proven

invaluable in the search to peer deep into the structure and dynamics of the Sun. Long, uninterrupted observations of the Sun are needed to garner accurate estimates for the Sun's global eigenmode frequencies. A requirement which has seen the development of ground-based observation networks such as the Birmingham Solar Oscillation Network (BiSON) (Elsworth et al., 1991) and the Global Oscillation Network Group (GONG) (Hill et al., 1996), as well as space-borne observatories such as the Solar and Heliospheric Observatory (SoHO) (Domingo et al., 1995) and the Solar Dynamics Observatory (SDO) (Pesnell et al., 2012). Analysis of the myriad of observations collected over the last fifty or more years has led to the determination of sound-speed, density and adiabatic exponent profiles (Dziembowski et al., 1990; Basu and Antia, 1997; Turck-Chièze et al., 1997), the depth and elemental abundances of the convection zone (Christensen-Dalsgaard et al., 1991; Basu, 1998; Basu and Antia, 2004; Serenelli and Basu, 2010), interior differential rotation rates (Thompson et al., 2003), as well as shedding light on the infamous solar neutrino problem (Elsworth et al., 1990; Bahcall et al., 1997).

Local helioseismology on the other hand, concentrates on phenomena observed at much smaller scales and works in complement with global helioseismology. Its goal is to use a variety of techniques to interpret the full wave field at the surface, not just the eigenmode frequencies. It provides a three-dimensional viewpoint for the solar interior and is crucial in understanding large-scale flows, magnetic structures, and their inherent interactions. It is responsible for revealing the existence of meridional flows (Hathaway et al., 1996), vertical flows (Komm et al., 2004) and sunspot flows (Duvall et al., 1996), whilst also helping to reveal the source of solar quakes (Donea et al., 1999). It further revealed variability in the solar tachocline (Howe et al., 2000), as well as forming the basis for a host of solar dynamo models (Schuessler, 1981; Dikpati and Charbonneau, 1999; Nandy and Choudhuri, 2002).

One local helioseismology technique is helioseismic holography, the basic concept of which was first proposed by Roddier (1975) and derived much later in detail by Lindsey and Braun (1990). The premise is that that any wavefield observed at the solar surface can be used to infer the wavefield at any other location in the solar interior. This theory relies on the assumption that the observed surface wavefield (pupil) is a composite entirely of waves converging to (ingression) or diverging from (egression) the point of interest (focus point). The mathematical formulation is described by Lindsey and Braun (2000) and is formulated based on the Kirchoff integral solution to the wave equation (Jackson, 1975).

The egression $H_+^{\mathcal{P}}$ or ingression $H_-^{\mathcal{P}}$ is given by Gizon and Birch (2005) as

$$H_\pm^{\mathcal{P}}(\boldsymbol{r}, \omega) = \int_{\mathcal{P}} d^2\boldsymbol{x}' G_\pm(\boldsymbol{x} - \boldsymbol{x}', z, \omega)\Phi(\boldsymbol{x}', \omega) \tag{1.1}$$

where $\boldsymbol{r} = (\boldsymbol{x}, z)$ is the focus point, $\boldsymbol{x}'$ is the horizontal position within the pupil $\mathcal{P}$, Φ is the scalar wavefield, ω is the angular frequency and G is a Green's function designed to propagate the surface wavefield forwards (or backwards) in time into the solar interior. The construction of the Green's function has seen many forms and differs greatly depending on the approach from a ray theory or wave theory perspective.

From this, stems the ability to estimate the amount of wave power emitted from a specific point or region at a particular time or frequency. Formally, this estimate of acoustic power at a particular time is given by

$$P(\mathbf{r}, t) = |H_+(\mathbf{r}, t)|^2, \tag{1.2}$$

or at a particular frequency by

$$P(\mathbf{r}, \omega) = |H_+(\mathbf{r}, \omega)|^2. \tag{1.3}$$

In practice, equations (1.2) and (1.3) are integrate over all time and frequency respectively, and give the same total power by Parseval's theorem. The implementation of egression acoustic power maps by Donea et al. (1999) led to time series revealing the acoustic sources of the newly discovered phenomena of solar quakes. Further implementation revealed a whole catalogue of solar quakes, opening a fresh field of research. Solar quakes appear as concentric surface ripples in Doppler difference images (see Figure 1.1), emanating from a localised source, although significant anisotropies within these ripples are prominent for most quakes observed to date. The acoustic source driving the quakes has been strongly linked with the onset of solar flares, but the exact mechanism responsible for initiation is still debated. Not all solar flares generate solar quakes and it is not clear why this is.

A further related technique is time-distance local helioseismology, its goal being to measure and interpret travel times between two points on the solar surface (Duvall et al., 1993). An anomaly in the predicted travel time indicates an inhomogeneity along the ray path. Through filtering and inversion techniques, the properties and dynamics of the sub-surface fluid then becomes apparent (Jensen, 2003). The differences in solar travel times are generally inferred to be due to the influence of magnetic fields, flow perturbations or thermodynamic effects. Defining accurate travel time inversion kernels required to
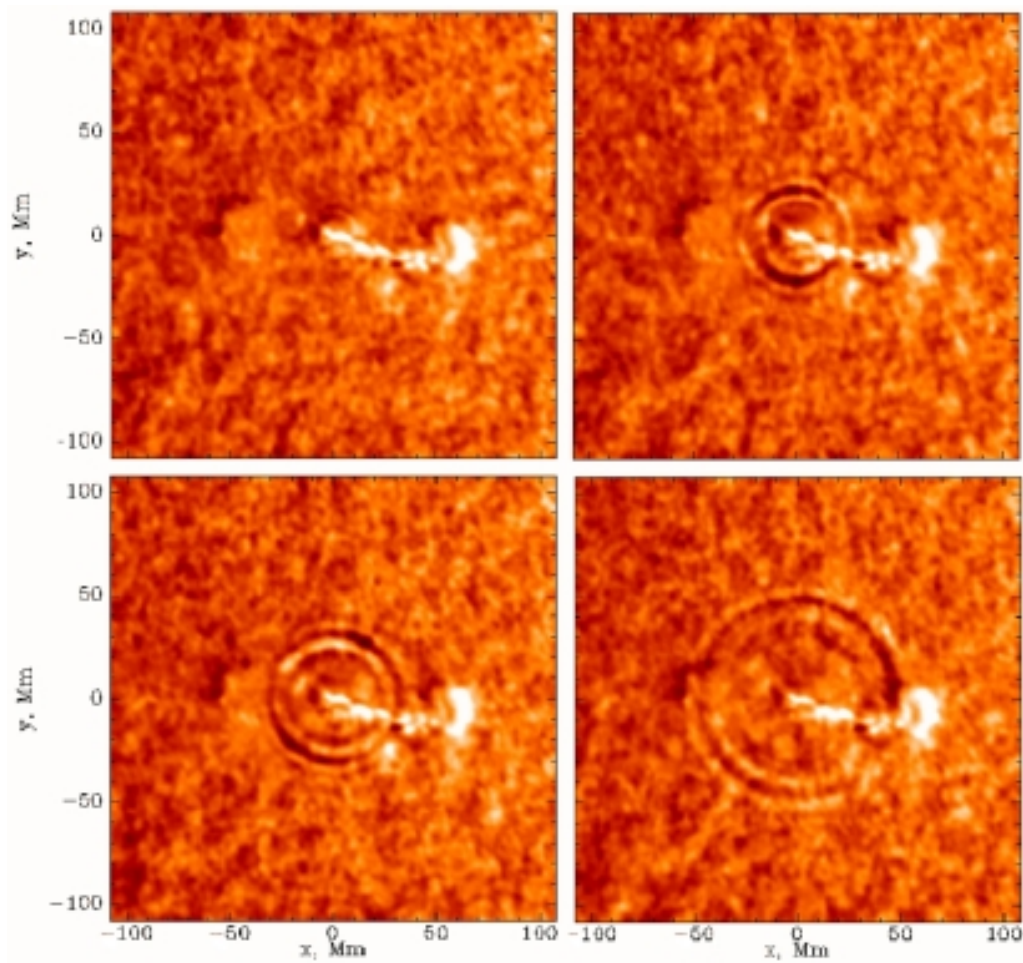
Figure 1.1: Remapped and filtered MDI Dopplergrams showing the temporal and spatial evolution of the first observed solar quake following the 9 July 1996 X-ray flare from Kosovichev and Zharkova (1998).

complete the computations for magnetic fields has proven difficult and consequently, the effects of the magnetic field were oft discounted. Strong observational evidence suggested active region magnetic fields significantly modify the helioseismic signals (Schunker et al., 2005) and as such, disregarding their influence would come at a cost.

Propagation of waves through magnetic fields have been theoretically modelled using linear geometric ray path calculations, as is common in the optics field. The solutions are based on the Wentzel-Kramers-Brillouin (WKB) approximation for small wavelengths and are found by tracking a sound speed perturbation as an integration along a ray path. However, this similarly has its failings in areas where the sound and Alfvén speeds coincide

($a = c$ layer), which occurs in the solar atmosphere near its surface layers and is commonly referred to as the equipartition level. Here, the eikonal assumption upon which standard ray theory is based fails as it has no mechanism to allow tunnelling between the slow and fast magnetoacoustic wave modes. Cally (2006); Schunker and Cally (2006) rectified this by providing a description of a more generalised ray theory, which can be applied to waves in complex magnetic field models.

The helioseismic waves driven internally (p-modes) and emerging in magnetically active regions are effectively acoustic (fast) waves. Upon interaction with strong magnetic fields, these waves see significant physical changes, leading to variations in their travel times, which are in turn heavily relied upon in helioseismic inversions (Moradi and Cally, 2013): 1. Fast wave reflection near the height where the Alfvén speed matches the fast wave horizontal phase speed (Melrose, 1977; Cally and Goossens, 2008; Khomenko and Cally, 2012), 2. The ramp-effect, which reduces the effective magnetoacoustic cut-off frequency dependent upon the magnetic field inclination (Bel and Leroy, 1977), 3. Fast to Alfvén mode conversion near the fast wave reflection height (Cally and Hansen, 2011), and 4. Fast to slow mode conversion at the equipartition layer (Cally, 2006).

Fast to slow mode conversion involving an exchange of energy occurs between the two modes, an effect believed to be the primary cause of p-mode absorption in sunspots (Spruit and Bogdan, 1992; Cally, 1995; Cally and Bogdan, 1997a; Crouch and Cally, 2003; Cally et al., 2003; Crouch and Cally, 2005). The degree of transmission between the two modes is moderated by a transmission coefficient, which is heavily dependent upon the attack angle, the angle the wave vector makes with the magnetic field. A smaller attack angle leads to greatest transmission between the two modes. A recent analysis by Núñez (2019) suggested that magnetoacoustic waves that have developed into shocks by the time they reach the equipartition layer not only split their energy into the two modes but that both resulting waves are smoothed in the process.

Magnetohydrodynamic (MHD) waves have long been theorised as a possible mechanism for heating the outer atmosphere of the Sun (Narain and Ulmschneider, 1996), although there is not a clear understanding of the energy transport and release mechanisms involved (Kuperus, 1969; Hood, 2010). Figure 1.2 shows a model chromospheric temperature distribution, highlighting the extreme drop in density and corresponding increase in temperature at the top of the chromosphere, an area known as the transition region. Without a thorough understanding of the processes which moderate what type and how

much of each wave mode is penetrating into the upper solar atmosphere, there is likely to be little progression in deciphering the role MHD waves play in this scenario.
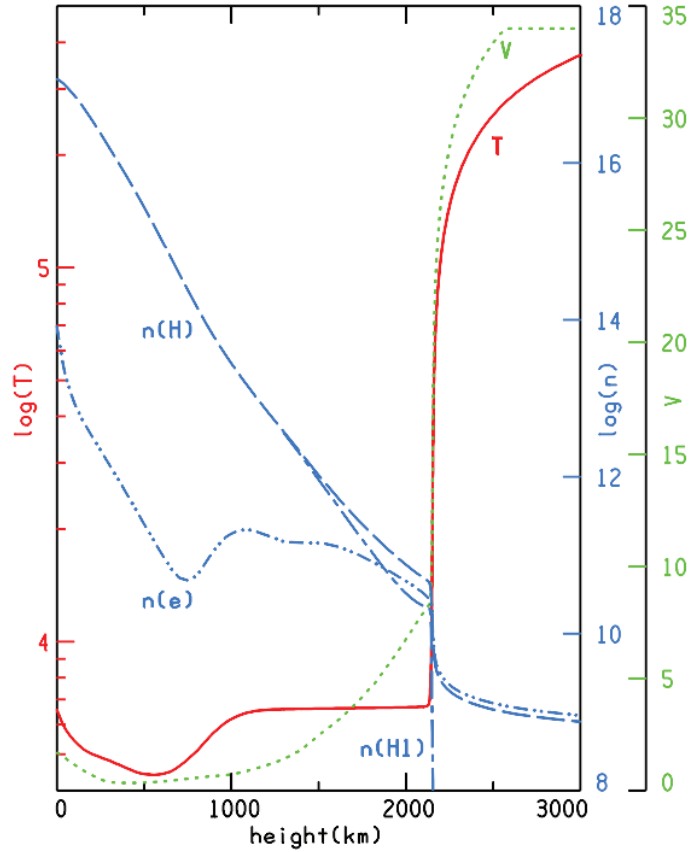
Figure 1.2: Temperature (red in K), turbulent velocity (green in km s^{-1}), total hydrogen density (blue dashed in cm^{-3}), neutral hydrogen density (blue dot-dashed in cm^{-3}), and electron density (blue dot-dot-dashed in cm^{-3}) distributions from photosphere to transition region extracted from Avrett and Loeser (2008)

As magnetoacoustic waves propagate into the chromosphere, there is also the potential for partial acoustic reflection off any acoustic impedances, most notably the transition region temperature gradient. These reflection sites have the potential to create chromospheric cavities with semi-permeable walls (Zhugzhda, 2007, 2008), providing a location for trapped waves to resonate within them. This effect can further confound the results of measuring oscillation amplitudes in the chromosphere as it is uncertain as to whether they are the result of purely upward propagating waves as suggested by Banerjee et al. (2002); Centeno et al. (2006); Afanasyev and Nakariakov (2015) or whether downward propagating (Gurman, 1987) and standing waves complement them (Botha et al., 2011).

1.2 Numerical Modelling of Magnetohydrodynamic Waves

The discovery of the aforementioned solar phenomena can be predominantly attributed to observations, whilst explaining their physical underpinnings is largely the domain of theorists. However, the theory is generally limited to simplified analytical models, not sufficient to explain the full workings of heavily complex environments such as the solar atmosphere. Realistic solar magnetic field configurations are rarely amenable to analytic solutions and in order to accurately model them and the physical processes within, the implementation of forward modelling via numerical methods is required.

Numerical simulations have long been used as a link between observation and theory. Their implementation has seen the investigation of a wealth of solar atmospheric conditions and the waves being generated in and/or propagating through them. A far from exhaustive list shows recent simulations covering MHD mode-conversion (Felipe et al., 2010); subsurface flows (Bhattacharya and Hanasoge, 2016), coronal dynamics (Prasad et al., 2017), the solar wind (Cameron and Jackel, 2019), turbulent convection (Jacoutot et al., 2008) and shock formation/heating (Orta et al., 2003).

Historically, the well known Courant-Friedrichs-Lewy (CFL) timestep constraint (Courant et al., 1928) on numerical simulations has proved heavily restrictive on simulations modelling the solar atmosphere. The need to resolve small spatial scales and large characteristic Alfvén speeds reduces the allowable numerical time-step when using explicit schemes. This problem has been somewhat alleviated by increases in computational power of the preceding decades and also with the introduction of Lorentz Force reductions (Rempel et al., 2009) or Alfvén speed limiters such as that of Boris (1970). Amongst others, the codes MANCHA (Felipe et al., 2010), VAC (Tóth, 1996), SLIM (Cameron et al., 2007), SPARC (Hanasoge, 2011) and LareXd (Arber et al., 2001) have all been instrumental in the progress of forward modelling of MHD waves. The intrinsic complexity and the requirement for magnetic solenoidity in the numerical solutions leads to each code approaching the task in a different mathematical manner, with their various advantages and shortcomings discussed in a succinct fashion by Murawski (2011).

1.2.1 MHD Equations

All MHD simulations inevitably require solving some form of the MHD equations, which can be found using various methods, and at their core can be derived strictly from the Boltzmann equations (Goedbloed and Poedts, 2004). A simplified version of the MHD equations taken from Fitzpatrick (2014) are given below; these describe the motion of a perfectly conducting (ideal) fluid and its interaction with a magnetic field in a uniform atmosphere. They stem from the combination of Maxwell's equations with the equations of gas dynamics. It is assumed that the typical plasma velocities are much less than the speed of light and the effect of gravity is also ignored. The MHD equations are thus given here as

$$\frac{d\rho}{dt} + \rho \nabla \cdot \mathbf{v} = 0, \tag{1.4}$$

$$\rho \frac{d\mathbf{v}}{dt} + \nabla p - \rho \mathbf{g} - \frac{1}{\mu_0}(\nabla \times \mathbf{B}) \times \mathbf{B} = 0, \tag{1.5}$$

$$-\frac{\partial \mathbf{B}}{\partial t} + \nabla \times (\mathbf{v} \times \mathbf{B}) = 0, \tag{1.6}$$

$$\frac{d}{dt}\left(\frac{p}{\rho^\gamma}\right) = 0. \tag{1.7}$$

Here, ρ is the mass density, p is the scalar pressure, $\mathbf{v}$ is velocity, $\mathbf{g}$ is gravity, $\mathbf{B}$ is the magnetic field strength, μ_0 is the permeability of free space, and γ is the ratio of specific heats. Owing to this description being of ideal MHD, several terms are absent, such as those encompassing the effects of viscosity, resistivity, hall effects, etc. In any case, these omitted non-ideal terms are considered negligible on the length scales considered within this study. In order to utilise these equations to study the propagation of small amplitude linear waves, we rewrite the system of equations (1.4) - (1.7) in terms of an initial time-independent background equilibrium state $(p_0, \rho_0, \mathbf{B_0}, \mathbf{v_0})$ and small perturbations $(p_1, \rho_1, \mathbf{B_1}, \mathbf{v_1})$ to that state, such that

$$\rho = \rho_0 + \rho_1, \tag{1.8}$$

$$p = p_0 + p_1, \tag{1.9}$$

$$\mathbf{B} = \mathbf{B_0} + \mathbf{B_1}, \tag{1.10}$$

$$\mathbf{v} = \mathbf{v_0} + \mathbf{v_1}. \tag{1.11}$$

Given no equilibrium flow velocity, this implementation gives a new set of equations

$$\frac{d\rho_1}{dt} + \rho_0 \nabla \cdot \mathbf{v_1} = 0, \tag{1.12}$$

$$\rho_0 \frac{d\mathbf{v_1}}{dt} + \nabla p_1 - \frac{1}{\mu_0}(\nabla \times \mathbf{B_1}) \times \mathbf{B_0} = 0, \tag{1.13}$$

$$-\frac{\partial \mathbf{B_1}}{\partial t} + \nabla \times (\mathbf{v_1} \times \mathbf{B_0}) = 0, \tag{1.14}$$

$$\frac{d}{dt}\left(\frac{p_1}{p_0} - \frac{\gamma \rho_1}{\rho_0}\right) = 0. \tag{1.15}$$

The $(\nabla \times \mathbf{B_0})$ terms have been omitted as all background magnetic field profiles utilised in this study are either constant or potential in nature and thus $\nabla \times \mathbf{B_0} = 0$. Assuming wave like solutions of the form $\exp[i(\mathbf{k} \cdot \mathbf{r} - \omega t)]$, where $\mathbf{k}$ is the wave vector, $\mathbf{r}$ contains the spatial coordinates, ω is the angular frequency, and t is time, it is seen that

$$-\omega \rho_1 + \rho_0 \mathbf{k} \cdot \mathbf{v_1} = 0, \tag{1.16}$$

$$-\omega \rho_0 \mathbf{v_1} + \mathbf{k}p - \frac{1}{\mu_0}(\mathbf{k} \times \mathbf{B_1}) \times \mathbf{B_0} = 0, \tag{1.17}$$

$$-\omega \mathbf{B_1} + \mathbf{k} \times (\mathbf{v_1} \times \mathbf{B_0}) = 0, \tag{1.18}$$

$$-\omega \left(\frac{p_1}{p_0} - \frac{\gamma \rho_1}{\rho_0}\right) = 0. \tag{1.19}$$

Under the assumption that $\omega \neq 0$, equations (1.16) - (1.19) yield the solutions

$$\rho_1 = \rho_0 \frac{\mathbf{k} \cdot \mathbf{v_1}}{\omega} \tag{1.20}$$

$$p_1 = \gamma p_0 \frac{\mathbf{k} \cdot \mathbf{v_1}}{\omega}, \tag{1.21}$$

$$\mathbf{B_1} = \frac{(\mathbf{k} \cdot \mathbf{v_1})\mathbf{B_0} - (\mathbf{k} \cdot \mathbf{B_0})\mathbf{v_1}}{\omega}. \tag{1.22}$$

Substituting equations (1.20) - (1.22) into the equation of motion given in (1.17) leads to

$$\left[\omega^2 - \frac{(\mathbf{k} \cdot \mathbf{B_0})^2}{\mu_0 \rho_0}\right]\mathbf{v_1} = \left\{\left[\frac{\gamma p_0}{\rho_0} + \frac{\mathbf{B_0^2}}{\mu_0 \rho_0}\right]\mathbf{k} - \frac{(\mathbf{k} \cdot \mathbf{B_0})}{\mu_0 \rho_0}\mathbf{B_0}\right\}(\mathbf{k} \cdot \mathbf{v_1})$$
$$- \frac{(\mathbf{k} \cdot \mathbf{B_0})(\mathbf{v_1} \cdot \mathbf{B_0})}{\mu_0 \rho_0}\mathbf{k}. \tag{1.23}$$

For a hydrodynamic case with no magnetic field ($\mathbf{B_0} = 0$), the solution is simply

$$\omega^2 = c^2 \mathbf{k}(\mathbf{k} \cdot \mathbf{v_1}), \tag{1.24}$$

where

$$c = \sqrt{\frac{\gamma p_0}{\rho_0}} \qquad (1.25)$$

is the sound speed. This solution is a longitudinal sound wave with phase velocity $\frac{\omega}{|\mathbf{k}|}\mathbf{k} = \pm c\mathbf{k}$ and group velocity $\frac{\partial \omega}{\partial \mathbf{k}} = c\mathbf{k}$. In the case of a non-zero magnetic field and without loss of generality, the equilibrium magnetic field $\mathbf{B_0}$ can be directed along the z-axis with the wave vector $\mathbf{k}$ lying in the $x - z$ plane. Then, equation (1.23) can be reduced to the eigenvalue equation

$$\begin{pmatrix} \omega^2 - k^2a^2 - k^2c^2\sin^2\theta & 0 & -k^2a^2\sin\theta\cos\theta \\ 0 & \omega^2 - k^2a^2\cos^2\theta & 0 \\ -k^2a^2\sin\theta\cos\theta & 0 & \omega^2 - k^2a^2\cos^2\theta \end{pmatrix} \begin{pmatrix} v_x \\ v_y \\ v_z \end{pmatrix} = \mathbf{0}. \quad (1.26)$$

Here, the subscripts for the perturbation velocity have been dropped and replaced with their respective cartesian coordinates, θ is defined as the angle between $\mathbf{B_0}$ and $\mathbf{k}$, $k = |\mathbf{k}|$, and

$$a = \sqrt{\frac{B_0^2}{\mu_0 \rho_0}} \qquad (1.27)$$

is the Alfvén speed. Solutions to equation (1.26) exist only when the determinant of the left hand square matrix is zero, which in turn provides the dispersion relation

$$(\omega^2 - k^2a^2\cos^2\theta)[\omega^4 - \omega^2 k^2(a^2 + c^2) + k^4 a^2 c^2 \cos^2\theta] = 0. \qquad (1.28)$$

There are three independent real roots of the above dispersion relation, which correspond to the three different types of waves that can propagate through an MHD medium. Starting with

$$\omega = ka\cos\theta, \qquad (1.29)$$

which describes the shear Alfvén wave. This wave involves plasma motion strictly perpendicular to the magnetic field, a fact which can be seen through equations (1.20) and (1.21), which reveal zero perturbation to the density or pressure. The remaining two roots of the dispersion relation are

$$\omega^2 = \frac{k}{2}\left[a^2 + c^2 \pm \sqrt{(a^2 + c^2)^2 - 4a^2c^2\cos^2\theta}\right]. \qquad (1.30)$$

Here, the fast magnetoacoustic wave mode (fast wave) corresponds to the (+) solution, and the slow magnetoacoustic slow mode (slow wave) corresponds to the (-) solution. These

11

waves have non-zero perturbations to the density and pressure and involve plasma motion both perpendicular and parallel to the magnetic field.

The fast v_f and slow v_s wave velocities will depend upon their propagation direction relative to the background magnetic field. A fast wave sees its maximum velocity $v_f = \sqrt{c^2 + a^2}$ occur when travelling perpendicular to the magnetic field, and conversely its minimum velocity $v_f = \max[a, c]$ when parallel. A slow wave on the other hand, experiences its maximum velocity $v_s = \min[a, c]$ when travelling parallel to the magnetic field, and it is unable to propagate perpendicularly.

The nature of both the fast wave and slow wave depends upon the ratio of the plasma pressure to magnetic pressure (the plasma beta β), which is in turn related to the ratio of the sound and Alfvén velocities:

$$\beta \equiv \frac{2\mu_0 p_0}{B_0^2} = \frac{2}{\gamma}\frac{c^2}{a^2}. \tag{1.31}$$

When $\gamma = 5/3$, equation (1.31) gives the relation $\beta = 1.2(c^2/a^2)$. In a typical quiet solar atmosphere, β finds unity in the layers near the photosphere and lower chromosphere. When $\beta \gg 1$, such is common in the solar interior, the fast wave will be essentially acoustic in nature and the slow wave magnetic. When $\beta \ll 1$, which is characteristic of the solar corona, the opposite is true such that the fast wave is essentially magnetic in nature and the slow wave acoustic. The Friedrichs diagrams shown in Figure 1.3 give a schematic representation of the phase velocities associated with the Alfvén, fast and slow waves for different values of β.

1.2.2 Stratified Atmosphere

Waves travelling through a stratified medium, such as the solar atmosphere, are altered by the various parameters which govern that medium. These waves are influenced by three restoring forces: compression, buoyancy and the magnetic field itself. Ignoring the effects of the magnetic field, which is common when examining p-modes in the solar interior, an acoustic dispersion relation can be found. Utilising the plane-parallel approximation, the wave equation can be solved exactly (see equations 2.2 and 2.3 from Deubner and Gough (1984)) and is given as

$$\omega^2 = \omega_c^2 + c^2 k_z^2 - \frac{c^2 N^2 k_x^2}{\omega^2}, \tag{1.32}$$

where k_z and k_x are the vertical and horizontal wavenumbers respectively. Introduced here are two important parameters, which will be looked at individually. The Brunt-Väisälä
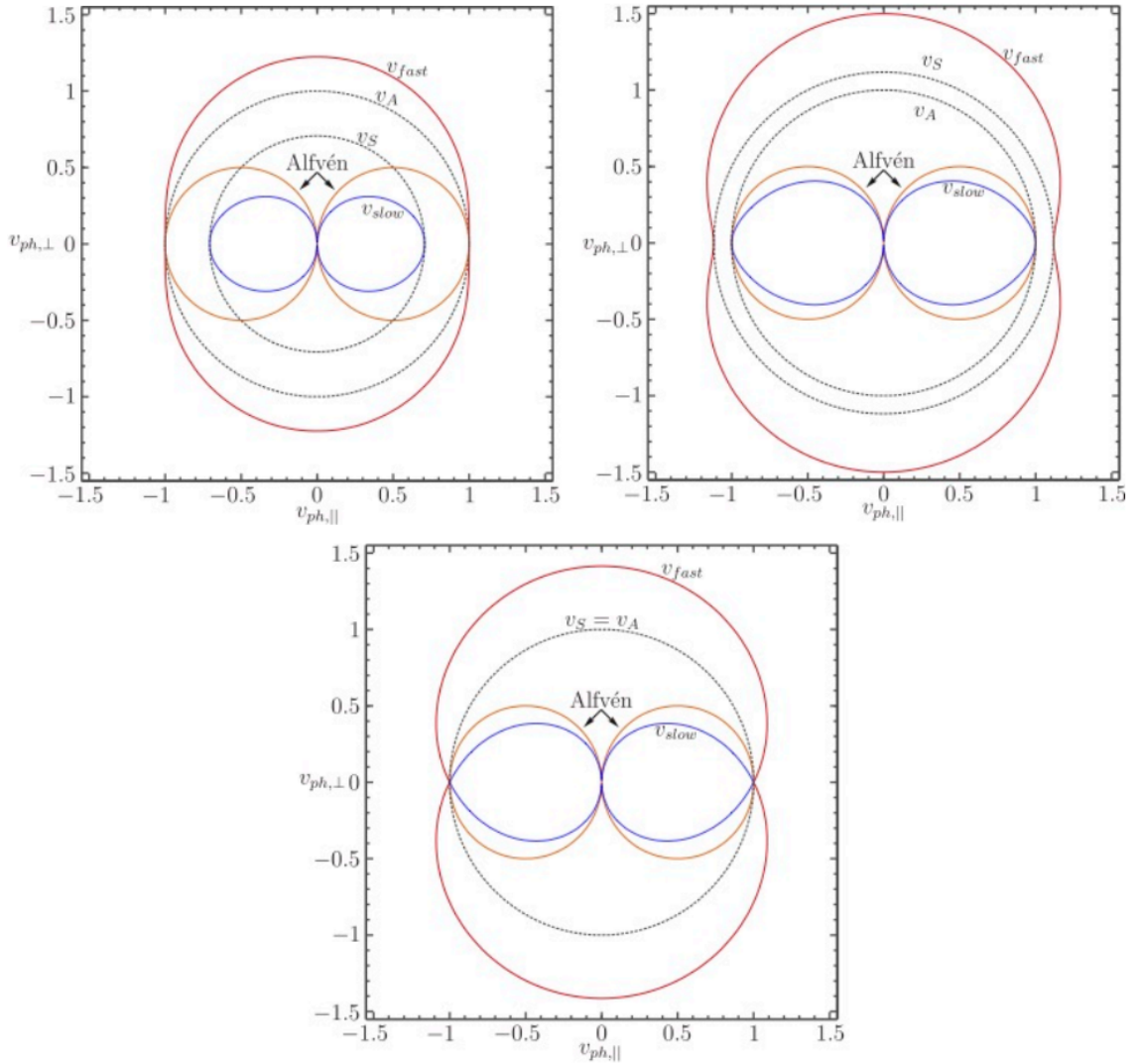
Figure 1.3: Friedrichs diagrams for $c < a$ with $\beta = 0.6$ (top-left), $c > a$ with $\beta = 1.5$ (top-right), and $c = a$ with $\beta = 1.2$ (bottom). The phase speed perturbation of the slow waves is illustrated in blue, the fast wave in red, and the Alfvén wave in orange. The dotted lines correspond to the sound and Alfvén speed. The horizontal and vertical axes ($v_{ph,\parallel}$ and $v_{ph,\perp}$ respectively) represent the velocity perturbation components parallel and perpendicular to the background equilibrium magnetic field $\mathbf{B_0}$. Figure extracted from Jess et al. (2015).

(or buoyancy) frequency N is a measure of the stability of a fluid particle to vertical displacements and is given by

$$N = \sqrt{\frac{g}{H} - \frac{g^2}{c^2}}, \qquad (1.33)$$

where $H(z) = -\rho(z)/\rho'(z)$ is the density scale height. When $N^2 > 0$, the Brunt-Väisälä frequency is real valued and a vertically displaced fluid particle will oscillate around the height where the density of the particle matches the density of the surrounding air, describing a convectively stable stratified environment. If $N^2 = 0$, a displaced fluid particle will move no further. When $N^2 < 0$, N is imaginary, and a vertically displaced fluid particle will continue to propagate until N^2 becomes zero or negative, a process known as convection.

The isothermal cut-off frequency is always defined as

$$\omega_{ci} = \frac{c}{2H}. \qquad (1.34)$$

However, the vertically stratified cut-off frequency is non-unique as it can take a variety of forms depending upon the choice of dependent and independent variables for the wave equation (Schmitz and Fleck, 2003). For a non-magnetic atmosphere, the most common form for the cut-off frequency of a stratified atmosphere is

$$\omega_c = \frac{c}{2H} \left(1 - 2\frac{dH}{dz} \right)^{1/2}, \qquad (1.35)$$

as given by Deubner and Gough (1984). Waves with frequencies below the acoustic cut-off will become evanescent. This process strongly influences which frequency waves survive as they propagate through the temperature minimum (maximum acoustic cut-off frequency) and into the upper chromosphere. The acoustic cut-off frequency effectively provides an upper reflecting point for vertically propagating acoustic waves in the solar atmosphere.

Further inspection of the acoustic dispersion relation reveals the Lamb depth, which occurs when

$$\omega^2 = c^2 k_x^2. \qquad (1.36)$$

This describes a lower reflecting point for vertically propagating acoustic waves, and when coupled with acoustic cut-off effect, provides the boundaries for the well known p-mode cavity for acoustic solar waves.

Having looked at the effects of stratification in an acoustic atmosphere, attention is turned to the effect of a non-zero magnetic field, which provides an extra restoring force

for MHD waves. The combined effects of both acoustic and magnetic restoring forces were first studied by Ferraro and Plumpton (1958), who considered the case of a uniform vertical magnetic field in an isothermal atmosphere. A dispersion relation for the special case of constant wave parameters (sound speed, Alfvén speed, density scale height) was then developed by Yu (1965). Not long after, McLellan and Winterberg (1968) produced a complex dispersion relation for gravitationally stratified atmospheres, which was reworked into a more amenable form by Thomas (1982).

Following these previous works, and by beginning with the self-adjoint formulation of linear MHD (Goedbloed and Poedts, 2004), a dispersion relation for gravitationally stratified MHD was given in Schunker and Cally (2006) as

$$
\begin{aligned}
\omega^4 = {} & (a^2 + c^2)k^2\omega^2 - a^2c^2k^2k_\parallel^2 \\
& - c^2 N^2 k_x^2 + (\omega^2 - a^2 k^2 \cos^2 \theta)\omega_c^2.
\end{aligned}
\tag{1.37}
$$

This dispersion relation reverts back to the classical magneto-acoustic dispersion function for unstratified media given in the right hand parentheses of equation (1.28), and to the acoustic dispersion relation for the non-magnetic case given in equation (1.32).

A dispersion relation of the form given in equation (1.37) is set out nicely to describe the extra influences imparted by the introduction of the magnetic field. Firstly, in the asymptotic regime $a \gg c$ (high in the atmosphere), the acoustic slow wave is given as

$$
\omega^2 = c^2 k_\parallel^2 + \omega_c^2 \cos^2(\theta),
\tag{1.38}
$$

where θ is the angle of the magnetic field from vertical. From this, the modification to the acoustic cut-off frequency due to the magnetic field inclination becomes apparent as

$$
\omega_m = \omega_c \cos \theta.
\tag{1.39}
$$

Hence, a strong more inclined field reduces the effective cut-off frequency and allows lower frequency waves to propagate freely. It enables slow waves to reach higher into the solar atmosphere, a feature known as the 'ramp effect' (De Pontieu et al., 2004), where they are observed as 'magnetic portals' (Jefferies et al., 2006). The influence of the magnetic field inclination on the cut-off frequency is also the main reason behind the dominant frequency variation at a given height in sunspot atmospheres (Solanki, 2003).

Secondly, in the asymptotic regime $c \gg a$ (deep in the interior), the magnetic slow wave is given as

$$
\omega^2 = a^2 k^2 \left(\frac{c^2 k_\parallel^2 + \omega_c^2 \cos^2(\theta)}{c^2 k^2 + \omega_c^2 - c^2 N^2 k_c^2/\omega^2} \right),
\tag{1.40}
$$

15

which shows that the slow wave becomes field aligned when density and pressure perturbations are neglected, reminiscent of the shear Alfvén wave.

Lastly, the fast waves are given by

$$\omega^2 = a^2 k^2 + c^2 k_\perp^2 + \omega_c^2 \sin^2(\theta) - \frac{c^2 N^2 k_x^2}{\omega^2} \tag{1.41}$$

in the asymptotic $a \gg c$ regime, and

$$\omega^2 = c^2 k^2 + \omega_c^2 - \frac{c^2 N^2 k_x^2}{\omega^2} + a^2 k^2 \frac{c^2 k_\perp^2 + \omega_c^2 \sin^2(\theta) - c^2 N^2 k_c^2 \omega^2}{c^2 k^2 + \omega_c^2 - c^2 N^2 k_c^2 \omega^2} \tag{1.42}$$

in the asymptotic $c \gg a$ regime. These representations show that the fast wave propagates slightly faster across magnetic field lines.

Unfortunately, the dispersion relation based upon the WKB solution is unable to distinguish between the slow and fast wave modes around the equipartition layer z_{eq}, which occurs when $a = c$. Here, mode conversion and transmission can occur, which allows energy to pass between the two modes. Schunker and Cally (2006) showed that transmission (energy moving from slow-fast or fast-slow) occurs preferentially for (i) small attack angle, the angle between the wave vector and the magnetic field; (ii) low frequencies (small wavenumber); and (iii) small equipartition layer depth.

Above the $a = c$ layer, and near the fast wave reflection height, fast-Alfvén mode conversion can take place. Unlike slow-fast mode conversion, which can occur in a 2D geometry, fast-Alfvén mode conversion requires a 3D geometry as it only transpires when the wavevector is at an angle to the plane of the magnetic field. Numerical modelling has shown that the strongest Alfvén fluxes recorded high in the solar atmosphere occur when the magnetic field is inclined $30°$ - $40°$ from vertical, and when the wave propagates at a angle of $60°$ - $80°$ from the plane of the magnetic field (Cally and Goossens, 2008). Further studies have shown that fast-Alfvén conversion occurs preferentially at high inclinations with an angle between the wave vector and magnetic field of $50°$ - $120°$ (Felipe, 2012).

Alfvén waves have been detected in the interplanetary medium using data taken from as far back as the Mariner 5 spacecraft voyage (Belcher and Davis, 1971). They have been found to be ubiquitous in the outer solar atmosphere (Tomczyk et al., 2007) and their absorption has been proposed as a possible mechanism for heating the solar corona (Mishonov et al., 2007). The low ionisation fraction of the photosphere suggests it may not be possible to generate Alfvén waves in this area (Vranjes et al., 2008), although this has been disputed (Tsap et al., 2011; Soler et al., 2013). Alfvén waves may also suffer from

near-total reflection at the transition region (Uchida and Sakurai, 1975). Hansen and Cally (2012) sought to mitigate these problems by providing numerical simulations showing that Alfvén waves may be generated high in the chromosphere by fast-Alfvén mode conversion and that their reflection is greatly reduced if the fast wave reflection height is sufficiently close to the transition region.

1.3 Numerical Codes

Two different numerical codes are used to perform the simulations described within, Lare2d and SPARC. Both codes employ the use of Message Passing Interface (MPI) to parallelise the computation and reduce computation time. Further to this, all plots were produced via the Interactive Data Language (IDL) or Mathematica.

1.3.1 Lare2d

Lare2d is a subset of the codes described by Arber et al. (2001). It implements a non-ideal Lagrangian remap code to solve the 2-D MHD equations. It utilises a staggered grid and is second-order accurate in space and time. The code correctly handles shocks, whilst not using the traditional approximate Riemann solver. The method instead is based on each step taking a fully 3-D Lagrangian step via a second-order predictor corrector scheme before being conservatively remapped onto the original grid. The technique becomes viable when solving Euler's equations through an appropriately staggered grid and Wilkins artificial viscosity implementation, although it has been shown to be not as robust as those using an approximate Riemann solver. It was designed to accurately include the nonhyperbolic physics such as resistivity, viscosity, radiation, thermal conduction, and gravity, which are common in the high solar atmosphere. The use of gradient limiters and shock viscosities make the Lare2d code ideally suited to shock calculations and is hence used in Chapter 2 to realise the smoothing effects of MHD shocks in mode conversion. The code is also used in Chapter 3 to investigate chromospheric resonances in the umbrae of sunspot atmospheres.

1.3.2 SPARC

The Seismic Propagation through Active Regions and Convection (SPARC) was developed progressively through the works of Hanasoge et al. (2006, 2007); Hanasoge (2008) and eventually to its full 3-Dimensional form described in Hanasoge (2011). The code uses an implicit compact sixth-order finite difference scheme, which is used to solve the linear idealised MHD equations for waves in a stratified solar environment. Explicit filters are also used to prevent numerical instabilities in the solutions. The option of Perfectly Matched Layers (Hanasoge et al., 2010) for any or all boundaries is available, which provides efficient absorption of outgoing waves. Further 'sponge' type absorbing layers can also be implemented, which introduce a linear friction based term to the underlying equations (Colonius, 2004). An Alfvén speed limiter can be invoked to avoid reduction of the time-step and consequent unrealistic computational times. This process is based primarily on the limitation of the Lorentz Force (Rempel et al., 2009) and the implications on computational helioseismology for various atmospheres is discussed in detail by Moradi and Cally (2014). The non-linear effects ignored by this code are primarily found at great heights in the solar atmosphere, such as in the mid-upper chromosphere and corona. Perturbations in sub-surface and photospheric layers are dominated by linear effects and in line with this, SPARC will be utilised in Chapter 4 to study the sub-photospheric propagation of waves known to produce 'solar quakes' at the solar surface.

Smoothing of MHD Shocks in Mode Conversion

2.1 Introduction

2.1.1 Linear Mode Conversion

MHD waves have the propensity to change their nature whilst travelling through the various physical conditions of the solar atmosphere. These conversions between fast, slow and Alfvén wave types can occur multiple times and are well known throughout the recent solar literature. Linear wave conversions from fast-slow (Schunker and Cally, 2006) and fast-Alfvén (Cally and Goossens, 2008; Cally and Hansen, 2011) have been explored in detail and reviewed by Cally et al. (2016). Linear fast-Alfvén conversion is realised in the neighbourhood of the fast wave reflection height for stratified atmospheres (provided there is some non-zero angle between the wave vector and the magnetic field) and linear fast-slow conversion occurs where the Alfvén speed a roughly matches that of the local sound speed c. It is this latter case we will introduce and explore in further detail.

Fast-Slow Conversion

Extensive observations of the quiet solar surface surrounding sunspots revealed that p-modes are partially absorbed in magnetically active regions (Braun et al., 1987, 1988, 1992; Bogdan et al., 1993; Braun, 1995). A mechanism of fast-slow conversion was proposed to be responsible by Spruit (1991). The mode description of this process was

19

then significantly advanced and coupled with strong observational data to give credence to this original description of fast-slow wave conversion. Following this, time-distance helioseismology techniques such as those of D'Silva (1996); Kosovichev et al. (2000); Gizon and Birch (2002), as well as a formulation based on acoustic holography given by Braun and Lindsey (2000) were used to supplement the original modal description (Cally and Bogdan, 1993, 1997b; Cally et al., 1994; Cally, 2000; Cally et al., 2003; Crouch and Cally, 2005) (see also the review by Cally et al. (2016)).

However, it wasn't until Cally (2005), that the introduction of a strong magnetic field was implemented with any considerable rigour. This allowed a perturbation-based approach to proceed, in which the perturbed quantity was that of the inclination of the magnetic field; an important addition to the theory given active regions comprise of magnetic fields which can be both strong and highly inclined to the vertical. The results of this analysis led to an understanding of where and under what physical conditions fast-slow or slow-fast conversion might take place in a solar-like context. It was discovered that slow and fast magnetoacoustic waves couple within the neighbourhood of the Alfvén acoustic equipartition layer z_{eq} where the Alfvén and sound speeds coincide, $a = c$. This coupling allows the transition from fast-slow wave types or equivalently, slow-fast. The degree of transmission is moderated by a transmission coefficient T; the most important constituent of which is the attack angle, the angle the wave vector makes with the magnetic field. Greater transmission between the two wave types is apparent with a smaller attack angle.

The perturbation method was then developed by Cally (2006) for a more generalised ray theory approach, utilising dispersion relations based on the mathematical formulations of Tracy et al. (2003). The implementation then allowed the potential for non-analytical thermal and magnetic models to be explored, a vast improvement given the complexity of both the solar and other various stellar atmospheres. Coupled with the matrix description of standard MHD ray theory given by Weinberg (1962), Schunker and Cally (2006) utilised and expanded upon these formalisms to give the most thorough and succinct description of linear mode conversion we have today. It is chosen to look at both the development of the theory given by this description, as well as some of its most important results below.

Beginning from the self-adjoint description of linear MHD by (Goedbloed and Poedts, 2004), and setting $\nabla \times \mathbf{B} = \mathbf{j} = \mathbf{0}$ for a potential magnetic field, the equilibrium equation is

$$-\nabla p + \rho \mathbf{g} = 0,$$

where p is pressure, ρ the density and $\mathbf{g}$ the acceleration due to gravity. Whilst the potential energy of the system is given by

$$
\begin{aligned}
W &= -\frac{1}{2}\int \boldsymbol{\xi}^* \cdot \mathbf{F}(\boldsymbol{\xi})dV \\
&= \frac{1}{2}\int \rho c^2 |\nabla \cdot \boldsymbol{\xi}|^2 + |\mathbf{b}|^2 + \frac{1}{2}\rho \mathbf{g}\cdot(\boldsymbol{\xi}\nabla\cdot\boldsymbol{\xi}^* + \boldsymbol{\xi}^*\nabla\cdot\boldsymbol{\xi}) \\
&\quad + \frac{1}{2}\mathbf{g}\cdot(\boldsymbol{\xi}\nabla\cdot\rho\boldsymbol{\xi}^* + \boldsymbol{\xi}^*\nabla\cdot\rho\boldsymbol{\xi})dV,
\end{aligned} \tag{2.1}
$$

where $\boldsymbol{\xi} = (\xi, 0, \zeta)$ is the displacement vector (specialising to 2D for our purposes), $\mathbf{F}$ is the force per unit volume, $\mathbf{b} = \nabla \times (\boldsymbol{\xi} \times \mathbf{B})$ is the magnetic field perturbation and $\mathbf{B}$ is the background magnetic field. By defining $\mathbf{X} = \rho^{1/2}\boldsymbol{\xi}$ and $Y = \xi\cos\theta - \zeta\sin\theta$, along with some algebraic manipulation, the Lagrangian density can be defined as

$$
\begin{aligned}
\mathcal{L} &= \frac{1}{2}|\dot{\mathbf{X}}|^2 - \frac{1}{2}c^2\left|\nabla\cdot\mathbf{X} + \frac{\mathbf{X}_z}{2H}\right| - \frac{1}{2}\rho a^2 |\nabla\times(Y\hat{\mathbf{e}}_\mathbf{y})|^2 \\
&\quad - \frac{1}{2}\mathbf{g}\cdot(\mathbf{X}\nabla\cdot\mathbf{X}^* + \mathbf{X}^*\nabla\cdot\mathbf{X}),
\end{aligned} \tag{2.2}
$$

The wave equations may be recovered by extremising the action, $\int \mathcal{L}\, dV\, dt$.

Of particular interest is finding Wentzel-Kramers-Brillouin (WKB) type solutions to equation (2.2). This technique is best laid out by Bender and Orszag (1978) and involves assuming an eikonal solution coupled with an asymptotic series expansion. The small parameter ϵ inherent in the process in this case is inverse frequency, suggesting that this process is only valid for high frequencies. By assuming a plane wave like solution, the following definitions can then be introduced, $\nabla \equiv i\mathbf{k}$, $\partial/\partial t \equiv -i\omega$. A further introduction will be $\chi = \nabla\cdot\mathbf{X} = ik_x\rho^{1/2}\xi + ik_z\rho^{1/2}\zeta$. Solving for ξ and ζ in terms of χ and Y, gives $\mathcal{L} = \mathbf{Q}^H\tilde{\mathbf{D}}\mathbf{Q}$, where $\mathbf{Q} = (\chi, Y)^T$ (superscript 'H' denotes the Hermitian transpose), and

$$
\tilde{\mathbf{D}} = \begin{pmatrix} \tilde{D}_a & \tilde{\eta} \\ \tilde{\eta}^* & \tilde{D}_b \end{pmatrix} \tag{2.3}
$$

is the dispersion matrix, where

$$
\tilde{D}_a = \omega^2 - c^2 k_\parallel^2 - \omega_{ci}^2\cos^2\theta, \tag{2.4}
$$

$$
\tilde{D}_b = \omega^2 - a^2 k_\parallel^2 - \omega_{ci}^2\frac{k_x^2}{K^2} \tag{2.5}
$$

21

and

$$\tilde{\eta} = \frac{-ik_\perp \omega^2 + ik_x \omega_{ci}^2 \cos\theta - gk_x k_\parallel + \frac{1}{2}k_x k_\parallel c^2 H(z)^{-1}}{K}, \tag{2.6}$$

with $k_\parallel = k_x \sin\theta + k_z \cos\theta$ and $k_\perp = k_x \cos\theta - k_z \sin\theta$ being the components of the wave vector parallel and perpendicular to the magnetic field respectively, and $K = |\mathbf{k}| = \sqrt{k_x^2 + k_z^2}$. $\tilde{D}_a$ and $\tilde{D}_b$ are effectively the dispersion functions which relate to the distinct acoustic and magnetic modes respectively when far from a conversion zone. Note also the use of ω_{ci} (the isothermal acoustic cut-off frequency) as opposed to the conventional ω_c. The square of the acoustic cut-off frequency ω_c is given by Balmforth and Gough (1990) as

$$\omega_c^2 = \frac{c^2}{4H^2}(1 - 2H'), \tag{2.7}$$

where H is the density scale height. This has been modified so as to reflect an isothermal atmosphere where the derivative of the scale height is zero, giving an acoustic cut-off frequency

$$\omega_{ci} = \frac{c}{2H_\rho}. \tag{2.8}$$

This is an important simplification as the (now excluded) derivative term tends to cause a sharp spike in ω_c near the solar surface for empirical atmospheric models (Schmitz and Fleck, 1998, 2003).

According to standard ray theory, solutions are found by solving the dispersion function $\mathcal{D} = \det \tilde{\mathbf{D}} = 0$. It is then apparent that the solutions to $\tilde{D}_a = 0$ and $\tilde{D}_b = 0$ will give the independent acoustic and magnetic wave solutions. For the dispersion matrix (2.3),

$$\begin{aligned} \mathcal{D} = \omega^4 &- (a^2 + c^2)K^2\omega^2 + a^2c^2K^2k_\parallel^2 \\ &+ c^2N^2k_x^2 - (\omega^2 - a^2K^2\cos^2\theta)\omega_{ci}^2, \end{aligned} \tag{2.9}$$

where $K^2 = k_x^2 + k_z^2$, $k_\parallel$ is the component of the wave vector along the magnetic field direction, and the Brunt-Väisälä frequency N is defined by

$$N^2 = \frac{g}{H} - \frac{g^2}{c^2}. \tag{2.10}$$

As discussed earlier, the solution to equation (2.2) is sought via a WKB type solution. The eikonal method however fails in a variety of circumstances. Most importantly for this discussion focusing on mode conversion, it contains no mathematical mechanism in which

to couple the slow and fast wave types. The rigidity of the system distinguishes both the fast mode and slow mode independently and relinquishes any connection between the two. In regions where $a \gg c$, the fast wave is dictated by magnetic characteristics and the slow wave by acoustic characteristics. Conversely, where $c \gg a$, the slow wave is magnetic in nature and the fast wave, acoustic. Away from these distinct regions and around the conversion zone, the region of interest, the fast and slow waves become mixed in their nature and thus it would be erroneous to decouple them, as is inherent in the standard WKB analysis. Even with attainable higher order approximations, the WKB expansion is asymptotic in nature rather than convergent and hence increased accuracy in these solutions is not guaranteed; this is shown numerically in Cally (2005) for appropriate horizontal phase speeds.

The idea then is to construct a solution which is valid around the conversion region and is further matched asymptotically to the incoming and outgoing solutions away from that particular region. By utilising a local Taylor series expansion around the conversion point and ignoring higher-order terms, the dispersion function can be arranged as $\mathcal{D} = \det$ $\mathbf{D} = \tilde{D}_a \tilde{D}_b - |\eta|^2$. This function is moderated by η, which will be from herein referred to as the 'coupling term'. Away from the conversion zone, η is small in comparison to $\tilde{\mathbf{D}}_{\mathbf{a}}$ and $\tilde{\mathbf{D}}_{\mathbf{b}}$, and can be ignored. However, near regions of conversion, η becomes comparable in size and plays a crucial role in determining the degree of conversion between the two wave types; in other words, it acts to quantify the amount of mode transmission in areas where $\tilde{D}_a = \tilde{D}_b = 0$. A complex mathematical process is then prescribed by Tracy et al. (2003) which sets out what is to be termed the transmission coefficient. In the current MHD context, this describes the amount of energy transitioning from one WKB branch (slow/fast) to the next (fast/slow) and is given by

$$\mathcal{T} = \exp\left(\frac{-2\pi |\eta|^2}{\mathcal{B}}\right), \tag{2.11}$$

where

$$\mathcal{B} = \{\tilde{D}_a, \tilde{D}_b\} = \frac{\partial \mathcal{D}_a}{\partial k_z}\frac{\partial \mathcal{D}_b}{\partial z} - \frac{\partial \mathcal{D}_b}{\partial k_z}\frac{\partial \mathcal{D}_a}{\partial z} \tag{2.12}$$

is the Poisson bracket of the uncoupled dispersion functions. Conversely, there is the complex conversion co-efficient $\mathcal{C}$, where $|\mathcal{C}| = 1 - \mathcal{T}$. The argument of this can be associated with the wave's change in phase. When $\mathcal{T} = 0$, no transmission is recorded and the fast and slow waves retain their nature throughout the conversion zone. Conversely,

$\mathcal{T} = 1$ corresponds to a complete change from fast-slow or slow-fast. It is appropriate to restate that $\mathcal{T}$ was found via a local expansion around a conversion point. It provides a coupling between the eikonal solutions, which are valid elsewhere.

At this point, a new function U is introduced into the equations for both $\tilde{\mathbf{D}}_{\mathbf{a}}$ and $\tilde{\mathbf{D}}_{\mathbf{b}}$. The form of this function is not unique and acts to match the two dispersion functions with their corresponding acoustic and magnetic branches away from the conversion region. Near the conversion region, this addition makes little practical difference and thus the derivation is excluded.

In order to calculate $\mathcal{T}$, the solution to $\mathcal{D} = \det \mathbf{D} = \tilde{D}_a \tilde{D}_b - |\eta|^2$ is sought. At conversion points, $\tilde{D}_a = \tilde{D}_b = 0$, therefore

$$|\eta|^2 = -\mathcal{D}. \tag{2.13}$$

Schunker and Cally (2006) chose to look at the demonstrative case where both the cut-off ω_{ci} and Brunt-Väisälä N frequencies are identically zero. This leaves the conversion points to occur at exactly $a = c$ and $K^2 = \omega^2/c^2$, and gives

$$|\eta|^2 = c^4 K^2 k_\perp^2. \tag{2.14}$$

The transmission coefficient associated with the above scenario is

$$
\begin{aligned}
\mathcal{T} &= \exp\left[-\frac{\pi h K^2 k_\perp^2}{|k_z|(K^2 + k_\perp^2)}\right]_{a=c} \\
&\approx \exp\left(-\frac{\pi h k_\perp^2}{|k_z|}\right)_{a=c} \quad \text{for } |k_\perp| \ll K \\
&= \exp[-\pi K h_s \sin^2 \alpha]_{a=c},
\end{aligned} \tag{2.15}
$$

where $\alpha = \arcsin(k_\perp/K)$ is the attack angle, recalled as the angle the wave vector makes with the magnetic field. Also introduced above is the equipartition scale height $h = [d(a^2/c^2)/dz]_{a=c}^{-1}$, the measure of thickness of the layers in which $a \approx c$, along with $h_s = [d(a^2/c^2)/ds]_{a=c}^{-1}$, the measure of thickness along the path traced out along the direction of the phase velocity $\hat{\mathbf{k}}$.

Examination of equation (2.15) suggests that transmission from slow-fast or fast-slow occurs preferentially for (i) small attack angle; (ii) low frequencies (small wavenumber); and (iii) small equipartition layer depth. Conversely, large attack angle, high frequencies and a wide interaction region enhances conversion, where energy is converted in form from acoustic to magnetic but stays on its original fast or slow branch. This is illustrated in

Figure 2.1, which depicts the ray paths on a (z, k_z) phase diagram for a given horizontal wavenumber k_x, angle of magnetic field from vertical θ, and frequency f. The green acoustic and purple magnetic curves are seen to align closely with their respective fast or slow branches except in the region around $a = c$. In this region, they disassociate themselves and transition through one of the nominal *star* points upon which their respective transmission coefficients $\mathcal{T}$ are calculated. The upper star point corresponds to a small attack angle and higher $\mathcal{T}$ as predicted.
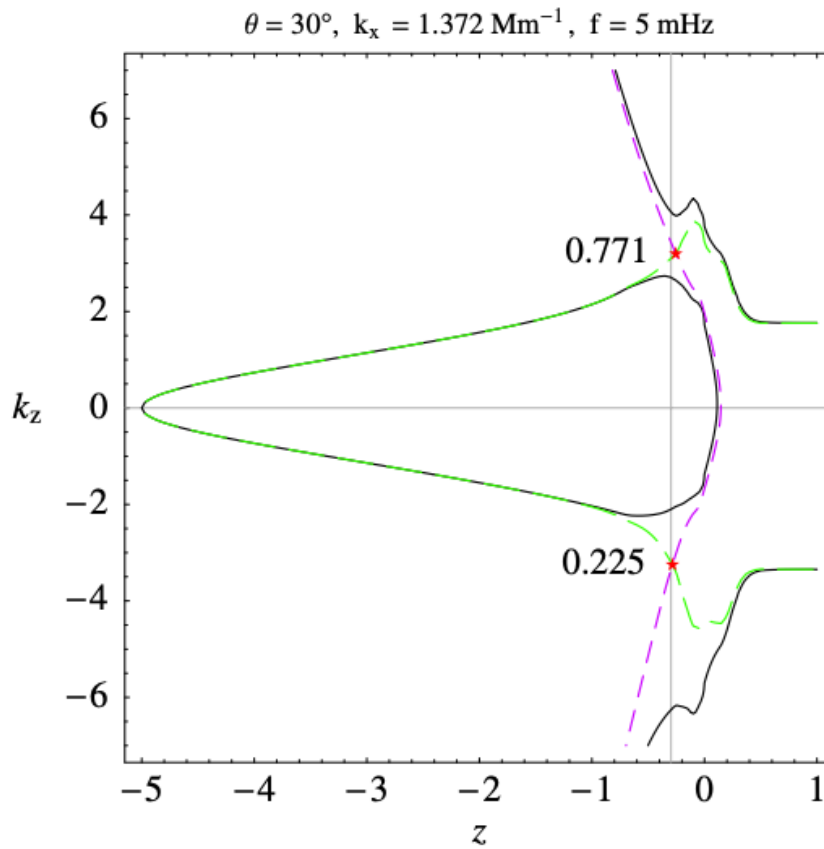
Figure 2.1: $z - k_z$ phase diagram taken from Cally (2007). The background magnetic field is 2 kG and inclined at an angle $\theta = 30°$ to the vertical with further atmospheric values based on the Model S version from Christensen-Dalsgaard et al. (1996). The horizontal wavenumber $k_x = 1.372\,\mathrm{Mm}^{-1}$ is unchanged and determined by the lower turning point of the fast branch, namely at $z = -5$ Mm. The frequency used is f $= 5$ mHz, and the vertical grey line corresponds to the $a = c$ equipartition depth $z_{eq} = -297$ km. The points at where transmission is predicted to occur are outlined as red *star* points and their associated transmission values according to equation (2.15) are displayed.

The visualisation of the attack angle's effect is borne out best through ray analysis in

physical space, as is seen in Figure 2.2. When an incoming fast wave from below reaches the $a = c$ layer, the amount of transmission (conversion) realised is predicated heavily upon the angle at which the fast ray makes with the magnetic field. The small attack angle (middle panel) sees the majority of the energy transferring from the fast to slow branch. The continuing fast wave containing the remaining energy then reflects and interacts again with the $a = c$ layer to split its energy again into further fast and slow branches.

It should be remembered that the formula for the transmission coefficient $\mathcal{T}$ (see equation (2.15)) used to calculate the values in Figure 2.2 was introduced as an approximation based on setting the acoustic cut-off and Brunt-Väisälä frequencies to zero. Hansen and Cally (2009) tested this approximation against the exact solutions for a two-dimensional, isothermal, gravitationally stratified model with inclined magnetic field. Both were found to perform well against the exact solutions set out in Cally (2008), with the original form performing slightly better. The more condensed approximate form is consequently judged to be suitable for this analysis.

2.1.2 Shocks in MHD

Physical processes within the Sun and its overlying atmosphere create a plethora of disturbances, each producing their own sound waves. The vast majority of these will begin as subsonic disturbances. Their accompanying sound waves will propagate ahead of the disturbance, giving warning to the upcoming fluid of its arrival. This allows the reaction of the fluid to the arrival of the disturbance to be predominantly smooth and adiabatic. If on the other hand the initial disturbance is strong enough, the response will be supersonic. The ability for the accompanying sound wave to carry such information ahead of the local disturbance is then destroyed. This leads to a sharp and abrupt change of the physical conditions at the interface between disturbed and undisturbed fluid particles and the response is commonly referred to as a shock.

Some common major solar disturbances such as magnetic reconnection, prominence eruptions, solar flares, coronal mass ejections and even on smaller scales, surges and spicules, can be so powerful that shock waves can be produced almost instantaneously following their onset. Even the constant granulation of the Sun, a comparatively mild process compared to the aforementioned, can eventually produce shock waves. This process occurs mainly because as the sound waves travel outward from the interior of the Sun, they progress through a density profile which decreases significantly with height.
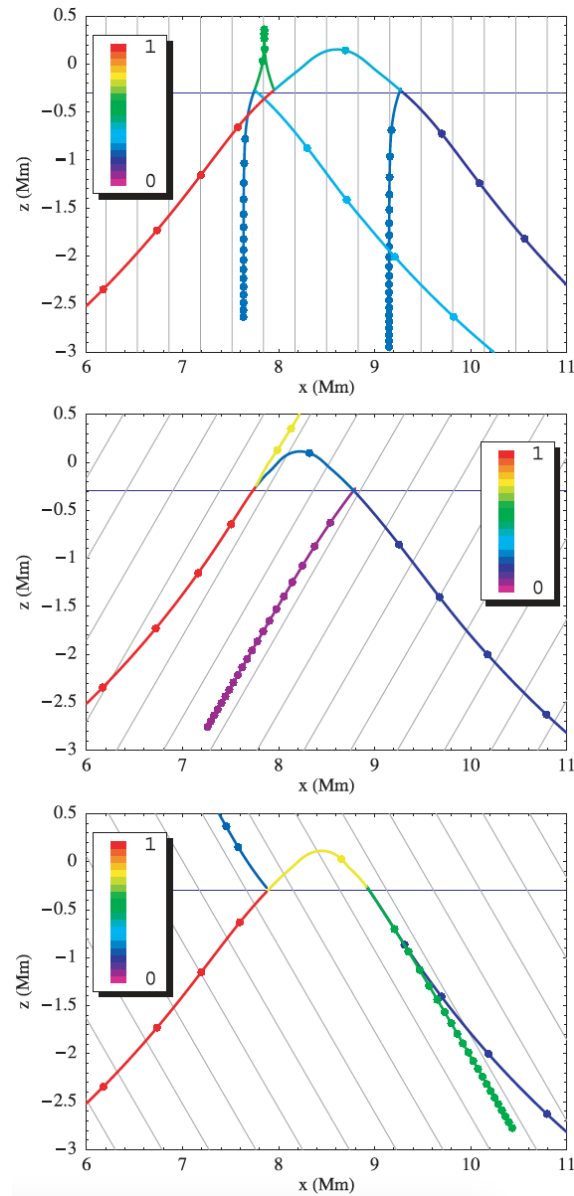
Figure 2.2: Physical space (x, z) ray path diagram from Schunker and Cally (2006) for a model atmosphere with 2 kG magnetic field inclined $0°$ (top), $+30°$ (middle), $-30°$ (bottom) from the vertical, as represented by the grey background lines. An incoming 5 mHz fast ray is injected from the bottom left into the atmosphere; the colour bar represents the energy remaining in each branch of the ray. The horizontal line represents the $a = c$ layer, the region where transmission takes place. The dots on each ray path represent 1-min travel time intervals.

The inverse relationship between density and the amplitude of the waves causes some previously subsonic waves to become supersonic and a shock is formed.

The layer between the shocked and unshocked fluid is referred to as the shock front and for MHD shocks, the thickness of the front is generally very narrow due to the balance between convective and dissipative effects. The gradients of pressure, density, velocity and temperature become so great at the front that dissipative processes such as viscosity or thermal conduction now start to play an important role. The shock front is in fact so narrow (a few mean free path lengths) that it is often modelled as a discontinuity of the fluid, though of course this is not achievable computationally.

For simplicity, this scenario is viewed from the rest frame of a shock travelling in the y direction with the shock-front lying in the (x, z) plane. The velocity and magnetic fields also lie in this same plane. The regions upstream and downstream of the shock are denoted by subscripts '1' and '2' respectively and are assumed to be non-varying in time and space. Thus, the area of interest can be localised to the immediate vicinity around the shock. By utilising the conservative form of the MHD equations along with Maxwell's equations, a further set of equations can be established to govern the shock as it travels through a chosen medium. Integrating these equations across the discontinuity (shock-front) produces a necessary set of conditions known as the jump or Rankine-Hugoniot conditions

$$\left(\frac{\gamma}{\gamma - 1} \frac{p_1}{\rho_1} + \frac{v_1^2}{2} \right) \rho_1 v_{y1} + \frac{v_{y1} B_{x1}^2}{\mu_0} - \frac{B_{y1}(B_{x1} \cdot v_{x1})}{\mu_0}$$
$$= \left(\frac{\gamma}{\gamma - 1} \frac{p_2}{\rho_2} + \frac{v_2^2}{2} \right) \rho_2 v_{y2} + \frac{v_{y2} B_{x2}^2}{\mu_0} - \frac{B_{y2}(B_{x2} \cdot v_{x2})}{\mu_0} \quad (2.16)$$

$$\rho_1 v_{y1} = \rho_2 v_{y2} \quad (2.17)$$

$$B_{y1} = B_{y2} \quad (2.18)$$

$$\rho_1 v_{y1}^2 + p_1 + \frac{B_{x1}^2}{2\mu_0} = \rho_2 v_{y2}^2 + p_2 + \frac{B_{x2}^2}{2\mu_0} \quad (2.19)$$

$$\rho_1 v_{y1} v_{x1} - \frac{B_{x1} B_{y1}}{\mu_0} = \rho_2 v_{y2} v_{x2} - \frac{B_{x2} B_{y2}}{\mu_0} \quad (2.20)$$

$$(\mathbf{v_1} \times \mathbf{B_1}) = (\mathbf{v_2} \times \mathbf{B_2}), \quad (2.21)$$

which have been applied in this context from as far back as De Hoffmann and Teller (1950). These equations allow for the solution of all six unknown quantities. Simplified cases involve parallel and perpendicular shocks, whilst the more general case of an oblique shock is further involved. Priest (1984) and Fitzpatrick (2014) both give concise descriptions of all three different types of MHD shocks, which are summarised below.

Parallel Shocks

A parallel shock is formed when the plasma flow direction is both parallel to the magnetic field and perpendicular to the shock front

$$\mathbf{v_1} = (0, v_1, 0) \quad \mathbf{v_2} = (0, v_2, 0)$$
$$\mathbf{B_1} = (0, B_1, 0) \quad \mathbf{B_2} = (0, B_2, 0)$$

(2.22)

and the upstream plasma velocity exceeds that of the sound speed $v_1 \geq c_1$. Or, by invariance, the propagation velocity of the shock through a stationary plasma must be supersonic. In this case, the magnetic field plays no role, $B_2 = B_1$ and the MHD shock is analogous to a purely hydrodynamic shock. All of the shocks discussed herein are compressive, in that the density of the shocked material is always greater than that of the un-shocked material. By substituting equation (2.22) into our jump conditions, the density ratio between the two,

$$X = \frac{\rho_2}{\rho_1} = \frac{(\gamma + 1)M_1^2}{2 + (\gamma - 1)M_1^2}$$

(2.23)

where $M_1 = v_1/c_1$ and $c_1 = (\gamma p_1/\rho_1)^{1/2}$, is always greater than unity. In fact, it can be demonstrated through the imposition of the second law of thermodynamics (the entropy of the closed system must never decrease) that $1 < X < \frac{\gamma+1}{\gamma-1}$. On the other hand, the pressure ratio,

$$Y = \frac{p_2}{p_1} = \frac{(\gamma + 1)X - (\gamma - 1)}{(\gamma + 1) - (\gamma - 1)X}$$

(2.24)

can increase without bound. Due to the limiting value of the compression ratio, as a shock increases in strength, the increase in pressure must be predominantly associated with an increase in temperature. The terms *strong* shock and *weak* shock are often used to refer to when $M_1 \gg 1$ and $M_1 - 1 \ll 1$ respectively.

Perpendicular Shocks

In the case of the perpendicular shock, the plasma flow direction must be both perpendicular to the magnetic field and the shock front

$$\mathbf{v_1} = (0, v_1, 0) \qquad\qquad \mathbf{v_2} = (0, v_2, 0) \qquad (2.25)$$
$$\mathbf{B_1} = (B_1, 0, 0) \qquad\qquad \mathbf{B_2} = (B_2, 0, 0).$$

The shock will form when the upstream plasma velocity is greater than the upstream *fast magneto-acoustic* speed $v_1 \geq (c_1^2 + a_1^2)^{1/2}$. In essence, the fast speed plays the same role

as the sound speed in the case of the parallel shock. The perpendicular shock however, will propagate across the magnetic field. Again, substituting equation (2.25) into the jump conditions now produces a quadratic in X

$$2(2 - \gamma)X^2 + \gamma[2(1 + \beta_1) + (\gamma - 1)\beta_1 M_1^2]X - \gamma(\gamma + 1)\beta_1 M_1^2 = 0, \qquad (2.26)$$

where $\beta_1 = 2\mu_0 p_1/B_1^2$ is the plasma beta, the ratio between gas and magnetic pressures. The solution is the real positive root of equation (2.26), and as a consequence, the limiting range for the density compression is once again $1 < X < \frac{\gamma+1}{\gamma-1}$. In the limit $\beta_1 \to \infty$, the solution reverts back to that of the hydrodynamic scenario given by equation (2.23). Further separating this case from the parallel shock, the magnetic field is now also compressed by the same quantity X. The pressure ratio

$$Y = 1 + \gamma M_1^2(1 - X^{-1}) + \beta_1(1 - X^2) \qquad (2.27)$$

can again increase without limit.

Oblique Shocks

An oblique shock describes any situation not covered by the aforementioned scenarios, specifically when the plasma flow direction is neither perpendicular nor parallel to the magnetic field or the shock front. This leads to the introduction of the angle θ, which is the angle subtended between the upstream plasma flow and the normal to the shock front, such that $v_{1y} = v_1 \cos\theta$. Calculations show that it is possible, and in fact convenient to transform into the de Hoffmann-Teller frame in which,

$$|\mathbf{v_1} \times \mathbf{B_1}| = 0 \qquad (2.28)$$

and it follows from equation (2.21) that

$$|\mathbf{v_2} \times \mathbf{B_2}| = 0. \qquad (2.29)$$

This frame is advantageous in that the upstream and downstream plasma flows are now parallel to the local magnetic fields in their respective regions. Substituting equations (2.28) and (2.29) into the original jump conditions, produces a new set of equations

$$p_1 \left(1 + \frac{c_1^2 X}{\gamma v_1^2(X - 1)} - \frac{X a_1^2[(\gamma + 1)v_1^2 - 2X a_1^2 \cos^2\theta_1]}{2(v_1^2 - \gamma a_1^2 \cos^2\theta_1)^2}\right) = p_2 \frac{c_1^2 X}{\gamma v_1^2(X - 1)} \qquad (2.30)$$

$$\rho_1 v_{y1} = \rho_2 v_{y2} \tag{2.31}$$

$$B_{y1} = B_{y2} \tag{2.32}$$

$$B_{x1}(v_1^2 - \cos^2\theta_1 a_1^2) = X^{-1}B_{x2}(v_1^2 - X\cos^2\theta_1 a_1^2) \tag{2.33}$$

$$v_{y1} = X v_{y2} \tag{2.34}$$

$$v_{x1}(v_1^2 - \cos^2\theta_1 a_1^2) = v_{x2}(v_1^2 - X\cos^2\theta_1 a_1^2) \tag{2.35}$$

The solution in X is now a real root of the cubic equation commonly referred to as the shock adiabatic

$$
(v_1^2 - X\cos^2\theta_1 a_1^2)^2 \left\{ [(\gamma+1) - (\gamma-1)X]\, v_1^2 - 2Xc_1^2 \right\} - X\sin^2\theta_1 a_1^2
$$
$$
\left\{ [\gamma + (2-\gamma)X] - [(\gamma+1) - (\gamma-1)X]\, X\cos^2\theta_1 a_1^2 \right\} = 0. \tag{2.36}
$$

The density compression ratio is once again limited as per the above shock types, $1 < X < \frac{\gamma+1}{\gamma-1}$. For a *weak* shock $X \to 1_+$, the real roots of equation (2.36) can be rearranged for v_1^2 to give

$$v_1^2 = \frac{a_1^2 + c_1^2 - [(a_1+c_1)^2 - 4\cos^2\theta_1 c_1^2 a_1^2]^{1/2}}{2} \tag{2.37}$$

$$v_1^2 = \cos^2\theta_1 a_1^2 \tag{2.38}$$

$$v_1^2 = \frac{a_1^2 + c_1^2 + [(a_1+c_1)^2 - 4\cos^2\theta_1 c_1^2 a_1^2]^{1/2}}{2}. \tag{2.39}$$

These should be familiar as they correspond to the velocities of the three linear MHD waves: slow, Alfvén and fast, respectively. The non-linear versions of which are termed the *slow* shock, *intermediate* shock and *fast* shock. The principal interest in this discussion lies in that of the slow and fast shocks and it can be shown through some algebra that the fast shock acts to refract the magnetic field away from the shock normal, whilst the slow shock has the opposite effect. Turning attention to the *strong* shock $X \to \frac{\gamma+1}{\gamma-1}$, the presence of multiple real roots to equation (2.36) is not always guaranteed. The fast shock solution is always viable, whereas the slow and intermediate shock solutions can vanish under certain scenarios. It is this crucial feature that will be revisited with further detail later in the chapter when applied to realistic shock simulations in a typical solar like atmosphere.

2.1.3 Motivation for Study

As described in Sections 2.1.1 and 2.1.2, both linear mode conversion as well as shock development and propagation of MHD waves have been well studied. However, the mixing of the two to give non-linear mode conversion of MHD shocks, is much less understood. Recently, Núñez (2019) presented an analysis based on the generalised ray theory of Cally (2008) and Schunker and Cally (2006) (see also Tracy et al. 2003) to argue that magnetoacoustic shocks passing through the layer where a and c coincide (the Alfvén-acoustic equipartition) not only split into fast and slow components as suggested by linear theory, but also that both the resultant outgoing fast and slow shocks are smoothed in the process. Núñez's argument is predicated on an assumption which is stated and not fully justified: *'Assuming that the passage through the conversion zone acts linearly in the waves, which is reasonable since they spend very little time there, we obtain the surprising result that the shocks which may be present in the incident wave are smoothed out in the outgoing ones, except for the single case of a pure transfer from a fast to a slow wave or vice versa.'* (Núñez, 2019, Conclusions)

This phenomenon is explored through 1.5-dimensional (1.5D) numerical simulation and accompanied theoretical discussion. The main questions addressed will be i) Does mode conversion still operate at $a = c$, as for linear waves? ii) Is it similarly dependent on the attack angle? iii) Are the transmitted and converted waves also shocks, or have they been smoothed?

2.2 Model

In active regions, the spatial extent over which the magnetic field is considered dynamically important is of the order of a few hundred kilometres, significantly smaller than a sunspot, which can have a diameter of tens of megametres. This demotes the variation in strength and inclination of the magnetic field to secondary importance and hence the field can be represented as locally uniform but inclined at some angle to the vertical. Owing to this, the simplest suitable model to explore the proposed phenomenon is adopted: an isothermal gravitationally stratified 1.5D atmosphere with uniform magnetic field $\mathbf{B} = B_0(\sin\theta, 0, \cos\theta)$ inclined at angle θ to the vertical. The effect of gravity is balanced by a decreasing density profile with height to achieve hydrostatic equilibrium. The magnetic field is chosen such that the Alfvén speed a equals the sound speed c at a

sufficient altitude that a fast (i.e. acoustic) wave injected at the bottom of the computational domain has enough space to shock before reaching the equipartition level $a = c$.

The computational box stretches 2.0 Mm both above and below the $z = 0$ height. The equilibrium density scale height is $h = 175.731$ km, the uniform sound speed is $c = 8.958$ km s^{-1}, the adiabatic index is $\gamma = 5/3$, and the magnetic field strength is $B_0 = 0.9$ kG oriented at angle θ to the vertical. The $a = c$ equipartition level is situated at height $z_0 = 125$ km. The acoustic cutoff frequency is $\omega_c = c/2h$, or 4.0 mHz. There is nothing particularly special about these values, though they are broadly characteristic of the active solar chromosphere. Changing B_0 simply moves the equipartition level up or down. Similar results may be expected for other stellar atmospheric models.

The numerical code used to solve the non-linear MHD equations is Lare2d (Arber et al., 2001). The grid is comprised of 8192 cells in the vertical direction, giving a resolution of 0.488 km.

A shock viscosity term is employed to avoid the Gibbs phenomenon whilst not artificially smoothing the shock front substantially. It can be seen that the shock fronts remain sharp where predicted throughout the simulations. An artificial cooling term is applied to avoid thermal runaway from shock heating, allowing the atmosphere to remain close to its initial profile. This term has the form of an exponentially weighted moving average, where the degree of weighting is set at $\alpha_w = 0.05$. When the cooling term is removed, the results show a $< 1\%$ difference within a scale height either side of the $a = c$ layer, the main area of interest.

Well approximated solutions for mode conversion and transmission are given in equation (2.15) and exact solutions for the linear case can be described via $_2F_3$ generalised hypergeometric functions as given in Hansen et al. (2015). The degree of transmission/conversion is based primarily on three conditions, the most important being the attack angle, the angle between the wave vector and the magnetic field. The smaller the attack angle through the layers around $a = c$, the more transmission occurs. In the most simple case with a vertically propagating wave through a vertical magnetic field, the attack angle is identically zero. Núñez (2019) is in agreement that an incoming acoustic shock-wave should remain unchanged except to transmit all its energy from the fast branch to the slow or vice versa. However, orientating the magnetic field away from vertical such as to give a non-zero attack angle should cause varying degrees of mode splitting. According to Núñez's analysis based on the averaging between Fourier modes of the outgoing waves,

the resulting fast and slow 'shocks' should be smoothed in the process.

Disentangling the fast and slow waves for analysis as they exit the $a = c$ layer requires looking into their governing natures and becomes easiest when the acoustic and Alfvén speeds are well separated. In the areas above $a = c$, the plasma beta β level decreases dramatically towards zero, hence magnetic pressure is dominating in this environment. The fast wave at this stage is predominantly magnetic in nature and its polarisation becomes ever more perpendicular to the magnetic field with height. Classically, the fast wave reflects at some stage in the chromosphere due to the ever-increasing Alfvén speed gradient but this is only true in the case where the wave vector isn't exactly vertical. In this case of a vertical wave, the fast wave travels upwards unhindered. The slow also propagates upwards unhindered but its travelling speed is significantly less than that of the fast wave. The slow wave also becomes more and more aligned with the magnetic field with height. These defining features allow for the two wave modes to be distinguished above $a = c$.

In accordance, both perpendicular and parallel-to-the-field plasma velocities $v_\perp$ and $v_\parallel$ are analysed. It should be noted that the measurements of parallel and perpendicular components are with respect to the actual (perturbed) magnetic field and not the original equilibrium field. This is important as the propagating shock front acts to compress the plasma by up to a factor of 4 and given that the field lines are tied to the plasma, the magnetic field inclination can be greatly perturbed. In line with this, the density ρ scaled by the equilibrium density $\rho_0(z)$ is tracked throughout the simulations and presented accordingly.

2.3 Results

A wave driver is implemented at the bottom of the computational box $z = -2.0$ Mm and acts to deliver an angular-frequency-ω_0 half-period sinusoidal pulse of vertical velocity with amplitude V_0. This is essentially just adding a source term to the momentum equation for MHD. The proposed driver creates a wave with purely vertical wave vector. The plasma velocity disturbance is also initially vertical. It does not begin to deviate significantly from vertical until such a height that the plasma beta has decreased enough to allow the pressure imparted by the inclined magnetic field to have a non-negligible effect. The frequency chosen is twice that of the acoustic cut-off value $\omega_0 = 2\omega_{ci} = 8.0$ mHz. In frequency

space, this corresponds to the broad frequency spectrum

$$\tilde{F}(f) = -f_0 \left[\frac{\cos(\pi f/2 f_0)}{(f^2 - f_0^2)\pi} \right], \tag{2.40}$$

which is centred around zero, where $f = \omega/2\pi$. It is important to note that the acoustic cut-off phenomenon only allows frequencies above 4 mHz to propagate upwards in this atmosphere. This is due to the acoustic cut-off providing an upper boundary to the p-mode cavity; the lower boundary lies at a depth inside the Sun where the horizontal phase speed of the wave equals that of the local sound speed. Waves with frequencies below this value become evanescent and are spatially confined to this cavity (Jiménez et al., 2011). A Fourier analysis of the frequency components confirm this numerically to be the case. To confine the frequency spectrum more closely to a single frequency, a piston like driver running over several wave periods can be implemented. However, this would further introduce a variety of numerical complications. Each shock would act to perturb the atmosphere in such a way that the following shock would be interacting with what is essentially a different atmosphere, and most importantly one that would be notably different to the initial equilibrium setup. Given the large amplitudes required to produce shocks at these heights, reflection of waves off the top of the computational box becomes prominent and difficult to alleviate numerically. Any returning waves are consequently artificial and act to complicate the behaviour around the area of interest. For the most succinct results, the half-period driver is found to perform the best. It can be seen from the resulting figures that very clean shocks are created from a broad spectrum of frequencies above f_c.

Kalkofen et al. (1994) have discussed the evolution of linear and nonlinear waves in non-magnetic 1D isothermal atmospheres. The wakes produced by the initial pulse follow each other by typically one acoustic cut-off period f_{ci}^{-1}, supporting the theory that the atmosphere rings at the acoustic cut-off frequency. The results obtained through these simulations are restricted to tracking the initial pulse produced by the 8.0 mHz driver and hence this effect should not interfere significantly. Kalkofen et al. also describe the various non-linear effects associated with a piston like driver such as shock merging, another reason why a single half-period pulse is implemented.

The velocity perturbation increases exponentially with height until a shock is formed well below the $a = c$ layer. When the magnetic field is vertical, the shock front remains sharp throughout the entire simulation and travels unhindered through to the top of the
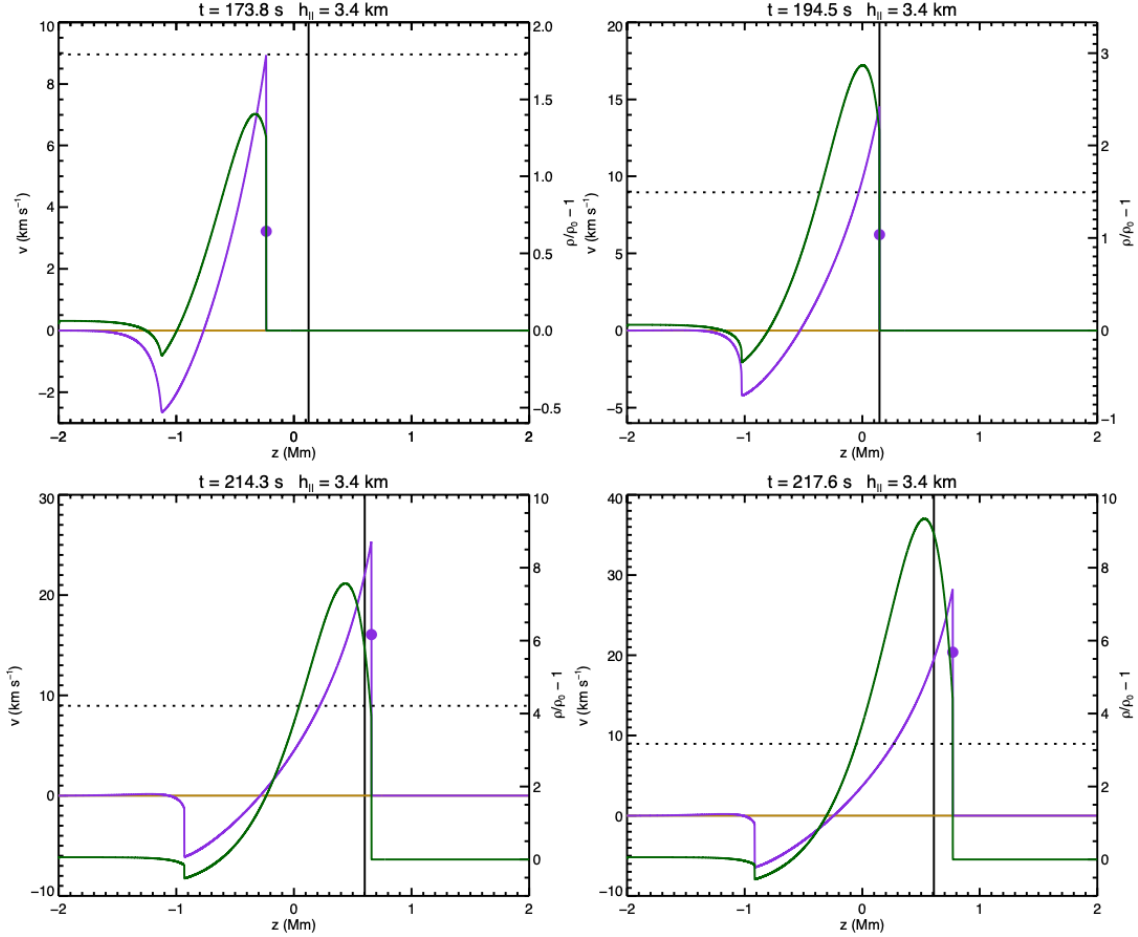
Figure 2.3: $\theta = 0°$: The purple solid line, gold solid line (zero in this case) and green solid line correspond to $v_\parallel$, $v_\perp$ and $\rho/\rho_0 - 1$ respectively. The shock front is formed and travels through the $a = c$ layer unaltered. The solid vertical line is where $a = c$, which moves in response to the incident wave. The black dotted horizontal line is the equilibrium sound speed. The purple dot indicates the steepest point in the acoustic shock. The top-right panel indicates that the shock reaches the conversion layer with almost-maximal density contrast ($X = 4$).

computational box, as expected (Figure 2.3). Increasing θ, the angle of the magnetic field from vertical, produces a splitting of the wave into its slow and fast components around the $a = c$ layer. When $a > c$, the fast wave accelerates out in front of the slow wave and the two wave types can be easily distinguished.

The choice is made to look separately at velocities both parallel and transverse to the (actual) magnetic field. This separation allows an approximation of the two wave types, however it is not precise. This can be seen by the fast wave appearing in the parallel velocity for $\theta > 0$, and vice versa for the slow wave.

Another important component is the in-place density compression ratio ρ/ρ_0, where ρ is the density value at the given time and ρ_0 is the initial background density value at the same spatial position. This is not the same as the classical shock-jump compression ratio $X = \rho_2/\rho_1$ from the pre-shock to post-shock regions ('1' and '2' respectively), though they do correspond immediately after a shock front passes. For an oblique compressive shock, where the magnetic field is not completely perpendicular to the shock front, the limiting compression ratio when $\gamma = 5/3$ is 4 (Priest, 1984). For these simulations, this remains true across the shock front as expected; however the values behind the front can exceed this ratio due to the transport of fluid via the propagating shock. Deeper, higher density fluid is carried upwards and is then related to the original density values of greater heights giving the appearance of a much higher compression ratio. To eliminate this, the movement of each fluid particle would need to be traced throughout the simulation and the densities compared to those at their original equilibrium height, which is an unnecessary complication.

A non-zero attack angle gives rise to the splitting of the fast and slow components around $a = c$. However both the fast and slow shock remain sharp in the simulations when θ is less than about $15°$. At angles increasingly larger than $15°$, it becomes easier to see the smoothing of the slow component as it separates from the fast shock and traverses the layers around $a = c$. As the slow wave exits the $a = c$ layer, it begins to steepen again to 're-shock', best seen in Figure 2.4. Conversely, the fast shock remains sharp throughout and continues to propagate through the atmosphere unaltered in its form. Again, it does not reflect off the Alfvén speed gradient because of its purely vertical wave vector.

Figures 2.4, 2.5, 2.6 and 2.7 show the evolution of the $\theta = 15°$, $30°$, $45°$, and $60°$ cases respectively. It can be seen that the greater the value of θ, the more smoothing of the slow component is realised. To quantify this, a measurement related to the steepness of the slow
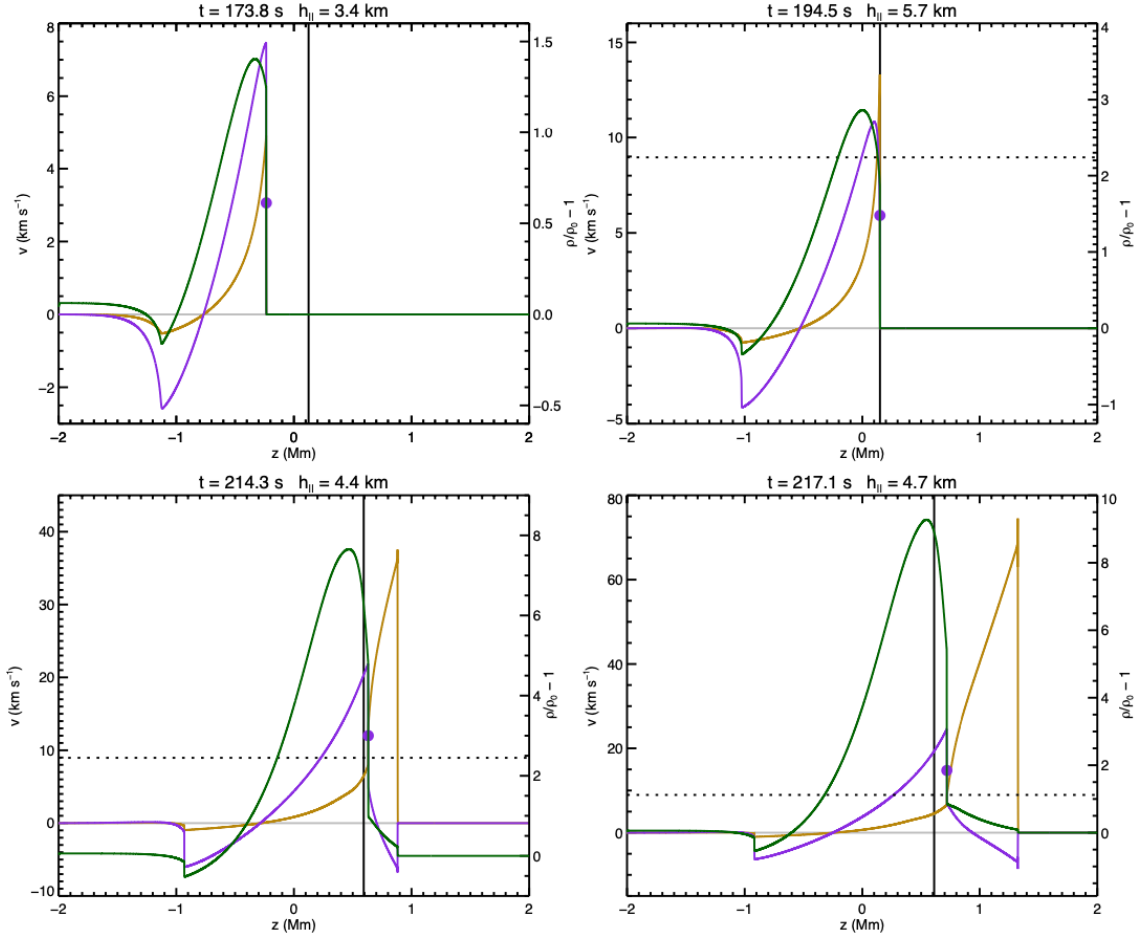
37

Figure 2.4: $\theta = 15°$: At the $a = c$ layer, the slow shock is smoothed slightly, before steepening again to produce another shock front. The fast shock remains sharp and propagates unaltered. The purple dot shows the location of the steepest point in the slow shock.

shock at its inflection point is introduced. The purple dot displayed on each 'shock' front corresponds to the inflection point of $v_\parallel$ at the given time and consequently delineates the steepest part of the shock. At each of these points, the value of the 'velocity scale height' $h_\parallel$[1] is given above each panel, defined as

$$h_\parallel = \left| v_{\parallel,\text{max}} \middle/ \left(\frac{dv_\parallel}{dz} \right) \right|, \tag{2.41}$$

---

[1]The values of $h_\parallel$ given in Figures 2.3, 2.4, 2.5, 2.6 and 2.7 were calculated using a different algorithm than that in Pennicott and Cally (2019) and consequently differ in value. The results are however, qualitatively the same.
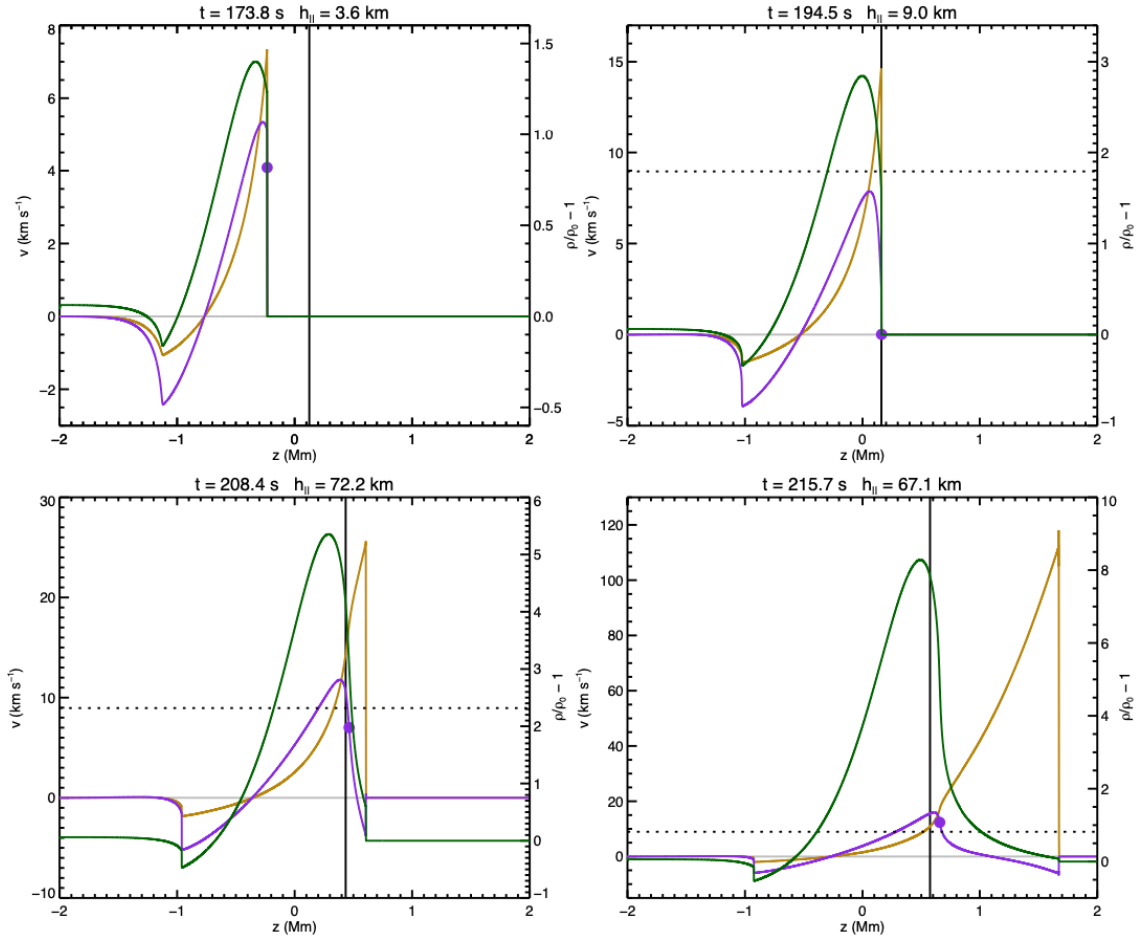
Figure 2.5: $\theta = 30°$: At this stage, the increased magnetic field inclination produces an easily identifiable smoothing of the slow shock around $a = c$ before beginning to steepen again. Again, the fast shock remains sharp and propagates freely.

which is a measure of shock steepness. A small $h_\|$ corresponds to a steep shock front, the value of which is limited numerically.

Figure 2.4 represents the case of the lowest angle of incidence in which smoothing of the slow shock can be visualised, however smoothing is predicted to occur for any non-zero angle of incidence. Figure 2.8 provides a visualisation of the velocity scale height for incident angles as low as $5°$, showing that this is indeed the case.

Núñez (2019) makes the assumption that the passage through the conversion zone around $a = c$ acts linearly on the waves. This is supposedly owing to the fact that the waves spend such little time in this area. However, as seen in Figure 2.9, the incoming shock front is strong enough to drag the $a = c$ layer along with it, which can increase in height
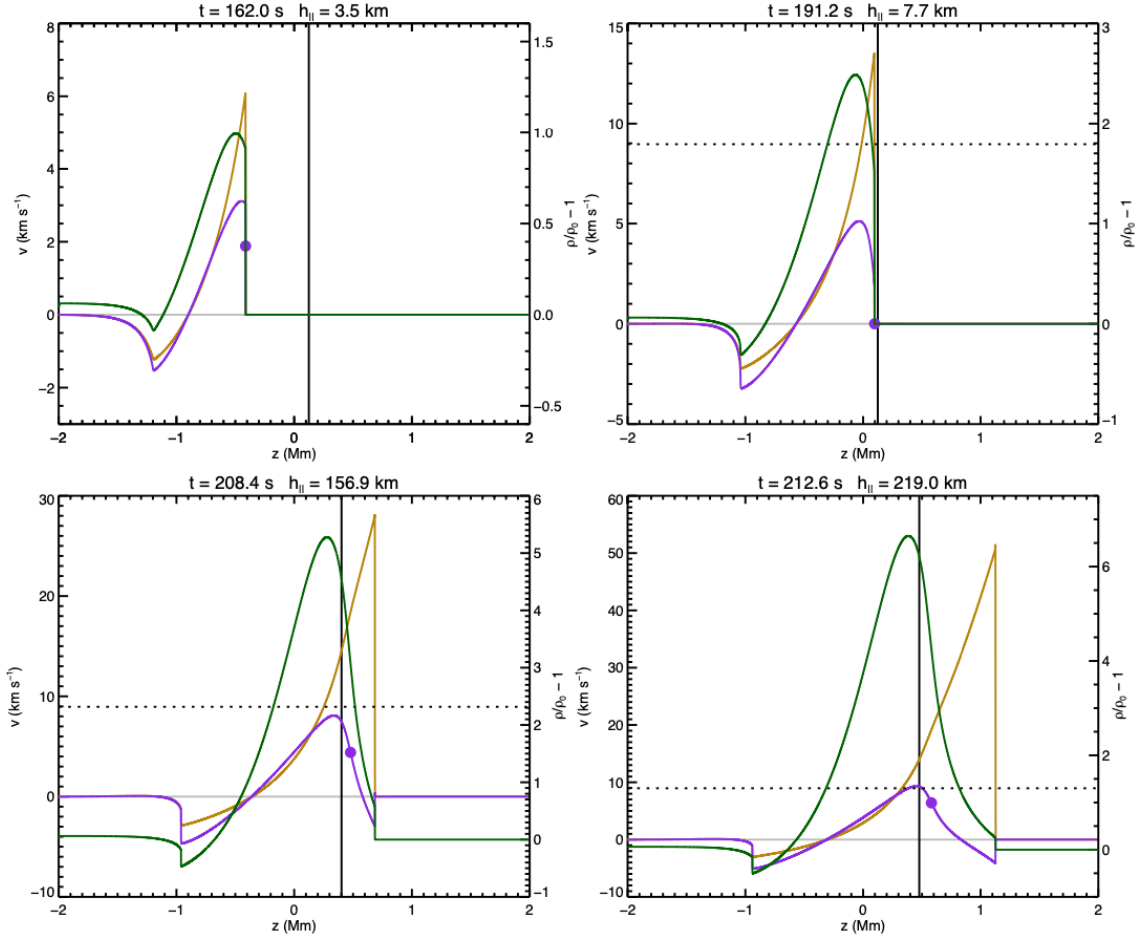
Figure 2.6: $\theta = 45°$: With the magnetic field angle continually increasing, the smoothing of the slow shock becomes quite evident. Having exited the $a = c$ layer, the slow wave will require more time before it is strong enough to steepen again into another shock. Again, the fast shock remains unchanged in its form.

by up to 400 km for low θ. This means the shock front itself can spend multiple seconds in close proximity to the mode conversion region. In fact, it takes quite a substantial amount of time before the slow wave completely separates itself out from the area around $a = c$.

2.4 Discussion and Conclusion

1.5D simulations were conducted using a base-driven 8.0 mHz half-period sinusoidal pulse injected into an isothermal, gravitationally stratified atmosphere with the angle the magnetic field makes from vertical being varied from $\theta = 0°$ to $60°$. The driver produces
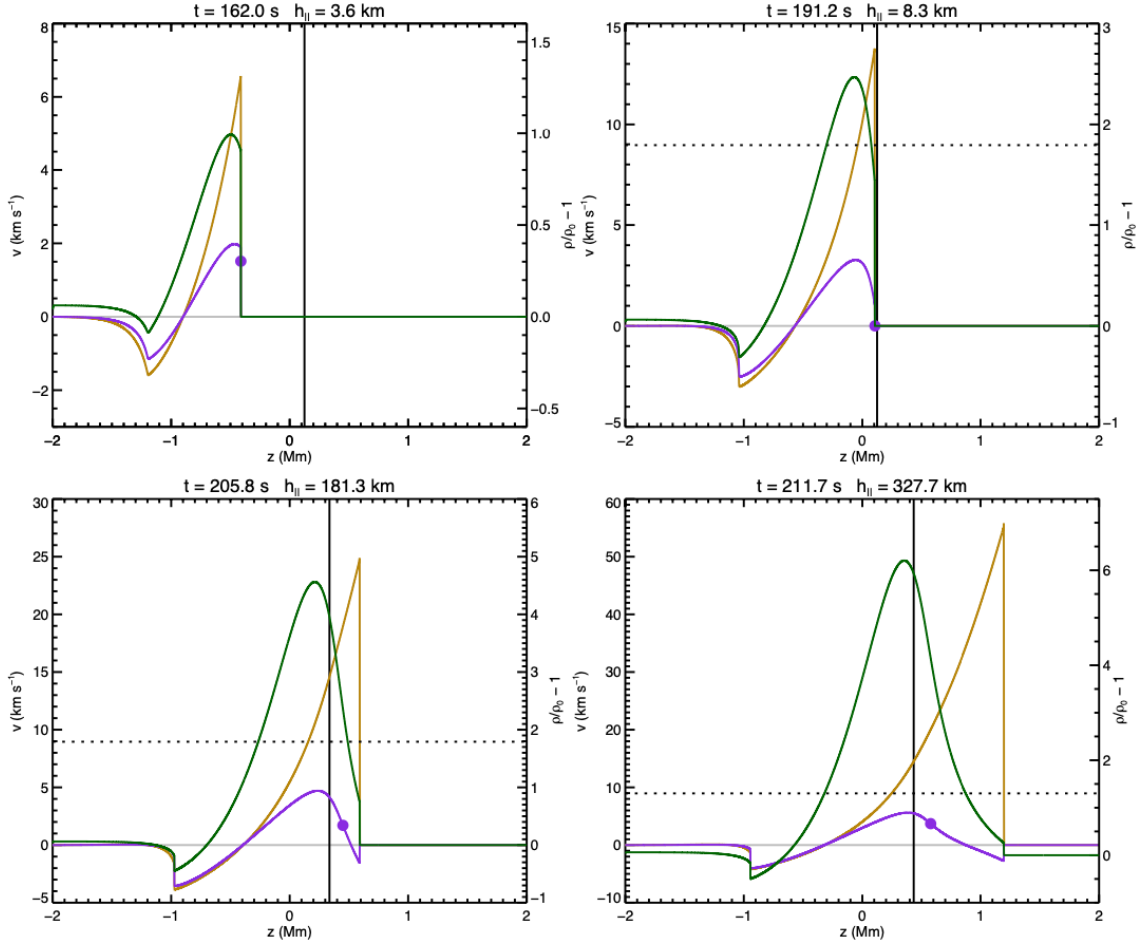
Figure 2.7: $\theta = 60°$: Heavy smoothing of the slow shock through $a = c$. The transmitted slow wave is subsonic and much too weak to re-shock before the fast shock reaches the top of the computational box. The fast shock remains sharp and propagates freely again.

a broad frequency spectrum, however due to the acoustic cut-off effect, only frequencies above 4 mHz progress into the area of interest. The perturbation is allowed to freely evolve with the constantly decreasing density profile causing a shock to be formed well below the Alfvén-acoustic equipartition ($a = c$) layer. When the attack angle α between the (vertical) wave vector $\mathbf{k}$ and magnetic field is zero, a typical parallel shock is formed as described by equations (2.22), (2.23) and (2.24). This shock continues to travel upwards unimpeded, growing in amplitude with the decreasing density profile, as expected. When α is non-zero, the shock splits into its slow and fast components around $a = c$. When $\theta \gtrsim 15°$, the passage of the slow shock through this layer is accompanied by an appreciable smoothing. Angles less than this (but greater than zero) have been shown numerically
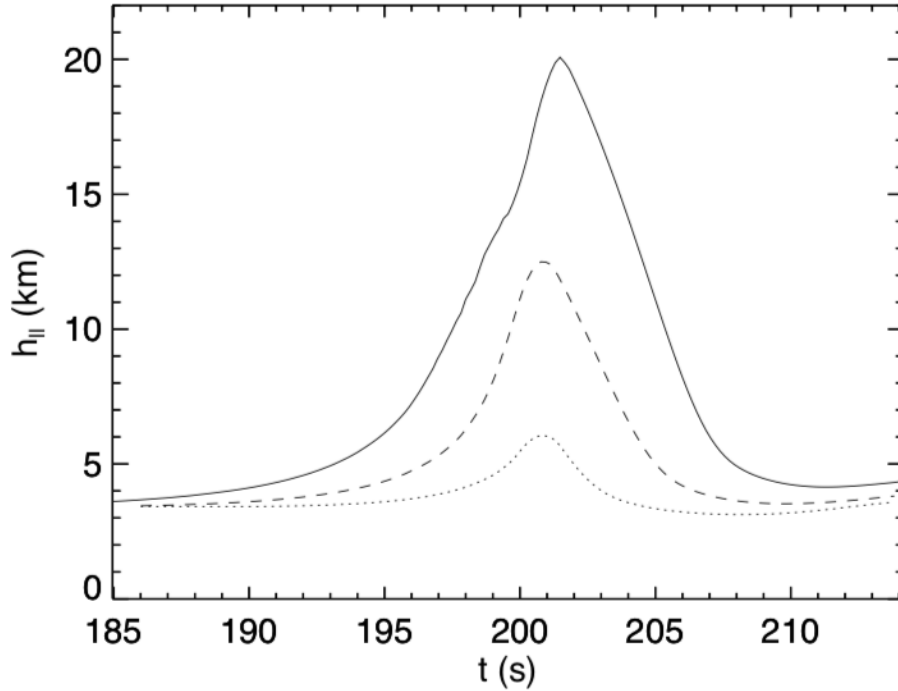
Figure 2.8: Values of $h_\parallel$ for magnetic field inclinations $5°$ (dotted line), $10°$ (dashed line), and $15°$ (solid line) as the slow wave progresses through the layers around $a = c$. Smoothing (increase in $h_\parallel$) is apparent even at small angles of incidence.

to incur at least some degree of smoothing. As the smoothed slow wave leaves this area and continues to propagate upwards, it begins to re-shock. The fast shock on the other hand always continues to propagate freely through the atmosphere without any smoothing, regardless of the value of θ. This is in only partial agreement with Núñez (2019), who stated that both the fast and slow components of the shock should be smoothed.

One possible reason for this discrepancy is that the $a = c$ layer is dragged along by the shock. This causes the time over which transmission occurs to increase and makes the interaction intrinsically non-linear. The Fourier series that Núñez uses to characterise the transmitted waves is based on the linear conversion hypothesis.

Even without the above effect, a different mathematical approach suggests further differences. Whilst no formulae (exact or otherwise) exist for non-linear transmission calculations, looking to the exact linear transmission coefficients $\mathcal{T}$ as given by Cally (2008) is insightful. Figure 2.10 shows these values for a vertical wave in an isothermal atmosphere as a function of frequency measured relative to the acoustic cut-off frequency for a range of representative field inclinations. All waves with frequencies below the
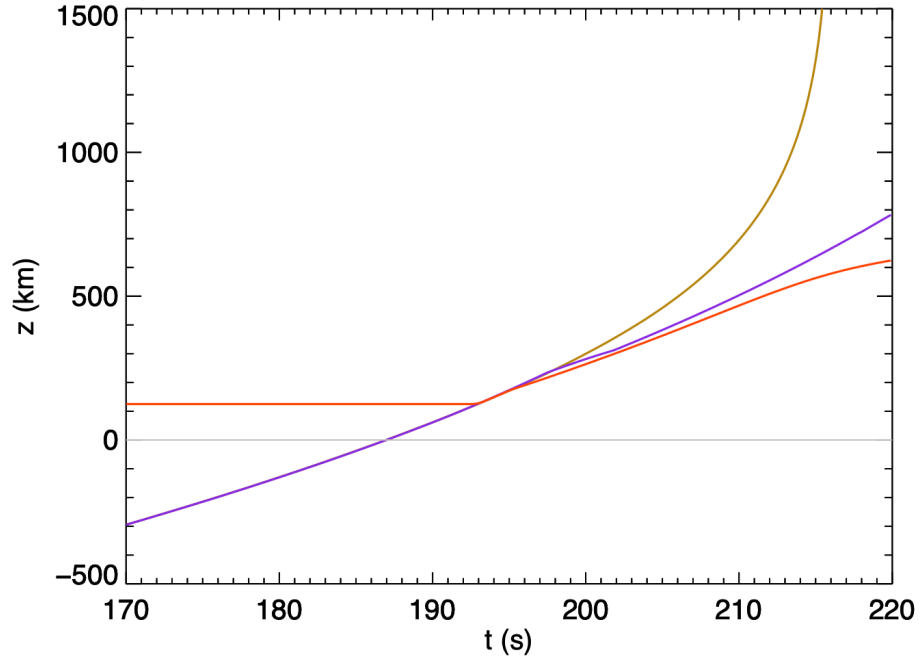
Figure 2.9: Time-distance plot showing the evolution of the $a = c$ layer (orange) along with the 'shock' as seen in $v_\parallel$ (gold curve) and $v_\perp$ (purple curve) for the $\theta = 30°$ inclined magnetic field. The $a = c$ layer is seen to be advected along with the shock for several seconds as it passes through. The slow component stays within close proximity to $a = c$ for a significant period of time.

acoustic cut-off are evanescent, which describes their absence. For the situation at hand, the transmission coefficient $\mathcal{T}$ gives a measure of the fraction of energy transferring from the fast wave into the slow wave around $a = c$. A shock wave discontinuity can be modelled by a Fourier Series, which will be pointwise convergent as described by Chernoff (1980). This series will be composed of high-order Fourier modes with amplitudes asymptotically proportional to the inverse of the vertical wavenumber k_z, where k_z is proportional to ω via a dispersion relation. It can be seen from Figure 2.10 that as the angle θ (equivalent to the attack angle α for a vertical wave) increases, the individual wave components are transmitted less and less. This is especially true for high frequencies and as a consequence, it should come as no surprise that the resulting outgoing wave tied to the slow shock is smoothed. Any high frequency Fourier modes not being transmitted are however not lost and are in fact converted to the fast wave, allowing the fast shock to persist. Recall that due to the conservation of energy, $\mathcal{C} = 1 - \mathcal{T}$. This analysis fits consistently with the results obtained via simulation. The advection of the $a = c$ layer with the shock could only act to
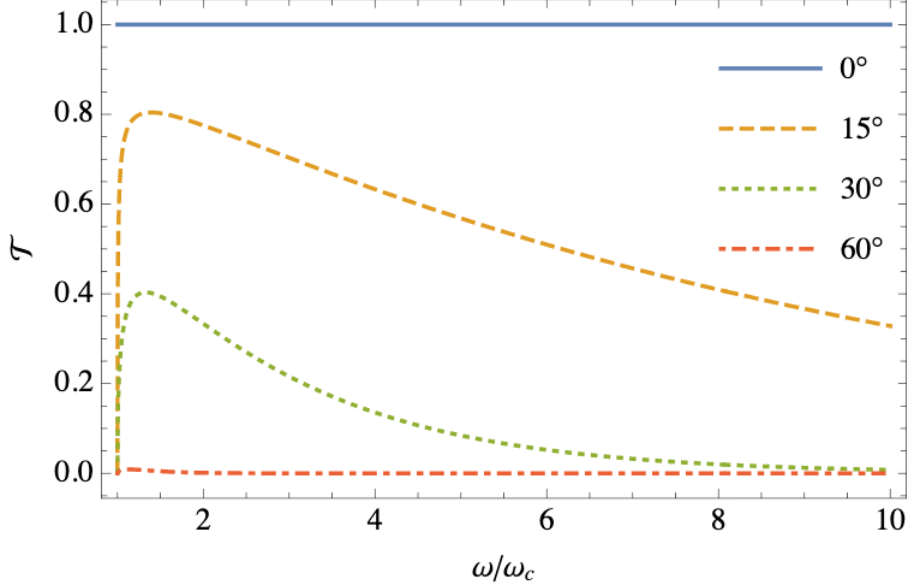
amplify this effect.

Figure 2.10: Exact linear transmission coefficients $\mathcal{T}$ for vertical waves in an isothermal atmosphere as a function of frequency measured relative to the acoustic cut-off frequency. The curves are for magnetic field inclinations $\theta = 0°, 15°, 30°$ and $60°$ from vertical (top to bottom). An adiabatic index of $\gamma = 5/3$ is used.

The approximate WKB-based formula for transmission described previously is adjusted for the current simulation parameters to give $\mathcal{T} \approx \exp[-\pi \mathbf{k} h_z \sin^2 \theta]_{a=c}$, which lends further support to the above conclusion. $\mathcal{T} \to 0$ exponentially with increasing $|\mathbf{k}|$ (or equivalently, increasing ω), faster for greater values of θ. This is perfectly in line with the above discussion and the simulation outputs. Whilst the size of the $a = c$ conversion layer remains unchanged, the advection of this layer would also effectively increase h_z, which is a measure of the thickness of the conversion layer, further dampening the transmission values.

Further investigation can be explored in relation to the solutions available for the aforementioned shock adiabatic (2.36). This is a bi-cubic polynomial describing the evolution of an oblique shock in a uniform medium, pertinent to when $0° < \theta < 90°$. The atmosphere used in these simulations is stratified vertically, however the adiabatic should give a good local description at the shock front. Figure 2.11 shows the solutions to the shock adiabatic for the case when $\gamma = 5/3$, $\theta = 30°$, $c = 8.958$ km s^{-1} and four nominal Alfvén speeds a, corresponding to results in Figure 2.5. In each case, the upper curve

corresponds to the fast shock. The lower curve is split into two branches: the lower branch represents the slow shock, whilst the upper branch represents the intermediate (Alfvén) shock. The intermediate shock is not excited through these simulations and can be ignored. Although the full solutions to the fast shock exceed the plotted domain, it occurs that there is a solution for all $1 < X < 4$, regardless of the local Alfvén speed. However, the solution to the slow shock is absent whenever X is to the right of its loop. As the Alfvén speed increases with height in the atmosphere, a wider range of X permits a solution and consequently a slow shock can redevelop under these conditions.
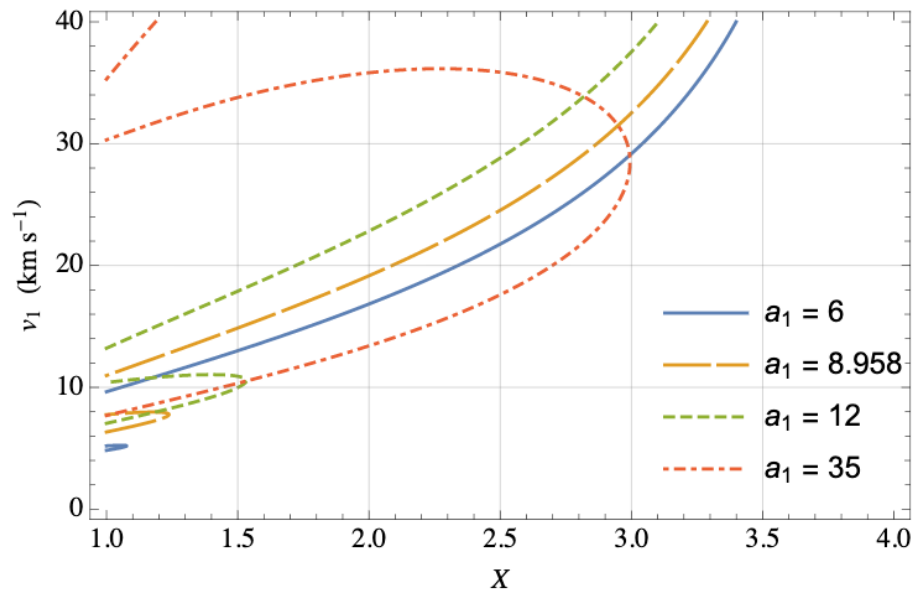

Figure 2.11: Solutions to the shock adiabatic as a function of density compression ratio X and shock speed v_1 for $\gamma = 5/3$, $\theta = 30°$, $c = 8.958$ km s^{-1}, and four nominal values of Alfvén speed a: 6 km s^{-1} (full blue), $c = 8.958$ km s^{-1} (long-dashed orange), 12 km s^{-1} (short-dashed green), and 35 km s^{-1} (dot-dashed red).

Upon exiting the conversion layer, the Alfvén speed will begin to exceed that of the sound speed, where a typical case could correspond to the dashed green curve in Figure 2.11, with $a = 12$ km s^{-1}. At this point, if the density compression ratio of the fluid $X \gtrsim 1.53$, there is no available slow shock solution. This matches with what is seen in the lower panels of Figure 2.5, in that a strong density compression is co-spatial with the slow wave and no shock is present. The fast shock remains because the fast shock always has a solution, regardless of the value of X. As the fast shock propagates higher into the atmosphere, X becomes closer to 1 and thus it travels at a speed only just above that of the

local Alfvén speed a.

The incident shock is primarily acoustic in nature within the deeper layers where $a < c$. However, upon reaching the conversion layer, the injected wave splits into its fast and slow components and the vast majority of the fluid's density compression is seen to be consistently associated with the slow wave, regardless of the value of θ. Above $a = c$, the slow wave now exhibits strongly acoustic characteristics and separates out spatially from the fast wave. The acoustically dominated slow wave travels ever more parallel to the magnetic field with height and acts to compress the fluid, hence the slow wave is primarily associated with the increase in X. Conversely, the fast wave is now predominantly magnetic in nature, travelling more and more transverse to the magnetic field and consequently becomes less capable of compressing the fluid, which is tied to the field. In actuality, in the $a \gg c$ limit, the fast wave becomes completely incompressive.

Irrespective of the above arguments, it is clear that the numerical results show the slow wave in $a > c$ being strongly aligned with the density compression of the fluid. There is no corresponding solution to the shock adiabatic at such high density compression value X for the slow wave until much higher in the atmosphere, such as that corresponding to the 35 km s^{-1} lobe in Figure 2.11.

2.5   Implications and Further Research

The parameters for the simulations were broadly characteristic of the solar photospheric and chromospheric layers, and in turn, related stellar atmospheres. The smoothing of the acoustic shock necessitates a loss of higher order Fourier components and consequently, a loss of energy. This occurs around the equipartition layer within the lower chromosphere and may impact on the amount of energy being transferred to the upper chromosphere or further into the corona. If these Fourier components are transmitted to the fast branch, the fast shock will consequently carry more energy with it. Any extra energy has the potential to enhance fast-Alfvén conversion at appropriate heights.

The most obvious avenue for further research is the extension of the setup into atmospheres encompassing further spatial dimensions. Firstly, a 2-dimensional (2D) extension will allow for a non-zero horizontal wavevector k_x to be associated with the injected wave. Transmission/conversion co-efficients are well known for all $k = \sqrt{k_x^2 + k_z^2}$. For different k_x, the degree of smoothing can be predicted and then investigated in relation to the amount

of transmission through the $a = c$ layer. Further to this, the non-zero k_x will bring with it an associated fast wave turnover height. The purely vertical waves investigated here travel upwards unhindered, however this introduction will cause fast waves of differing frequencies to act independently at varying heights. The effect of this will be to redistribute some of the wave energy, which is currently associated entirely with the vertical wave in all the simulated cases.

A 2.5 or 3-dimensional atmosphere would further permit the production of intermediate (Alfvén) shocks to be incited, a whole subtype of shock which was introduced briefly but not investigated herein.

Most recently, a study by Snow and Hillier (2020) has already extended the work presented here to investigate the role of two-fluid effects on shocks in a partially-ionised isothermal gravitationally stratified atmosphere. An upwards propagating shock may travel through the lower solar atmosphere where the fluid is predominantly neutral and enter the upper solar atmosphere where the fluid is almost fully ionised. Neutral and ionised species have different pressure scale heights, causing a 2-fluid wave to propagate slower and steepen more than the MHD shocks investigated here. Their results show that the mode-conversion point, shock width and shock transitions all depend on the collisionality of the system, governed by the coupling strength between neutral and plasma species. These identifying features provide the potential to observe two-fluid effects from within the lower solar atmosphere and further progress the understanding of shock propagation and conversion through this area.

Chromospheric Resonances in Sunspot Umbrae

3.1 Introduction

3.1.1 MHD Waves and Oscillations in Sunspots

Sunspots and other magnetically active regions have long been an important area of interest for studying magnetohydrodynamic (MHD) waves and oscillations in the solar atmosphere due to their array of magnetic field geometries and strengths. Their presence in sunspots has been known of for at least 50 years (Beckers and Tallant, 1969) and a vast amount of data and ensuing interpretations are starting to pile up. MHD oscillations and waves within sunspots have been the primary focus of a collection of reviews in the solar literature (Moore, 1981; Staude, 1991; Bogdan, 2000; Khomenko and Collados, 2015; Sych, 2016). The sunspot structures themselves are also home to their own assortment of reviews, which encompass everything from observational points of view (Borrero and Ichimoto, 2011) through to the latest theoretical and numerical models being employed (Rempel and Schlichenmaier, 2011; Rempel, 2012).

Measurements of wave properties are generally confined to spectroscopic or direct imaging instruments, both of which can be ground or space-borne and a good review of the observational trends is given by Banerjee et al. (2007). Many spectroscopic telescopes such as The Solar Optical Telescope (SOT) on-board Hinode (Tsuneta et al., 2008) or the Triple Etalon SOlar Spectrometer (TESOS) operated at the German Vacuum Tower Telescope

(VTT) (Tritschler et al., 2002) are used to observe spectral lines simultaneously at different heights above the solar surface, providing details of wave phase relations, amplitudes and line-of-sight velocities spanning a wide distribution of frequencies. These observations are based solely on time-series recordings of the variations of the four Stokes parameters (also known collectively as the Stokes vector or profile), a set of values describing the polarisation state of electromagnetic radiation. Any given spectral absorption line - of which there are thousands in the solar atmosphere known as the Fruanhofer lines - can have its Stokes parameters observed and recorded over time. These values describe the absorbed radiation through intensity (Stokes I), linear polarisation (Stokes Q & Stokes U) and circular polarisation (Stokes V). The various physical conditions of the solar atmosphere, such as the fluid velocity, are then inferred through inversions of these line profiles. This is done essentially through a best-fitting process of a synthesised line to that of an observed line. Accurate measurements of temporal Doppler velocity fluctuations at the photosphere have historically proven difficult to obtain because of their low amplitudes, however, space-based missions have begun to offer reliable readings (Nagashima et al., 2007). Conversely, moving upwards through the chromosphere, the fluctuations grow in amplitude due to the decreasing atmospheric density and are readily observed at heights up to and including the corona (Verwichte et al., 2010).

Due to the abundance of elements and simple molecules present in the solar atmosphere, there exists a plethora of line profiles which can be read, corresponding to a range of atmospheric temperatures (heights). Near the relatively cool photosphere it is common to view OH, CO, CaH, Fe I, Ca I, K I, Mg I and Na I line profiles, whilst in the hotter chromosphere, Hα , Hβ , He I, C, N, O, Ne, Mg, Si, Ca, Fe are frequently used, amongst others (O'Shea et al., 2001; Banerjee et al., 2002; Rendtel et al., 2003). Simultaneous measurements of different lines allow for measurements of spatial and temporal coherence between oscillations at various heights.

Owing to extensive observation, radio waves with frequencies as low as a few mHz (Gelfreikh et al., 1999) and as high as those associated with hard X-rays (Wang et al., 2002) have been recorded in sunspots and active regions. The velocity spectra resulting from these observational measurements contain peaks at distinct frequencies. The dominating frequencies in and around sunspot atmospheres are generally measured to be between 1-8 mHz (Kolobov et al., 2016; Löhner-Böttcher and Bello González, 2015; Khomenko and Collados, 2015; Sych and Nakariakov, 2014), the variation of which has been strongly

linked with the orientation of the local magnetic field (Reznikova and Shibasaki, 2012; Yuan et al., 2014). A particularly stark difference in measured frequencies of sunspot umbrae is the dominating signals at the photosphere peaking around 3-3.5 mHz and those through the chromosphere, which exhibit higher frequencies around 5.5-6.5 mHz (see Figure 3.1). This pattern is also observed in the quiet Sun regions, the main difference being the reduced overall power observed in sunspots, often by a factor of two or three (Kumar et al., 2000; Finsterle et al., 2004).

Various analytical and numerical models and methods have been used to study the propagation of MHD waves, all of which have been extensively discussed throughout the available literature and can be seen for example in Murawski (2002). Current solar models now encompass layers as deep as the sub-photosphere (Shelyag et al., 2009) and as high up as the corona (Santamaria et al., 2015). Due to the myriad of magneto-acoustic waves that can be imparted, a large discussion would need to ensue to discuss these individually with any depth. The chromosphere is also home to the equipartition layer z_{eq} where slow-fast wave conversion/transmission takes place, along with fast-wave reflection and fast-Alfvén wave conversion. These have all been introduced earlier and the reader is referred to the introduction for further insight. This study looks to simulate only field-aligned acoustic modes and as such, the discussion is limited to reflect this as much as possible.

3.1.2 Magneto-acoustic Cut-off Effect

As the production of waves being measured in sunspot atmospheres is heavily confined to subsurface interactions, the fact that waves of different frequencies dominate in different areas suggests a physical process exists whereby waves of different frequencies are preferentially filtered out as they propagate through the layers above the solar surface. The notion of an acoustic cut-off frequency as a fundamental property of stratified mediums was first introduced by Horace (1909), who described the formula for an isothermal atmosphere as

$$\omega_{ci} = \frac{c}{2H}, \tag{3.1}$$

where c is the sound speed, $H = c^2/(\gamma g)$ is the pressure scale height, γ is the co-efficient of specific heats, and g is the acceleration due to gravity. Any waves with frequencies $\omega < \omega_{ci}$ will become evanescent in these regions and prolonged propagation through such areas will lead to these waves being filtered out completely. It is this effect which can
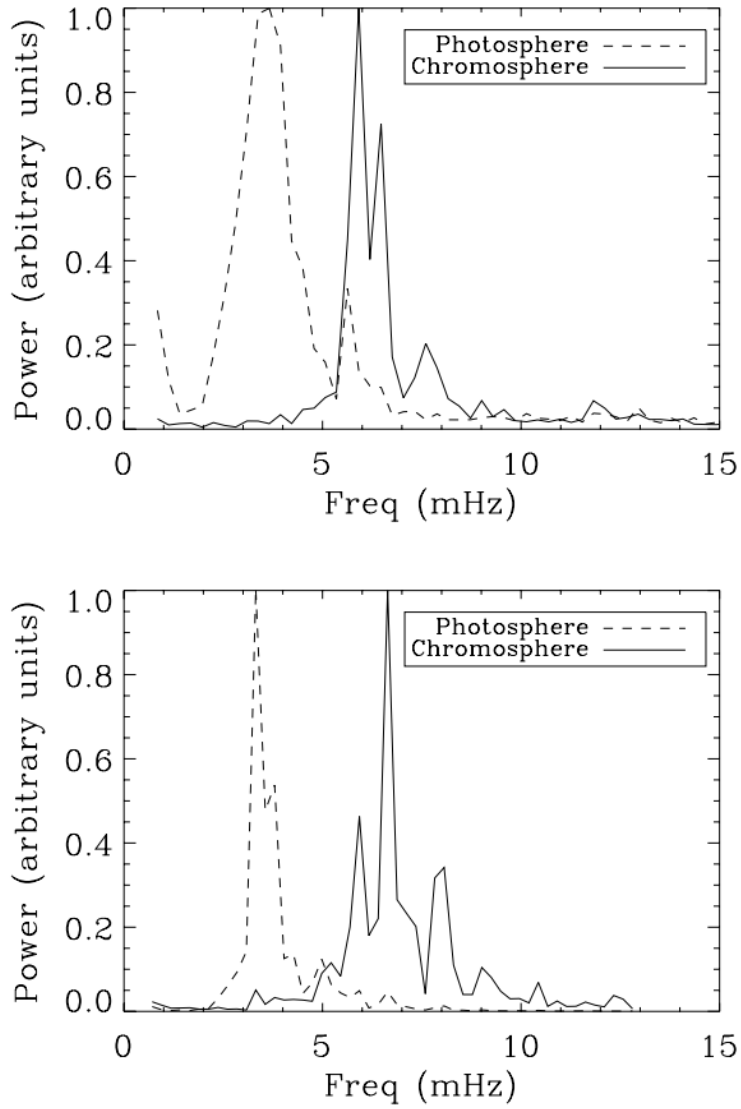
Figure 3.1: Normalised Fourier power from two different sunspots (top and bottom) measured from two spectral lines: the photospheric Si I λ10827 line (dashed line) and the chromospheric He I λ10830 multiplet (solid line). The Fourier power was calculated from a full Stokes inversion of line-of-sight velocity perturbations from both lines and averaged over their respective umbra. The difference in dominant frequencies between the two atmospheric heights is clear to see. Figure extracted from Centeno et al. (2006).

cause substantial variations in the frequency spectra taken from different areas of the solar atmosphere.

The solar atmosphere is of course, non-isothermal and hence equation (3.1) is in general not applicable. Various works have sought to derive an expression for the cut-off frequency in non-isothermal atmospheres (Deubner and Gough, 1984; Schmitz and Fleck, 1998; Musielak et al., 2006), however the choice of dependent and independent variables for the wave equations leads to a variety of different formulae (Schmitz and Fleck, 2003). The most widely used analytical form for a non-magnetic, vertically stratified atmosphere is

$$\omega_c = \frac{c}{2H} \left(1 - 2\frac{dH}{dz} \right)^{1/2},$$ (3.2)

as described in Roberts (2004).

Roberts (2006) went further in analysing the introduction of a vertical magnetic field in a stratified medium. For slow magneto-acoustic waves, which are predominantly the field aligned waves being produced in this study, the magneto-acoustic cut-off frequency is given by

$$\omega_c = c_t \left\{ \frac{1}{4H^2} \left(\frac{c_t}{c} \right)^4 - \frac{1}{2}\gamma g \frac{\partial}{\partial z} \left(\frac{c_t^2}{c^4} \right) + \frac{1}{a^2} \left(N^2 + \frac{g}{H}\frac{c_t^2}{c^2} \right) \right\}^{1/2},$$ (3.3)

where

$$c_t = \frac{ac}{\sqrt{c^2 + a^2}}$$ (3.4)

is the tube (cusp) speed,

$$N^2 = -g \left(\frac{g}{c^2} + \frac{1}{\rho}\frac{\partial \rho}{\partial z} \right)$$ (3.5)

is the square of the buoyancy (Brunt-Väisaälä) frequency, and

$$a = \frac{B}{(4\pi\rho)^{1/2}}$$ (3.6)

is the Alfvén velocity. Finally, all the aforementioned formulae don't take into account the effect of the inclination of the local magnetic field. The effect of the inclined magnetic field on the acoustic cut-off frequency was first demonstrated by Bel and Leroy (1977) and later by Jefferies et al. (2006). The greater the angle of the magnetic field from vertical, the lower the acoustic cut-off frequency, owing to the reduced gravity along the magnetic field. Thus, any choice of cut-off formula for ω_c taken from above must be moderated such that

$$\omega_m = \omega_c \cos\theta,$$ (3.7)

53

where θ is the angle of the magnetic field from vertical.

Several other alternative radiative processes have also been proposed which would further reduce the cut-off frequency (Roberts, 1983), however indications from numerical simulations by Heggland et al. (2011) suggest these effects to be negligible for low frequencies, such as those being discussed herein.

Most recently, (Felipe et al., 2018) analysed oscillations in the umbra of an active region sunspot at various heights to produce a profile for the cut-off frequency against height, which was then compared to the analytic formulae described by a variety of authors. The results suggested an agreement in the overall trend of the cut-off frequency profile and a good match in chromospheric values, whereas the photospheric values exposed significant quantitative differences. This could be due to the neglect of the magnetic field, such as in the models discussed above, or due to the use of the WKB approximation. This commonly used approximation produces a sharp spike in the profile of the cut-off frequency near the photosphere, which is inconsistent with the WKB formulation, as it assumes the linear acoustic waves being studied have wavelengths much shorter than the characteristic scales of the local atmosphere. This all implies care must be taken when interpreting values of the cut-off frequency from analytic formulae.

Whilst the various formulae used to describe the acoustic cut-off frequency can take many forms (Felipe et al., 2018), the general properties and their potential effects on MHD waves are found to be common and are easily extracted. Higher sound speeds (temperatures) result in a lower acoustic cut-off frequency and the deviation of the magnetic field from vertical also acts to decrease the acoustic cut-off frequency. This lowering of the cut-off frequency allows lower frequency waves to move unattenuated through parts of the solar atmosphere where they would normally become evanescent. In a typical sunspot atmosphere, these variations to the acoustic cut-off frequency manifest themselves most noticeably in two areas. Firstly, through the temperature minimum region in the lower chromosphere, which creates an extensive plateau of low cut-off values and ensures only the higher frequency waves survive this stage before growing to dominate the spectrum in the upper chromosphere. Secondly, the inclined nature of the sunspot magnetic field geometry further lowers the cut-off frequency. This effect is increased with radial distance from sunspot centre, where the magnetic field can bend up to $35°$ from vertical at the penumbra/umbra boundary (Jurčák, 2011). At a given height in the solar atmosphere, the increasing distance from sunspot centre therefore leads to overall lower frequencies being

measured (Maurya, 2013; Sych and Nakariakov, 2014), an effect seen clearly in Figure 3.2.
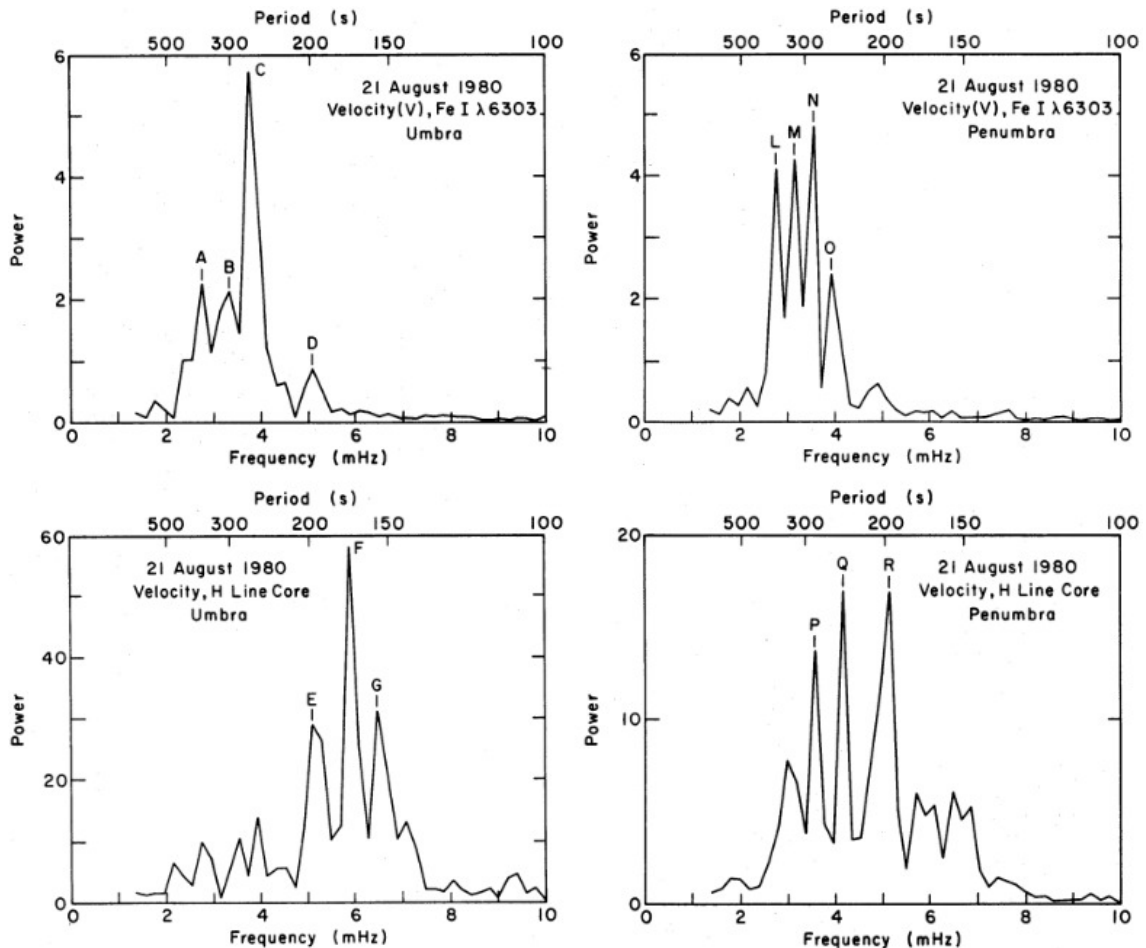

Figure 3.2: Averaged Fourier power derived from time series measurements of the photospheric Fe I λ6303 line (top row) and the chromospheric H line core (bottom row) for the umbra (left column) and penumbra (right column). The decrease in frequency from umbra to penumbra at a given height is readily apparent. The increase in power from photosphere to chromosphere due to the decreasing density profile with height can also be seen. Figures extracted from Thomas et al. (1984).

Further to this, some notably evanescent waves with frequencies below that of the local cut-off value can tunnel through and reach atmospheric heights which would otherwise not be accessible to them. This effect has been shown both numerically (Kráskiewicz, J. et al., 2019) and analytically (Cally, 2001). Somewhat predictably, the efficacy of this tunnelling is moderated by the distribution of the cut-off value with height. Tunnelling

is predicted and seen most dramatically through only narrow regions of increased cut-off frequency (Verwichte et al., 2006), such as the spike seen at the transition region in Figure 3.4. Most pertinent to this study, Fedun et al. (2011) presented 2D numerical modelling of magneto-acoustic waves in a model quiet Sun flux tube, where a range of frequencies were incited to show efficient tunnelling (leaking) of energy through the transition region and into the corona.

It is also prudent to note that solar frequency distributions observed over time, such as over the length of one or more solar cycles, have shown distinct variations (Jain et al., 2012; Elsworth et al., 2015; Santos et al., 2017). These are large time-scale observations and their effects are negligible for this discussion.

3.1.3 Sunspot Cavities

There are generally two competing theories describing the origin of the oscillations observed in the chromosphere. Studies such as Banerjee et al. (2002), Brynildsen et al. (2004), Centeno et al. (2006) and Afanasyev and Nakariakov (2015) suggest only upward propagating waves from the photosphere to the lower corona exist, whilst Gurman (1987) observed downward propagating waves by looking at line profiles of the Mg II k line. Further studies by Christopoulou et al. (2000) and Botha et al. (2011) propose the additional presence of standing acoustic waves which can leak into the corona. The idea of standing waves is supported by the possibility of partial reflections from any acoustic impedances within the atmosphere, characterised by any abrupt vertical change in the characteristic specific acoustic impedance $c_s\rho$ (Kinsler et al., 2000). These sharp density or sound speed (temperature) gradients can occur at the photosphere, the transition region and depending on the atmospheric model employed, other locations within the chromosphere. These reflection sites have the potential to create a chromospheric cavity with semi-permeable walls as proposed in Zhugzhda (2007, 2008). Any acoustic cavity will provide a location for trapped waves to resonate at their respective harmonic frequencies.

Each time these waves reach a site of potential reflection, there will be some transmission and reflection. The components which are transmitted through the transition region are observed as travelling waves in the corona, although it is still uncertain as to how high these waves can travel (Sych, 2016). In particular there is evidence that those waves can reach at least the heights of coronal reconnection sites, and modulate the flaring energy releases (Sych et al., 2009). Moreover, those waves could be responsible for the

quasi-periodic compressive perturbations detected at the heights about one solar radius above the solar surface (Ofman et al., 1997). Further to the transition region acting as an upper reflection site for any proposed cavity, it was found that the impact of the outgoing waves interacting with this region can excite horizontally propagating surface waves, as shown in 2D simulations by Fedun et al. (2011).

A recent study by Jess et al. (2019) provides strong observational evidence of a resonating cavity above an active region sunspot. Spectropolarimetric inversions taken from the centre of a large sunspot on 14 July 2016 were coupled with numerical simulations to further predict the temperature stratifications along the diameter of the sunspot, leading to a novel way of inferring the 3-dimensional structure of solar active regions.

3.1.4   Motivation for Study

The aim of this study is to identify the spatial extent of any resonant cavities caused by acoustic impedances in the chromosphere. The fundamental frequency of any cavity should show enhanced velocity signals in the component parallel to the magnetic field and exhibit characteristics of standing waves. The 1D umbral model of Botha et al. (2011) will be expanded to incorporate a full 2D potential magnetic field sunspot structure. The 1D results should be readily reproduced along the sunspot axis and further results owing to the introduction of a non-vertical magnetic field elucidated. The effect of the chromospheric temperature gradients as semi-permeable barriers causing partial reflections of slow magneto-acoustic waves can be demonstrated by looking at increased parallel velocity amplitudes in spectra taken from within the photospheric and chromospheric layers. Due to the importance of the cut-off effect, drivers with power both predominantly above and below the maximum cut-off values should be utilised.

3.2   Numerical Methodology

The computational modelling is conducted via 2-dimensional (2D) simulations of various model atmospheres and spectra of injected field-aligned (acoustic) magnetosonic waves. The numerical code used to solve the non-linear MHD equations is Lare2d (Arber et al., 2001). The computational domain is comprised of 256 x 256 grid cells, which is stretched in both the horizontal and vertical directions. The horizontal boundaries extend ± 15 Mm from the centre of the domain and the bottom and top boundaries are situated at -0.5 Mm

and 33.3 Mm, respectively. The grid stretching introduces variable grid spacing in both directions. The maximum horizontal grid spacing between ± 5 Mm is $\Delta x = 100$ km and the maximum vertical grid spacing between the bottom boundary and 2.5 Mm is $\Delta z = 25$ km; this being the particular area of interest. The vertical magnetic field strength is initially prescribed along the bottom boundary and given by

$$B_z = B_0 \exp\left(-\frac{x^2}{2\sigma^2}\right),\tag{3.8}$$

where $B_0 = 2$ kG is the peak amplitude of the field and $\sigma = 2.5 \times 10^6$ m. This initial distribution is used to generate a potential magnetic field throughout the rest of the domain as depicted in Figure 3.3.
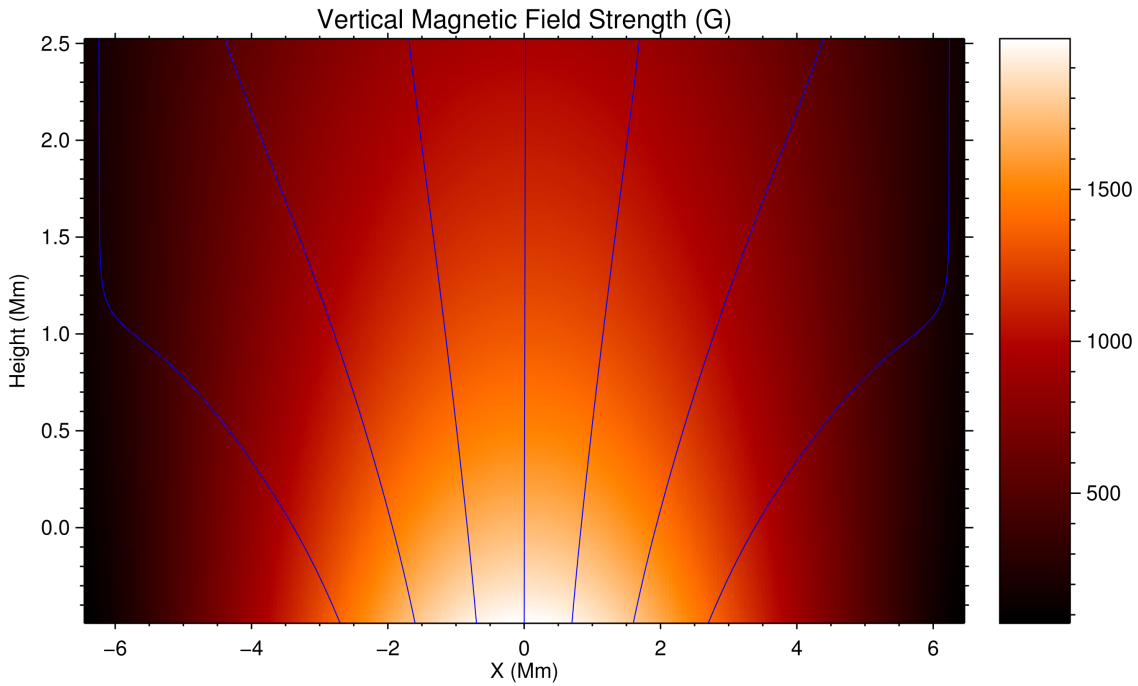

Figure 3.3: Vertical magnetic field distribution for the potential sunspot atmosphere with selected blue magnetic field lines superimposed.

The implementation of this particular model is supported by Schmelz et al. (1994), who showed that field strengths obtained from microwave observations in active regions are well reproduced by potential field extrapolations. The review by Borrero and Ichimoto (2011) also concludes that the magnetic field in the layers above the photosphere in sunspot umbrae is essentially potential in nature. The top and side boundaries of the domain

have closed/reflective conditions implemented - the derivatives of density, velocity and temperature are set to zero. In order to stop spurious reflections off these boundaries, a velocity damping profile based on the computational time step is implemented outside the area of interest. The magnetic field structure further acts to ensure no magnetic flux leaves through the side boundaries - here B_z is non-zero and $B_x \rightarrow 0$ to give a vertical field. The model peak photospheric magnetic field strength is set at $2\,\text{kG}$, which lies in the typical range for a smaller sunspot (Solanki, 2003).

The atmosphere is modelled by either an ideal, fully ionised gas, which ignores the inclusion of neutral hydrogen ions, or by a partially ionised gas; the particular atmosphere used for each result is clearly described herein. The reasoning behind not implementing the partially ionised gas for all simulations is multi-faceted. Firstly, the work of Botha et al. (2011) being compared to and extended in this study was conducted with a fully ionised gas. Secondly, there exist computational resource problems. Namely, the decreased density profile for the partially ionised atmosphere leads to a vast increase in the Alfvén speed and consequent decrease in the viable time step. The Lare2D code is a one-fluid MHD code, and as such, neutral-ion collisions would not be possible even in the partial ionisation implementation. Neutrals would, however, change the scale height, leading to an overall increase in the acoustic cut-off frequency as defined in equation (3.3). This is due to a change in the partial pressures and consequently the equation of state. Limited results are presented to show these assumptions to be valid in this particular case.

The temperature profile below the photosphere is prescribed by the polytrope

$$T = T_{ph} - \frac{b(\gamma - 1)zg}{\gamma}, \tag{3.9}$$

where $T_{ph} = 4040$ K is the photospheric temperature, $b = 2.0$, z is the distance below the photosphere, $\gamma = 5/3$ and g is the gravitational acceleration, set at a constant $274\,\text{ms}^{-2}$. The coronal temperature is given by the Avrett and Loeser (2008) model. As the area of interest lies between the photosphere and the transition region, different chromospheric temperature profiles are employed. Various models depict the distance between the photosphere and their respective transition region temperature gradients as being in the range of $1.0 - 2.8$ Mm in height (Staude, 1981; Lites and Skumanich, 1982; Avrett and Loeser, 2008; Fontenla et al., 2009). The main model being used in this work is based around the Maltby et al. (1986) Model M, which falls in the middle of this range with a transition region height of 2.1 Mm above the photosphere. In addition to this, an isothermal

chromospheric model is utilised and discussed in further detail later. In order to quantify the effects of the transition region temperature gradient as a reflecting barrier, simulations are performed with and without the inclusion of this region, depicted in Figure 3.4. Unless stated otherwise, all results pertain to the main model as described above.
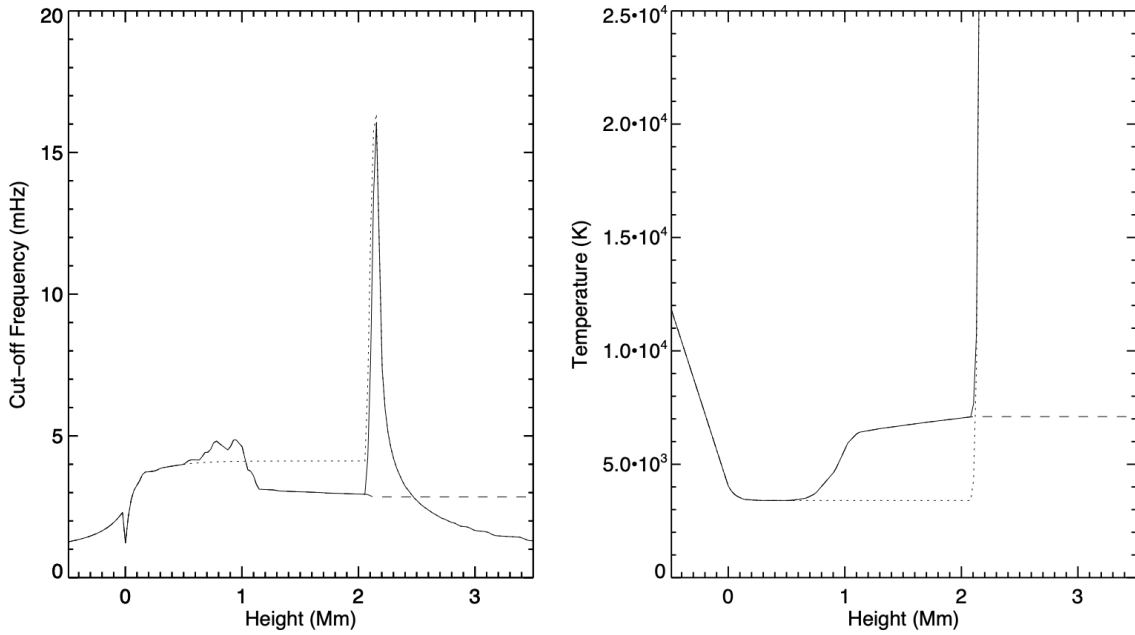

Figure 3.4: Three atmospheres were implemented: A modified Maltby Model M with (solid line) and without (dashed line) the transition region temperature gradient, and an isothermal chromospheric model (dotted line). Left-hand panel shows the cut-off frequency calculated from Equation (3.3) for each atmosphere and the right-hand panel gives their associated temperature distributions.

To drive the simulations, a frequency and space dependent Gaussian broadband source is implemented along the bottom boundary. The driver is a piston-like driver with 200 equally spaced frequencies in a given range (as described individually in section 3.3) and the perturbations are in v_z, the vertical velocity, given by

$$v_z = v_0 \exp\left(-\frac{x^2}{2\sigma_x^2}\right) \exp\left(-\frac{(\omega - \omega_0)^2}{2\sigma_\omega^2}\right), \qquad (3.10)$$

where v_0 is the amplitude of the source, $\sigma_x = 2.5 \times 10^6$ m, $\sigma_\omega = 1.0$ mHz, ω are the evenly spaced frequencies and ω_0 is the chosen peak frequency. The amplitude v_0, is chosen such that shocks do not develop, whilst the propagating waves still mimic the typical magnitudes of Doppler velocities measured at the solar surface (Thomas et al., 1997). As

the atmospheres have differing density profiles, this value will be adjusted dependent on the atmosphere chosen. In each case, the amplitude of the driver is slowly ramped up from zero to the full v_0 over the first 80 seconds of the simulation. After 3 hours of simulation time, the opposite happens, where the driver amplitude is slowly decreased over the same time period. The atmosphere is then allowed to oscillate/relax with no driver until a total simulation time of 6 hours is achieved.

For all of the drivers, the vertical velocities v_z are redistributed so they are parallel to the magnetic field on the bottom boundary such that

$$v'_z = v_z \cos \theta \tag{3.11}$$

$$v'_x = v_z \sin \theta, \tag{3.12}$$

where θ is the angle between the magnetic field vector and vertical, and v'_z and v'_x are the new vertical and horizontal velocities being imparted. As the driver is applied only along the magnetic field on the lower boundary, there should be no direct input of Alfvén or kink waves. The Alfvén acoustic equipartition layer z_{eq} (discussed extensively in the introduction to Chapter 2) lies near the level of the photosphere in this particular model. The close proximity of this layer to the bottom driving boundary ensures that the attack angle (the angle between the wave vector and the magnetic field) remains small. A small attack angle results in almost near complete transmission from fast-slow. The waves retain their acoustic characteristics and propagate almost entirely along the field lines. This is supported by numerical results, which show that the velocities in the upper chromosphere have negligible amplitudes in their components transverse to the magnetic field. High in the chromosphere, the plasma beta level will have decreased significantly to the point where field aligned and non-aligned velocities can give a good representation of the degree of fast/slow (magnetic/acoustic) waves present in the atmosphere. This also negates the need to examine the effects of fast wave reflection and fast-Alfvén conversion, both of which occur in the area where the fast wave's horizontal phase speed equals the Alfvén speed (Cally and Khomenko, 2018), usually located within the chromosphere. Hence, the following analysis is now concentrated purely on the component of the velocities parallel to the magnetic field.

A selection of the simulations described above were run with a 512 x 512 cell domain and no appreciable differences were found in any of them, suggesting the results have converged.

3.3 Results and Discussion

The results from the study below are separated into various sections dependent upon the drivers and atmosphere being implemented. For all simulations, field aligned magneto-acoustic waves are imparted into the domain via a bottom boundary driver which runs for the first 3 hours in each 6 hour simulation, before having its amplitude reduced to zero. The driven waves propagate upwards, guided by the magnetic field lines and are simultaneously filtered by the magneto-acoustic cut-off frequency effect. This causes a preferential attenuation of waves with frequencies below that of the local maximum cut-off frequency. As discussed through the introduction of this chapter, there are various forms used to describe the cut-off frequency. To best represent the effect of the inclined magnetic field within the sunspot model, a simplified version of the cut-off frequency can be visualised

$$\omega_c = \frac{c}{2H} \cos\theta, \tag{3.13}$$

where c is the local sound speed, $H = c^2/(\gamma g)$, $\gamma = 5/3$ is the ratio of specific heats, g is the gravitational acceleration, z is the height and θ is the inclination of the magnetic field from vertical. Due to the change in sound speed with height and the inclined structure of the magnetic field, this cut-off frequency varies throughout the chromosphere and an example from the main model atmosphere is given in Figure 3.5. This gives a good depiction of how the magnetic field will act to decrease the cut-off frequency along inclined fields found within sunspot umbrae. Further modifications to this formula will be implemented in the appropriate sections to give a more detailed description.

From the Fourier velocity spectra of the various simulations, it can be determined how this cut-off frequency has affected waves as they travelled along their respective field lines. Frequencies above the cut-off frequency will survive the evanescent stage of minimum temperature (equivalently maximum cut-off frequency) before continuing to grow in amplitude as they travel higher into the increasingly less dense atmosphere, and Figures 3.6 & 3.7 show clearly these effects playing out. As the waves travel along more inclined fields further away from sunspot centre, more and more lower frequencies (present in the original driver) are able to freely propagate into the upper chromosphere. This effect is visible when using the driver centered around 3.3 mHz, a frequency well below the maximum cut-off frequency. The frequency distributions at greater distances from sunspot centre begin to resemble that of the driver itself, suggesting little filtering is occurring at
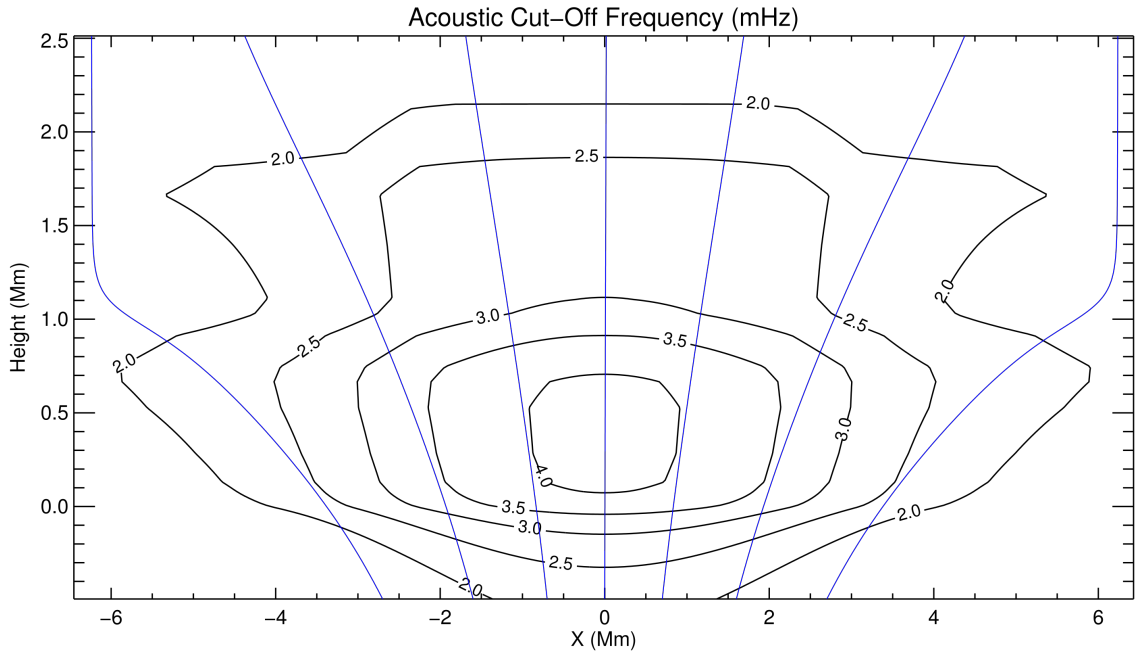
Figure 3.5: Contour plot of the simplified acoustic cut-off frequency (mHz) (see equation 3.13) using an ideal gas from the region of interest with transition region height set at 2.1Mm. Select magnetic field lines have been superimposed in blue. Above the transition region, the cut-off frequency falls off sharply.

these widths. The dominant frequencies along the sunspot axis in the upper chromosphere are shifted to a minimum of 4.1 mHz. This demonstrates that it is possible to achieve a velocity spectrum in the upper chromosphere containing dominant frequencies that are comparatively only weakly represented in the initial driving source.

If there is a transition region temperature gradient imposed, the outgoing waves will be partially reflected upon interaction with it. Although it can not be seen through any plots, it is also apparent that upon impact with this gradient, travelling surface waves are created, which propagate horizontally along the length of the computational box. This effect was previously documented in numerical simulations of magneto-acoustic waves in localised flux tubes by Fedun et al. (2011). These velocities transverse to the field are found to remain negligible in amplitude when compared to the field aligned velocities. In this case, the principal interest lies in the vertically reflected waves as they begin to set up potential resonant cavities within the chromosphere.
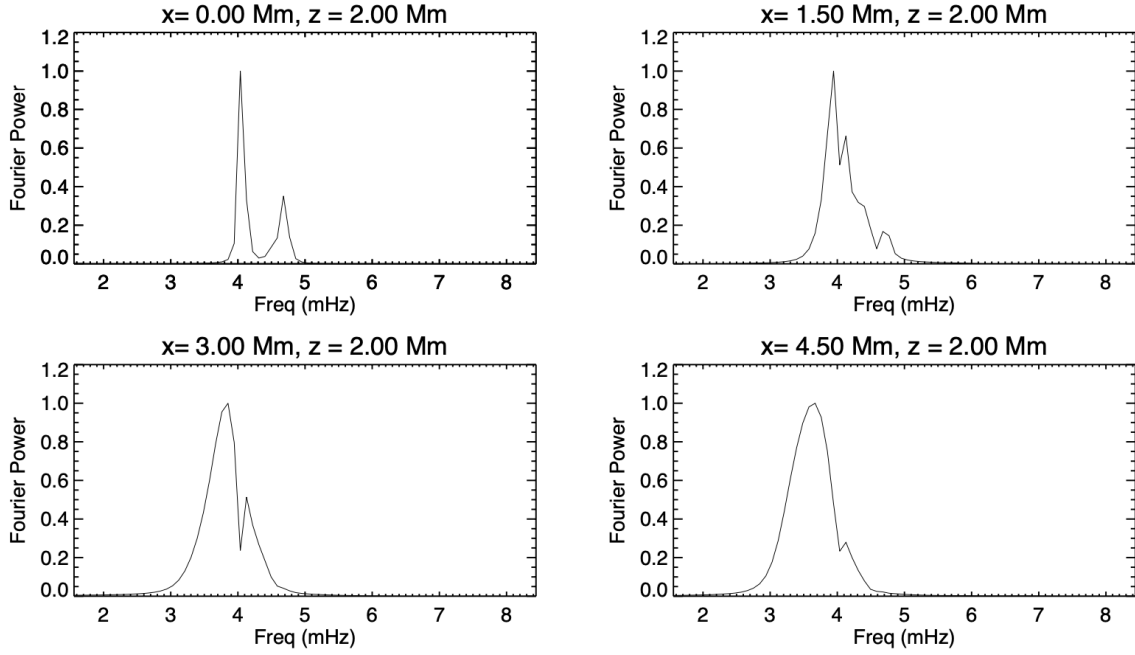
Figure 3.6: Normalised Fourier Power spectra taken from parallel velocity measurements with $\omega_0 = 3.3$ mHz. All spectra were recorded at the widths and heights given above each panel. The height of 2.0 Mm corresponds to a height just below the transition region. At a distance of 4.5 Mm, the frequency distribution begins to resemble that of the driving source.

3.3.1 Cavity Extent and Resonant Frequency

It is readily apparent that the transition region temperature gradient acts as the upper reflecting point of any proposed chromospheric cavity. Although, it should be noted that due to the amplitudes of the incoming waves, the transition region oscillates and can vary in height by up to 0.1 Mm either side of its original position, so it should not be considered a permanent hard boundary. What is less obvious is the site of the lower reflection point, something obviously needed to create a closed cavity. Of course there is already a well known p-mode cavity - any waves reflecting back through the photosphere will be trapped in this cavity as they are eventually totally internally reflected back due to the ever increasing sound speed of the solar interior. This occurs at a depth roughly given by

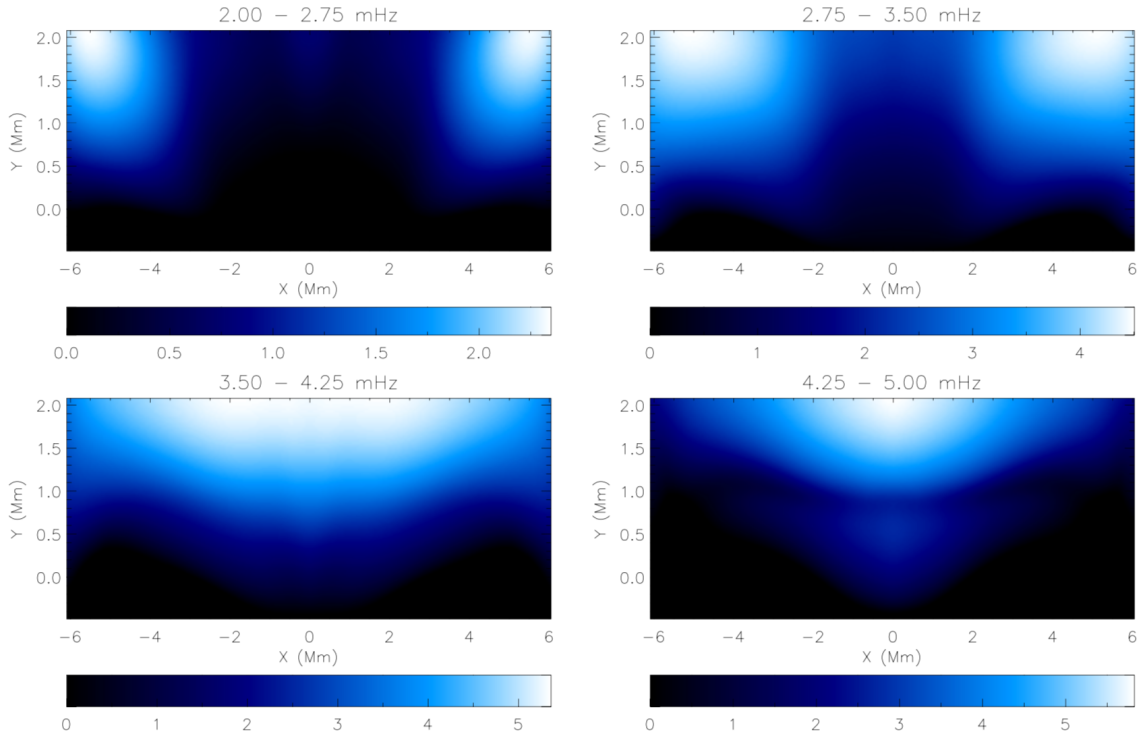$$ z = \frac{\omega^2}{\gamma - 1} \, g \, k_h^2, \tag{3.14} $$

Figure 3.7: Log plots of parallel Fourier velocity (m/s) for the frequency bins defined respectively above each panel. The top boundary of each panel corresponds to the height of the transition region temperature gradient at $z = 2.1$Mm. The driving frequency is centered around $\omega_0 = 3.3$ mHz.

where k_h is the horizontal wavenumber (Foukal, 2004). It follows that the low frequency waves being imparted here reflect at depths well below the photosphere and hence are clearly outside the computational domain used here. By looking more locally, there are distinct temperature gradients both at the photosphere and within the chromosphere. These gradients can also produce peaks in the cut-off frequency distribution (see Figure 3.4) and can act as potential reflecting sites. From the limited studies done on this topic, both of these gradients have been proposed as possible reflection sites. Botha et al. (2011) conducted 1-dimensional numerical simulations in a collection of more simplified atmospheres than that used here and proposed the photosphere as the lower extent of the cavity. Little explanation or results are given to justify this conclusion past the notion that there is a temperature gradient present at that particular height. More recently, a 1-dimensional numerical study with constant magnetic field strengths was conducted by Felipe (2019), where height of the transition region was varied, resulting in an increase in Fourier power in

the upper chromosphere for different period waves. It is interesting to note that Snow et al. (2015) found that the distance below the chromospheric temperature gradients influences the Fourier power more than the distance above, although it is unclear as to why this is. The periods identified by Felipe (2019) were used to extrapolate the distance of the wavelength of the first harmonic via the equation

$$P_r \approx \frac{2L}{\bar{v}_c n}, \tag{3.15}$$

where L is the length of the cavity, $\bar{v}_c$ is the average sound speed and $n = 1$ for the first harmonic (Freij et al., 2016). A worthwhile comparison can be drawn along the central axis of the 2-dimensional simulations presented herein. To identify the resonating frequency (period), the reader is referred to Figure 3.8. Here, two different driver frequencies were used to drive the simulations, one below the maximum chromospheric cut-off frequency and one above (the cut-off frequency distribution can be viewed in the left-hand panel of Figure 3.4). The top panel shows the frequency spectrum of both the 3.3mHz and 6.7mHz drivers being implemented along the bottom boundary. The extra peaks lying outside the predicted Gaussian distributions are thought to be due to partial reflections off the photospheric temperature gradient. The middle panel shows that after progressing through the chromosphere to a height of 0.8 Mm, peaks at distinct frequencies become apparent. The waves with frequencies below the local acoustic cut-off frequency produced by the 3.3mHz driver have been filtered out and the lowest surviving frequencies (these contain the most power from the original driver) grow to dominate the spectrum at just over 4.0 mHz. The waves produced by the 6.7 mHz driver are unaffected by the comparatively small cut-off values and propagate freely to dominate the spectrum. Moving higher into the chromosphere to a height of 1.8 Mm, the lower panel now shows a clear frequency peak of 4.7 mHz present in both spectra that was absent at lower heights. It is proposed that this is the resonant cavity frequency for the given chromosphere. By utilising a similar approach to that of Felipe (2019) - the actual sound speed at each point is used instead of the average - a cavity length of ~ 1.1 Mm is found. Subtracting this value off the height of the transition region would place the lower reflection site at ~ 1.0 Mm, which aligns co-spatially with the peaks in the chromospheric cut-off frequency distribution as can be seen in the left-hand panel of Figure 3.4.

To bolster this idea, further results can be drawn upon. Firstly, by utilising a completely flat temperature profile in the chromosphere (see right-hand panel of Figure 3.4 for this profile), what can be expected is travelling (and reflected) waves both at a frequency just
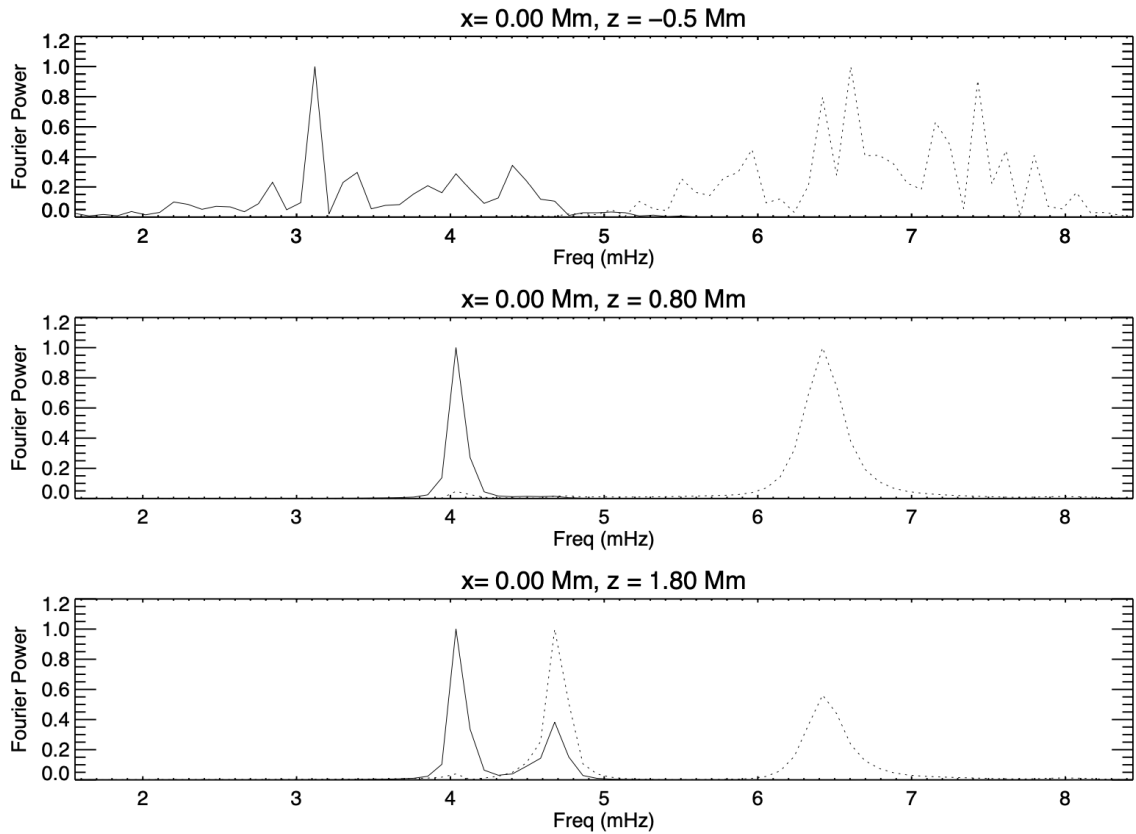
Figure 3.8: Normalised Fourier power spectra measured along the sunspot axis for $\omega_0 = 3.3$ mHz (solid line) and 6.7 mHz (dotted line) at the heights z given above each panel. The top panel coincides with the bottom boundary and represents the spectrum of the driving sources. The middle panel shows the frequency peaks outside of the cavity in the middle chromosphere. The bottom panel is at a height within the chromospheric cavity and highlights the extra resonant cavity frequency peak at ~ 4.7 mHz not seen in the middle panel.

67

above that of the local cut-off frequency will dominate the spectrum, and indeed this is what is found. The comparison of frequency spectra with a flat chromospheric temperature profile compared to the original atmosphere is displayed in Figure 3.9. This suggests that the extra temperature gradient within the chromosphere is cause for the production of the resonating frequency at 4.7 mHz. Of course there now exists the potential for a cavity being created by a lower reflection point at the photospheric temperature gradient. This is unremarkable as it would have a resonating frequency well below the local cut-off frequencies experienced within the chromosphere and will be absent from the spectrum.
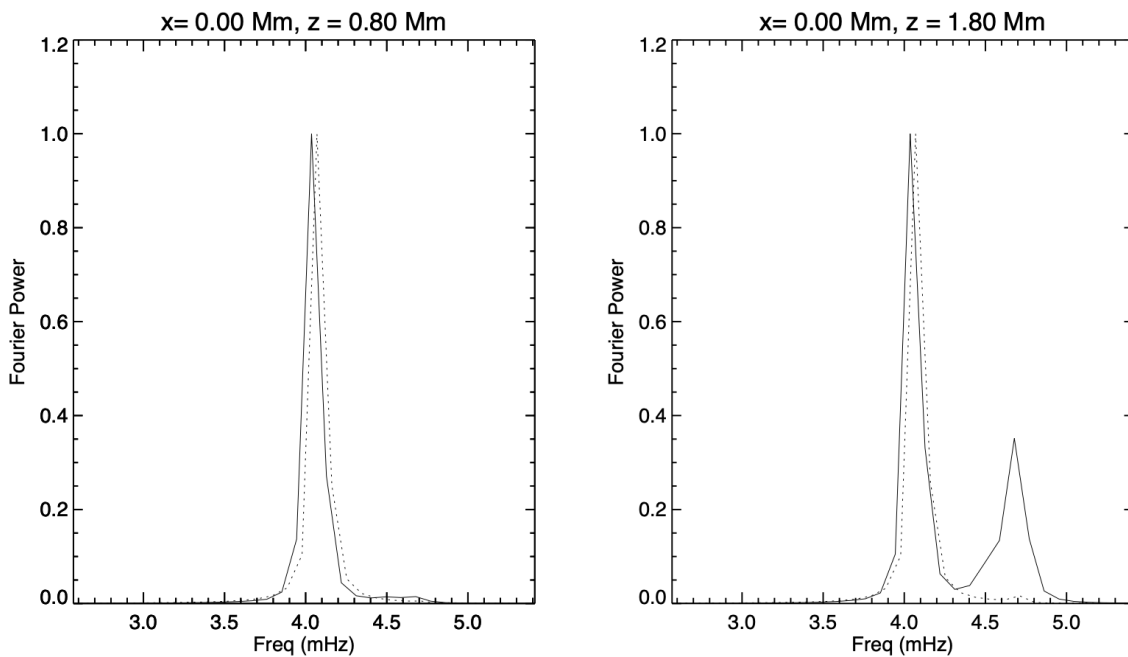

Figure 3.9: Normalised Fourier power spectra for the main model atmosphere (solid line) and the isothermal chromosphere model (dotted line). The extra temperature gradient in the Maltby model produces a further resonant frequency. The small shift in the dominant peak can be associated with the variation in cut-off frequency between the two models.

In addition to this, a more direct approach to identify the spatial extent of any cavity within the chromosphere is to make comparisons of velocity amplitudes between the atmosphere with and without a transition region temperature gradient (see right-hand panel of Figure 3.4 for these profiles). These measurements are established by taking the Fast Fourier Transform (FFT) of the parallel velocity time series over the duration of the entire simulation. The recorded Fourier velocities are summed together for the proposed resonant cavity frequency range ($4.4 - 5.0$ mHz) and compared between the simulations with and

without the transition region. As is seen in Figure 3.10, the outgoing waves reflect off the atmosphere with the transition region and produce a substantial increase in Fourier velocity in the upper chromosphere of up to $\sim 140\%$ (over a 400% increase in Fourier power) when compared to the atmosphere without a transition region. This increase in velocity is seen to extend down to a height which is in good agreement with the proposed lower reflection site of ~ 1.0 Mm. The increase is most apparent along the sunspot axis and within 3 Mm either side horizontally.
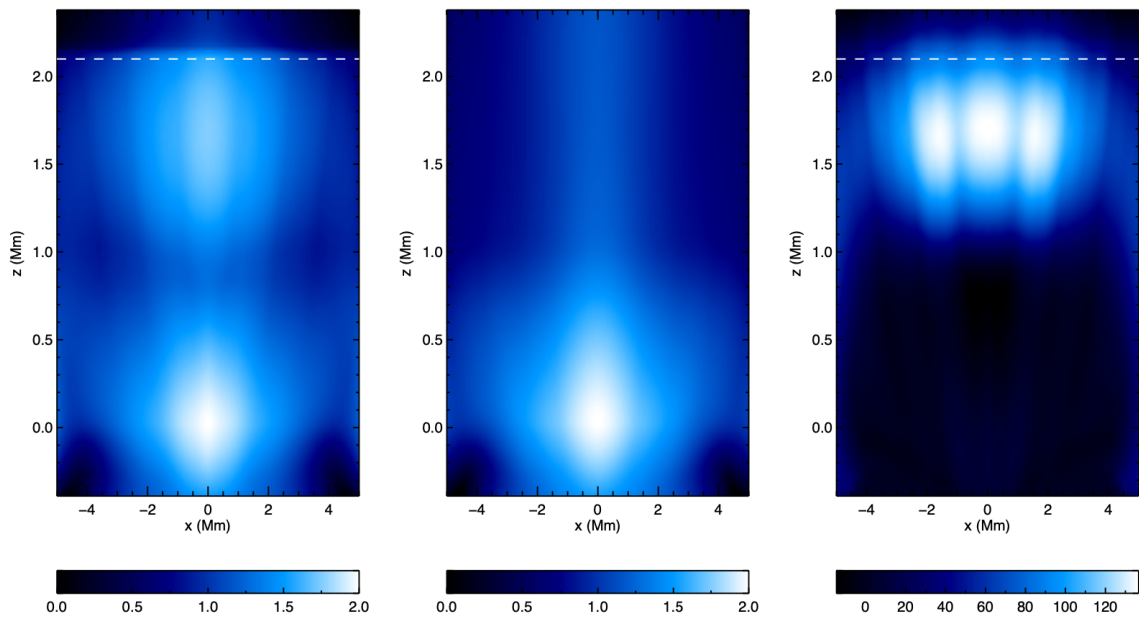

Figure 3.10: Log plots of parallel Fourier velocities summed over the proposed resonating frequency range $(4.4 - 5.0$ mHz$)$ scaled by $\sqrt{\rho c}$ for the main model with (left-hand panel) and without (middle panel) transition region temperature gradient. The right-hand panel is then a direct percentage increase comparison between the two, helping to elucidate the spatial extent of the resonating chromospheric cavity.

3.3.2 Driver Frequency

Two different broadband drivers were implemented, centred around $\omega_0 = 3.3$ and 6.7 mHz with a common standard deviation of $\sigma_\omega = 1.0$ mHz. For each case, the driver is 200 equally spaced frequencies from 0.5 - 10.0 mHz (for the 3.3 mHz driver) and 0.5 - 20.0 mHz (for the 6.7 mHz driver). These frequencies were chosen such as to represent ranges

that are both predominantly lower and higher than the maximum cut-off frequency in the chromosphere.

Time series for the parallel velocities recorded at probe points situated along the sunspot axis at certain heights for both frequency drivers are shown in Figures 3.11 and 3.12. The heights of the probe points were chosen to encompass areas both inside (1.6 and 2.0 Mm) and outside (0.8 Mm) the proposed cavity. All velocities have been normalised to the maximum velocity recorded at any of the probe points from each respective simulation. To begin with, all velocity perturbations are clearly out of phase in both simulations and must represent the initial travelling wave. Not long after, the perturbations measured inside the cavity (1.6 and 2.0Mm) move to being in phase, suggesting a standing wave is present in this area. This effect is seen most strongly when using the 3.3 mHz driver, as the oscillations from within the cavity for the 6.7 mHz driver look to contain various amounts of both the travelling and standing waves. From this observation, it becomes clear that higher frequency components are more capable of tunnelling through the acoustic cut-off spike at the transition region, a feature also noted in Santamaria et al. (2015).

For both simulations, the perturbations outside the proposed cavity (0.8 Mm) remain out of phase with those inside the cavity at all time, suggesting the cavity does not extend to this height. This area outside the cavity is dominated by travelling waves produced by the bottom boundary driver. After the driver amplitude is reduced to zero in the short time following 180 minutes, the cavity continues to resonate with the waves trapped within. Although these waves are constantly being leaked out, as can be seen by the decrease in velocity over time. The oscillations measured in the resonant cavity for the 6.7 mHz driver decrease in amplitude much quicker than those of the 3.3 mHz driver, giving further credence to the theory that the higher frequency components are more easily able to penetrate the boundaries of the cavity and hence leak out to a greater degree.

Figure 3.13 depicts the same scenario described above with the 3.3 mHz driver, however there is an absence of transition region temperature gradient. It is clear that in this case, all measured perturbations remain out of phase and represent travelling waves, as expected. No standing waves are recorded and the cavity ceases to exist.

3.3.3 Partial Ionisation

A partially ionised gas is now implemented for the modified Maltby Model M atmosphere. When introducing partial ionisation, the change in density required to achieve hydrostatic
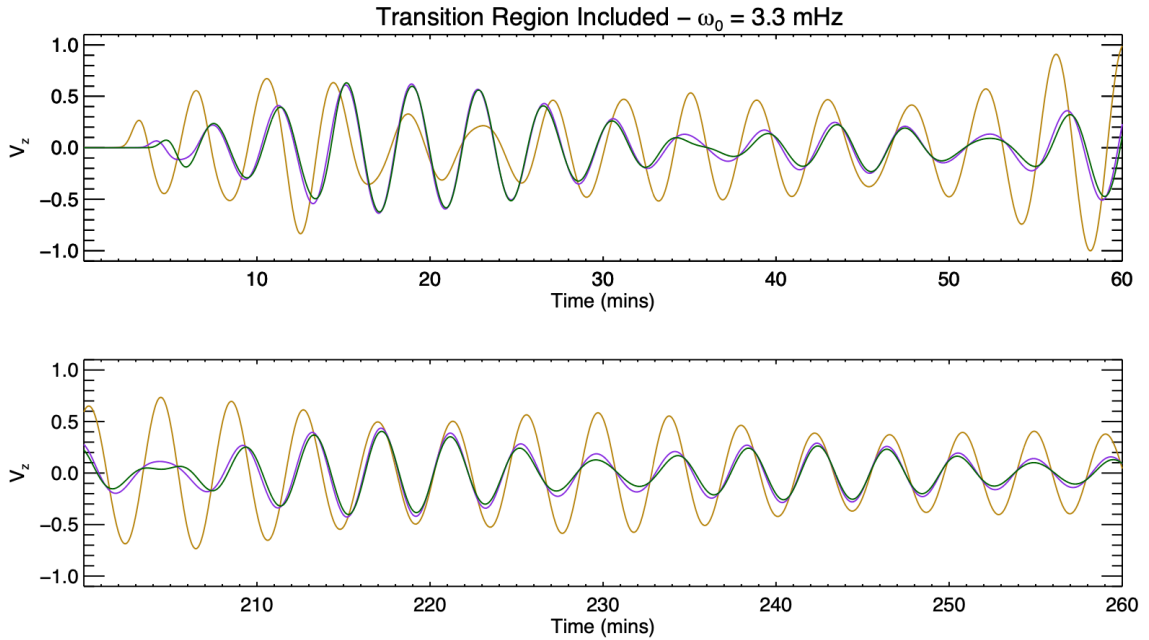
Figure 3.11: Selected time series of the normalised vertical velocity perturbations along the sunspot axis at various heights for driving frequency $\omega_0 = 3.3$ mHz. The gold line represents a point outside the proposed cavity ($z = 0.8$ Mm), whilst the purple ($z = 1.6$ Mm) and green lines ($z = 2.0$) Mm are from within the cavity. The top panel shows the first hour of simulation time. Here, all perturbations begin out of phase, which represents the initial travelling waves being driven from the bottom boundary. It is less than 10 minutes before the perturbations from within the cavity move to being in phase and represent a standing wave, whilst the perturbations outside the cavity remain predominantly out of phase and constitute a travelling wave. The bottom panel shows a further hour of simulation time not long after the amplitude of the driving source has been reduced to zero.

equilibrium results in an overall decreased scale height. This change leads to an increase in the cut-off frequency in the chromosphere by approximately 1 mHz. This effect is visualised in Fourier power spectra shown in the top panels of Figure 3.14. The driver implemented is centered around $\omega_0 = 3.3$mHz, whilst the amplitude of the source was decreased compared to those used in the ideal gas atmosphere so as to again prevent developing shocks or other non-linear effects. As the waves propagate upwards, all frequencies below 5.2mHz are filtered out along the sunspot axis. Much like in the lower chromosphere for the ideal case, it is then the lowest surviving frequency which begins to dominate the spectrum. The difference in this case being that the resonant cavity frequency of 4.7 mHz has also been filtered out, as is to be expected due to the higher maximum
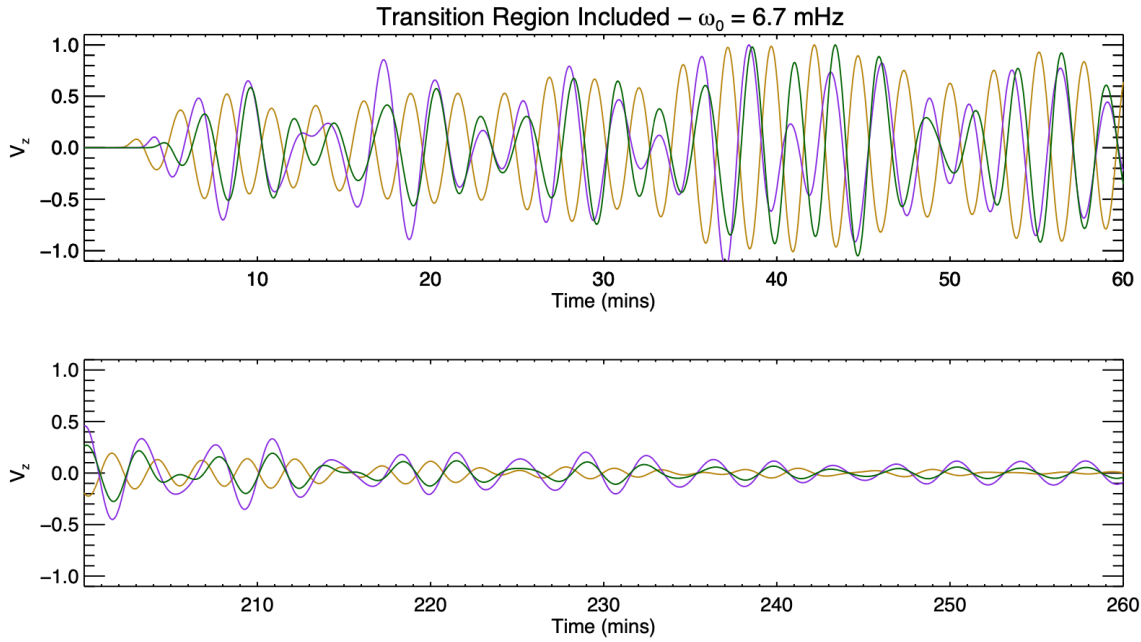
Figure 3.12: Same as Figure 3.11 with driving frequency $\omega_0 = 6.7$ mHz. The presence of the standing wave is not as clear as with the lower frequency driver, suggesting a combination of both standing and travelling waves. The amplitudes of the perturbations after the driving has stopped (bottom panel) decrease much quicker than for the lower frequency driver.

cut-off frequency. However, as the distance from sunspot centre is increased (bottom panels), the increased inclination of the local magnetic field causes the cut-off frequency to drop off as described by equations (3.3) & (3.7). This allows the cavity frequency to survive this evanescent stage and eventually dominate the spectrum. This further supports the idea that the resonant cavity frequency need not be strongly represented in the driving spectrum but it must survive the effect of the cut-off frequency before reaching the cavity. Note, the spectra shown have been taken from a reduced simulation time of 1.5 hours due to computational limitations, however the aforementioned results are clear to see.

3.4 Conclusion

Field aligned magneto-acoustic waves of frequencies both predominantly above and below the maximum cut-off frequency have been injected into a potential magnetic field sunspot atmosphere with a chromospheric temperature distribution reflecting that of a
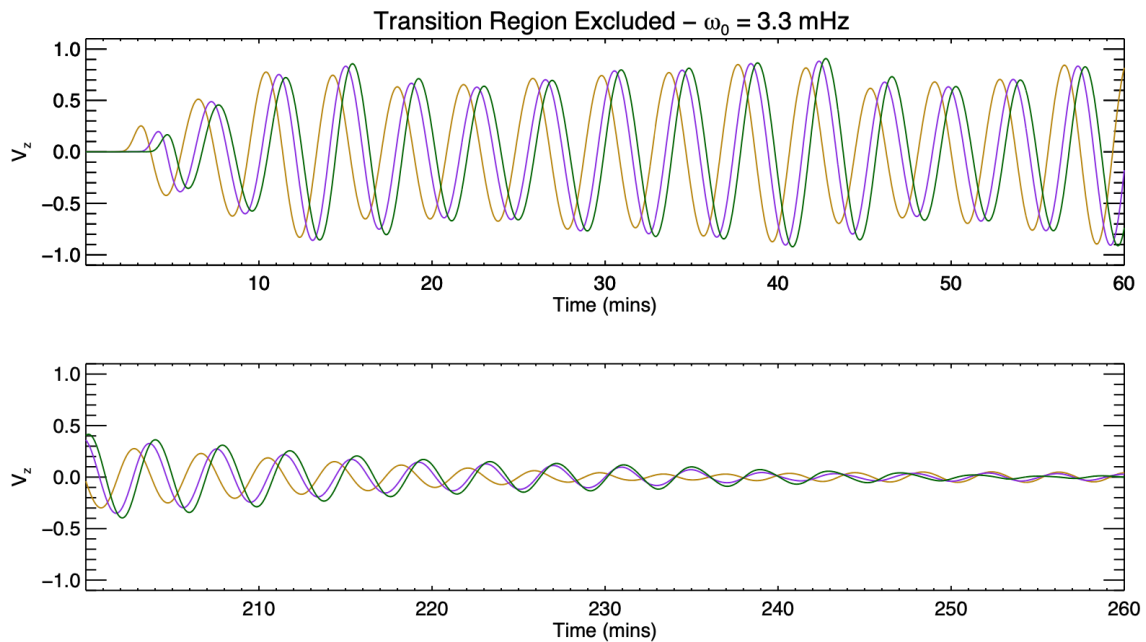
Figure 3.13: Same as Figure 3.11 with the transition region removed. A travelling wave is observed at all heights measured throughout the chromosphere for all time.

well referenced model. Through parallel velocity measurements, it is seen that a resonant cavity is formed in the upper chromosphere. The bounds of the cavity are described by the temperature gradients both at the transition region and within the chromosphere itself. A resonant frequency of ~ 4.7 mHz is found to exist in spectra taken from within the cavity but is absent outside the cavity. This frequency is also absent from the spectra when the chromospheric temperature gradients are removed. A standing wave is formed within the cavity, whereas travelling waves are recorded outside the cavity. The cavity's resonant frequency must be present in the original driving source, though the power in this particular frequency need not be initially strongly represented. The potential resonant frequency waves must also survive the effect of the local cut-off frequency as they propagate through the temperature minimum (maximum cut-off) region of the chromosphere. The velocity amplitudes of the resonant frequency increase by well over 100% for the linear regime in the upper chromosphere compared to when there is no cavity present. After the driving amplitude is reduced to zero, the waves trapped in the cavity begin to leak into the surrounding atmosphere and hence the cavity acts as a leaky resonator.
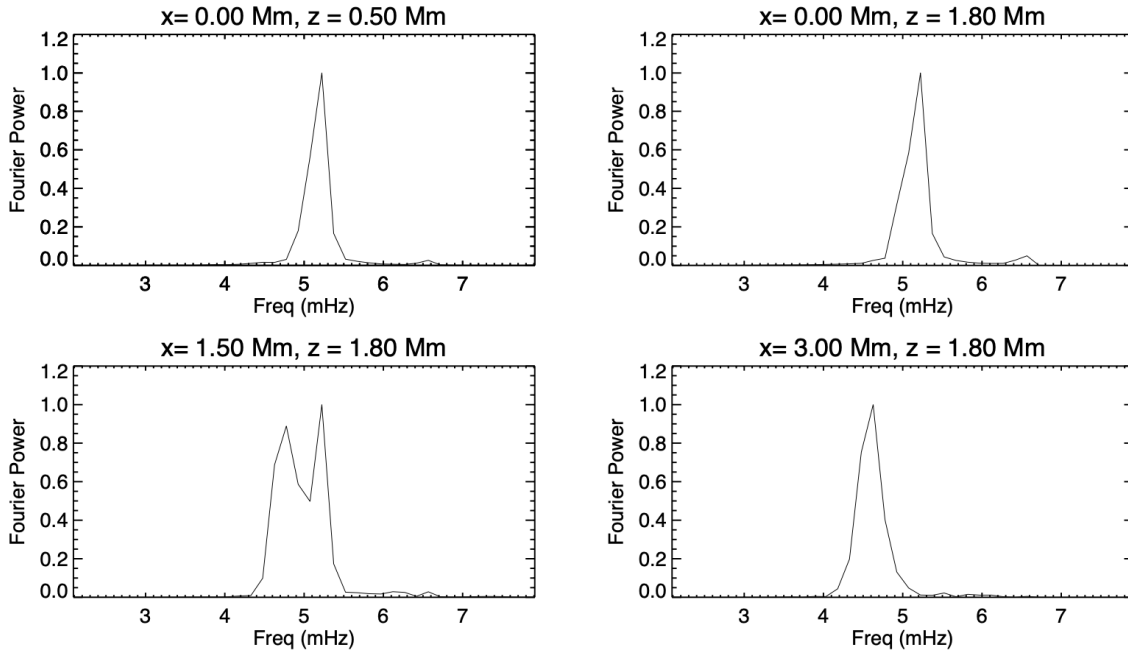
Figure 3.14: Normalised Fourier power spectra for the partially ionised atmosphere with transition region temperature gradient present recorded from a simulation spanning 1.5 hours. Top panels: Frequencies below the local cut-off frequency become evanescent, the lowest surviving frequency then begins to dominate the spectra. The resonating frequency of ~ 4.7 mHz does not survive this process and is lost. Bottom panels: Moving away from sunspot centre allows lower frequency waves to propagate freely, including that of the resonant frequency. This frequency then begins to dominate the spectra at increasingly larger horizontal distances.

3.5 Implications and Further Research

Strong magnetic fields, such as those found in active region sunspots play a fundamental role in the dynamical processes in the solar atmosphere. Magnetic structures can act as a wave-guide for magneto-acoustic waves, providing a link between the solar convection zone and photosphere through the transition region and in to the solar corona. This process is predicted to be the main energy supply for the outer solar atmosphere and understanding this process is crucial in solving the coronal heating problem (De Pontieu et al., 2004, 2005). Measurements of Doppler velocities only become tenable above the solar photosphere and are commonly taken from within the chromosphere to infer the degree of energy being transported into the corona. This study suggests that Doppler velocities measured from within the upper chromosphere cannot be attributed solely to outwardly propagating waves.

The existence of resonating chromospheric cavities must be taken into account as there can exist a stark increase in the resonant frequency amplitudes, impacting on any inferences drawn from them, most likely in terms of energy transport.

The following simulation parameters have either been ignored, or can be improved/expanded upon:

- Partial Ionisation: The main atmosphere used in this study was modelled as a fully ionised gas, yet the ionisation fraction at the photosphere can be as low as 10^{-4} (Vernazza et al., 1981). The reasons behind not including partial ionisation have been discussed previously in detail.

- Sunspot Model: A potential sunspot atmosphere has been utilised, and whilst this implementation is supported in the solar literature for the chosen atmospheric model, it eliminates the possibility of modelling sub-photospheric layers. In turn, this model does not support the implementation of deeper drivers, such as those stemming from the convection zone. In order to retain the sunspot structure, a non-potential sunspot model such as in Przybylski et al. (2015), which is an optimised version of the model developed by Khomenko and Collados (2008) could be implemented, allowing more realistic deeper sources to be used.

- Chromospheric models: A variety of different chromospheric temperature profiles have been proposed from the myriad of observational data available. As the cavity extent and its associated resonant frequency is dependent on this temperature distribution, more models could be introduced for testing.

- Kink/Alfvén Waves: Non-field aligned waves can be injected into the atmosphere to study how the effect of slow-fast and fast-Alfvén conversion plays a role in the increased amplitudes measured in the chromospheric cavities. Fast wave reflection within the chromosphere would also begin to play a role.

- Non-linear Effects: Magneto-acoustic waves have been reported to develop into shocks in the mid-chromosphere (Vecchio et al., 2008). If these shocks develop in the lower chromosphere, they are also known to split into their fast-slow components, with the slow shock being smoothed through the equipartition layer as discussed extensively in Chapter 2. The driving amplitudes chosen in this study were sufficiently

low so that non-linear effects aren't experienced to any appreciable degree and are hence ignored.

- Radiation: The numerical code used assumes an infinite radiative cooling time, yet there has been convincing evidence for decades that temperature fluctuations are moderated by radiative smoothing, an effect incorporated in the literature of various problems involving stellar atmospheres as far back as Vitense (1953). The need to include radiative effects will become more prominent with non field-aligned velocities, increased amplitudes and the introduction of partial ionisation (Khomenko, 2015).

Anisotropies of Solar Quakes

4.1   Introduction

The study of the interior of the Sun through observations of the solar surface is nothing new in the realm of solar physics - a process known well as helioseismology. The constant turbulence due to convective motions within the Sun sees the production of innumerable pressure waves (p-waves). These waves propagate through and interact with the various physical components of the solar interior. In doing so, they obtain information regarding the composition and dynamics of the medium they have passed through, which can be readily extracted through various observational techniques. The advent of helioseismology has led to a host of improvements in solar models with calculations of the convection zone depth (Christensen-Dalsgaard et al., 1991; Basu and Antia, 1997), rotation rates (Brown and Morrow, 1987; García et al., 2007), elemental abundances (Vorontsov et al., 1991; Richard et al., 1998), sound speed and density structures (Antia and Basu, 1994) becoming much more accurate, as well as providing a fundamental role in resolving the solar neutrino problem (Fukuda et al., 1999; McDonald et al., 2002). Similar helioseismic techniques can further be employed to investigate relatively newly discovered phenomena known as solar quakes.

Strong pressure waves are also generated by solar quakes, a direct energetic consequence of solar flare production. During their impulsive phases, solar flares can, under specific conditions deposit energy back into the Sun via spatially confined, high energy impacts with the solar photosphere. The dynamics of solar flare generation and the mechanisms involved is an area of active study and much is still unknown. It is proposed that the

study of solar quakes can act as a tool to uncover more information regarding the dynamics of the initial (impulsive) stages of solar flare production. Their highly localised and intense nature, along with their location around sunspots can also act to provide more detailed local analysis of magnetically active regions than global helioseismology could produce.

Despite the continual accruing of observational data, the physics behind the generation of solar quakes, or seismic transients, is poorly understood and many theories have been proposed to date. What is clear is that following the onset of some solar flares, only a hundredth or even a thousandth of the flare's energy is deposited back into the solar interior. This is still a significant amount of energy, which causes a collection of pressure waves to be sent into the solar interior. These waves will eventually return to the surface due to the ever increasing sound speeds they encounter. The edge of the wave front closer to the centre of the Sun will travel faster than that of the outer edge, causing it to bend back to the surface. The returning pressure waves cause disturbances at the photospheric level, which are the signatures of a solar quake. They consequently appear as a set of concentric ripples emanating from the initial impacting site (see Figure 4.1). The various magnetic field configurations found within active solar regions can act to alter the traditional acoustic properties and trajectories of any travelling wave in this environment. Therefore, understanding the physical parameters specific to such environments and their individual effects on flare-generated waves throughout their journey into the solar interior becomes important. It is these subsurface effects which act upon the waves before they return to the surface and manifest themselves into the series of ripples that have been observed following many solar flares.

This study looks to investigate the consistently observed but loosely studied feature of most solar quakes, the anisotropy of their surface wave fronts. This is achieved by analysing the primary effects of two components: Firstly, how do the properties of the local solar atmosphere affect not only the propagation of the waves producing the wave fronts, but also the amount of energy which is lost or returned to the solar surface? Secondly, how prominent are the destructive/constructive effects on the wave fronts, owing to any movement of the solar quake source itself?

A theoretical framework is provided, which underpins the main effects proposed to be causing the wave front anisotropy. A variety of atmospheres and solar quake sources are implemented through the use of supercomputers to achieve full 3D numerical simulations of solar quakes. The results produced are linked to both the theory developed herein as

well as with observations. Clear observations in the vicinity of the solar quake source have proven difficult to obtain due to the complex nature of the environment and the processes occurring within it. Away from the impacting site, the observations become much clearer and the features of the surface wave fronts become more amenable to analysis, which is the area this study focuses upon.

The mechanics behind solar flare generation is an ongoing field of study, with a variety of researchers providing efforts to fully explain both when and where a flare may be excited, as well as the process(es) which govern their onset. Flares have been associated closely with the ejection of plasma and particles into outer space, which have the capacity to reach Earth and may interrupt various important communication channels. Due to solar quakes being a direct energetic consequence of the onset of solar flares, any information regarding their morphology is greatly sought after.
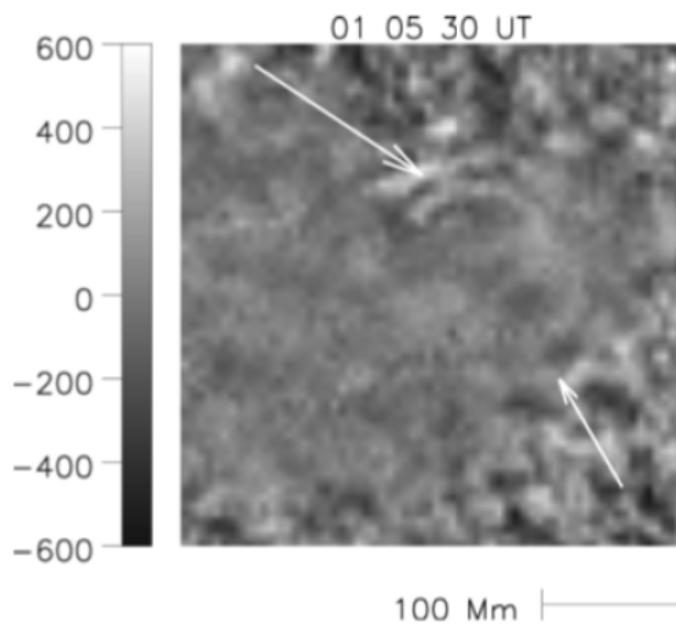

Figure 4.1: Doppler difference image with arrows depicting the distinct circular ridge, which appeared radially outward from the impact site of the 2005 January 15 X-class flare. Doppler difference units displayed on the vertical axis are in ms^{-1}. Image extracted from Moradi et al. (2007).

4.1.1 Observational Evidence

The first observation of a solar quake was made by Kosovichev and Zharkova (1998) using Dopplergrams obtained from data provided by the Solar and Heliospheric Observatory (SOHO). They used the Michelson Doppler Imager (MDI) to produce Dopplergrams to discover conspicuous movement of mass flows of the order of 3-5 Mm across the solar photosphere throughout the July 1996 X2 class flare impulsive stage. This allowed a direct link between the mass movement of material triggered from a solar flare to the production of a seismic transient. These Doppler images are now often remapped to provide seismograms depicting the travel distances of a given surface wave front across the solar surface (see Figure 4.2).
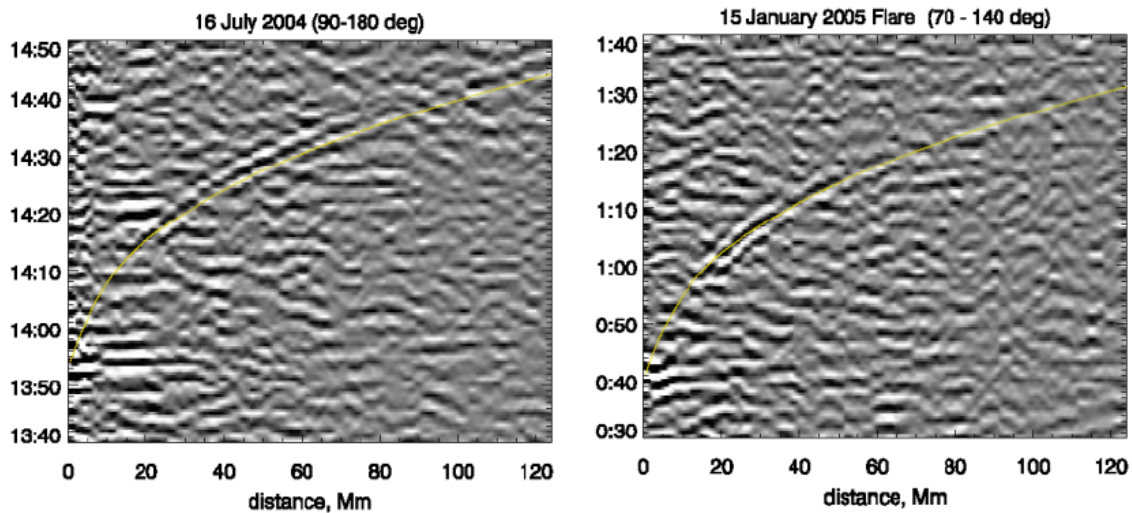
Figure 4.2: Helioseismograms showing the changing location of selected solar quake wave fronts through time on the solar surface. The dark patches refer to negative velocities and white to positive velocities. The images are from quakes associated with a 2004 (*left panel*) and a 2005 (*right panel*) observed X-class flare. The yellow lines superimposed on the images indicate the theoretical time distance arcs of propagating waves produced from a standard solar model. Figure extracted from Kosovichev (2009).

The continual turbulence from within the convection zone of the Sun manifests itself as oscillations of the solar photosphere with periods of approximately 5 mins (2-4 mHz frequency range). Due to this constant granulation of the background atmosphere, it is difficult to observe seismic ripples in the noisy solar background.

A dedicated technique to find seismic signatures is through the use of seismic emission power maps (see bottom-right panel of Figure 4.3) and the computational helioseismic

holography techniques introduced in Donea et al. (1999). These techniques have been utilised and expanded upon to locate a whole host of further solar quakes (Donea, 2011; Donea and Lindsey, 2005; Lindsey and Donea, 2008; Martínez-Oliveros et al., 2008; Donea et al., 2006; Moradi et al., 2006). One interesting aspect of solar quakes that draws attention is the anisotropy found in the acoustic amplitude of the surface wave fronts from the vantage of the source (Kosovichev, 2006; Moradi et al., 2007). In simpler terms, the acoustic emission is much stronger in some directions when compared to others. This prominent feature, which has received little attention in the solar literature has triggered the research presented within this chapter. Figure 4.3 shows Doppler images taken at the onset of the January 15 2005 X1 flare onset, as well as from 40 minutes following. These images clearly show the production of anisotropic wave fronts following a high energy flaring event.

As of now, hundreds of quakes have been identified and can be cross-correlated with flares having an energy classification as low as M-class (Sharykin and Kosovichev, 2019). A summary of the survey data on solar quakes collected by Ionescu (2006) suggests that only a small amount of a flare's total energy is observed through egression power calculations. Extrapolation of this data gives an estimation as to the resolution required to continually identify quakes produced from less and less powerful flares. It is also interesting to note that many high energy X-class flares predicted to produce solar quakes, do not actually induce an observable seismic transient signature and the cause of this is currently unknown. Before discussing the anisotropy of solar quakes, a discussion about the details of solar quake triggering mechanisms is provided.

4.1.2 Triggering Mechanisms

There remains still no consensus as to the actual mechanism which connects the onset of a solar flare to the production of a solar quake. Solar flares occur predominantly in magnetically active regions of the Sun and are powered by an intense sudden release of energy stored in the corona via the process of magnetic reconnection (also sometimes described as magnetic recombination). There is plenty of history in the solar literature for magnetic reconnection with theoretical work beginning as far back as Cowling (1945); Sweet (1950); Parker (1957), whilst numerical simulations (Aulanier et al., 2010, 2012; Kliem et al., 2013), plasma experiments (Ji et al., 1998), and space missions (Farrugia et al., 2016) are becoming more and more prominent in recent years. The myriad of
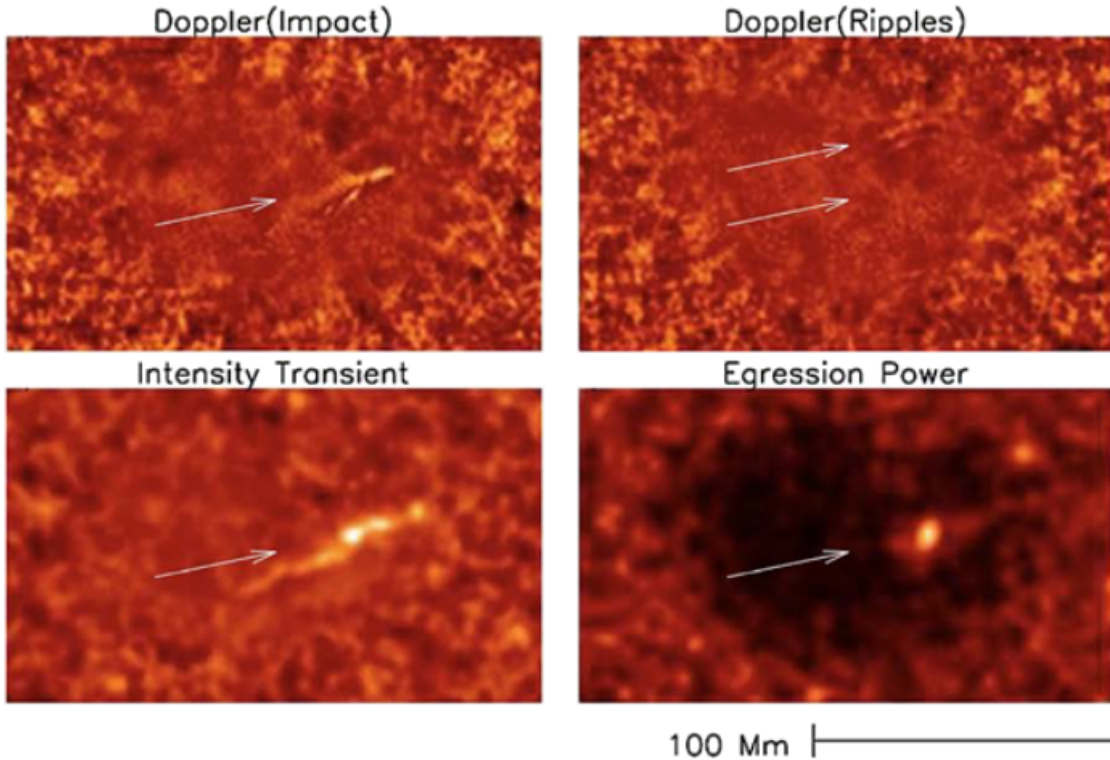
Figure 4.3: X1 flare of January 15 2005. *Top-left*: MDI Doppler image at flare onset. The arrow points to the sudden compact red-shift at the acoustic source. This arrow is reproduced in all other panels at the same spatial location. *Top-right*: MDI Doppler image 40 minutes after flare onset. The additional upper arrow points to the prominent surface ripples. *Bottom-left*: Visible continuum emission observed by GONG co-temporal with the top-left panel. *Bottom-right*: Egression power at flare onset in the 5-7 mHz spectrum reconstructed from the surface ripples using a 15-45 Mm pupil centered on each pixel. Figure extracted from Donea (2011).

processes involved in magnetic reconnection are well described and reviewed by Yamada (2007); Zweibel and Yamada (2009); Yamada et al. (2010); Janvier (2017). The main contribution from magnetic reconnection to this project is twofold: firstly, there is the ability to convert magnetic energy into alternate forms of energy such as kinetic or heat energy, and secondly, a redistribution of magnetic fluxes near the photosphere results in a change to the local magnetic field topology (Somov, 2010). These phenomena can lead to a variety of physical processes, each with their own capabilities of transferring energy back into the solar interior. Garnered from the works listed above (except where otherwise noted) and summarised below are the main proposed mechanisms resulting from solar flare

onset thought to be capable of supplying enough energy to incite an observable seismic transient.

Photospheric Backwarming

After the solar flare and magnetic reconnection occurs, plasma containing high energy particles such as electrons and protons can flow along the field lines. The particles streaming towards the solar surface will impact collisionally in the chromosphere, resulting in the temperature of the associated plasma rising significantly. This is balanced by the plasma releasing extreme ultraviolet (EUV) and ultraviolet (UV) line radiation as well as the emission of free-bound continua from hydrogen and other ions. This radiation is carried via photons and can penetrate into the photosphere, supplying enough energy to cause a seismic transient. Co-spatial and co-temporal comparisons of continuum emission and acoustic emission emanating from flare impact sites which were later found to produce solar quakes is strong evidence for a causal relationship between the two (Donea and Lindsey, 2005). Various theories spawning from works including Donea (2011); Lindsey and Donea (2008); Moradi et al. (2007) have been developed to explain directly the link between the continuum emission and consequent heating of the photospheric layers. This heating would cause an increase in pressure, supplying the force needed to drive an acoustic shock wave into the solar surface, which in turn produces the seismic transient. The bottom left-hand panel of Figure 4.3 shows the signature of sudden visible continuum emission observed by GONG during the flaring event of January 15 2005.

Despite the apparent spatial and temporal links between the acoustic and continuum emissions, there appears to be a large discrepancy in the magnitude of these energies. A crude estimate of the energy deposited into a seismic transient (see Lindsey and Donea (2008) for full derivation) can be estimated as

$$\Delta W \sim \frac{p_0^2}{32 \rho_0 g} \frac{(\delta F_{rad})^2}{F_{rad0}^2}, \tag{4.1}$$

where p_0, ρ_0 and F_{rad0} are the pressure, density and continuum flux of the undisturbed photosphere, and δF_{rad} and ΔW are the changes in continuum flux and energy deposited into the seismic transient. Utilising equation (4.1), Lindsey and Donea (2008) find a reasonable agreement between energy outputs of the continuum and acoustic emissions. However, uncertainties in the Global Oscillation Network Group (GONG) measurements, the non-consideration of magnetic fields, small data sets and simple assumptions involved in

the derivation of equation (4.1) need to be addressed in order for photospheric backwarming to be considered a proven mechanism for quake generation.

Chromospheric Shocks

Recent studies have shown the lower chromosphere and photosphere to be a possible site of sunquake excitation (Zharkova and Zharkov, 2015; Sharykin et al., 2017). The underlying idea, which has been termed the 'chromospheric shock' theory describes a process whereby the incoming energetic particles flowing along field lines collide with those in the lower chromosphere. An intense evaporation of the surrounding material ensues, creating distinct regions of high and low pressure. This process happens at such a rate that the plasma is now capable of moving at speeds much greater than the local sound speed. This process causes 'chromospheric shocks', which may travel uninhibited into the photosphere with enough energy to excite the acoustic waves needed to produce seismic transients (Kosovichev, 2015; Macrae et al., 2018). In response to this proposed mechanism, Allred et al. (2005) produced a study using hydrodynamic modelling of chromospheric shocks. The results of this study suggested that radiative losses inflicted throughout the photosphere are such that the shocks could not account for the measured acoustic energy in seismic transients observed to date.

Particle Triggers

Further to observations of high energy protons producing gamma ray emission associated with the aforementioned photospheric backwarming, hard X-ray emissions are also found in co-spatial and co-temporal regions, suggesting the additional presence of high energy electrons (Zharkova and Zharkov, 2007). Due to the spatial and temporal alignment of these two potential energy sources, it becomes difficult to distinguish whether protons or electrons are responsible for transporting the energy to the seismic transient and to what degree. Kosovichev (2007) presents Reuven Ramaty High Energy Solar Spectroscopic Imager (RHESSI) data from the July 23 2002 flare, which shows gamma ray emission with no co-spatial seismic response, whilst a joint gamma ray/hard X-ray emission is aligned with a seismic response. The gamma ray fluxes recorded at each particular site were of similar magnitude, which lead the author to conclude that high energy electrons are responsible for seismic transient production.

Lorentz Forces

The sudden change in the magnetic field topology leads to an impulsive Lorentz force to act upon the surrounding area, depositing energy which can be responsible for powering a seismic transient. Fisher et al. (2012) proposed the change in Lorentz force per unit area over time to be given as

$$\frac{\partial F_z}{\partial t} = \frac{1}{8\pi} \int_A dA \; \frac{\partial}{\partial t}(B_\perp^2 - B_z^2) \qquad (4.2)$$

where $B_\perp$ and B_z are the magnitudes of the magnetic field perpendicular and vertical respectively and A is the area of the solar surface experiencing the changing magnetic field - in this case the flare footprints. Sudol and Harvey (2005) found significant magnetic field changes to the low photospheric levels upon all surveyed flare release sites, including the 2003 October 29 flare, which excited an acoustically active seismic transient. However, specific values pertaining to this event have not been made available. Utilising equation (4.2), Alvarado-Gómez et al. (2012) measured line-of-sight magnetic field variations of the photosphere after the 2011 February 15 X-class flare impact to produce estimates for the magnitude of the Lorentz force excited. Their results produced a lower limit calculation describing a 6% contribution by the Lorentz force to the total acoustic energy of the seismic transient. They further their analysis by extrapolating the data to suggest that the line-of-sight measurements are underestimates to what could be a Lorentz force contribution in the order of 20%. These values suggest the contribution to the energy of seismic transients is non-negligible and cannot be discounted when accounting for the total energy required to produce a solar quake.

The possible triggering mechanisms addressed above are all capable of providing at least part of the acoustic source energy need to produce a solar quake. Due to the nature of the sources, it is possible and perhaps common, that the sites of the impacts are non-stationary and involve motion perpendicular to the solar surface. Owing to this, the importance of source movement in understanding the morphology of solar quake observations is now investigated.

4.1.3 Source Movement

Additional radio, hard X-ray and gamma-ray observations are being collected to study high energy particles being accelerated following the onset of a solar flare (eg., Aschwanden

et al. (2002); Hurford et al. (2003)). More specifically, particle motion transverse to the solar surface has been observed, suggesting that any impacting source can be non-stationary. One prominent theory to explain this behaviour is the contraction or relaxation of magnetic loops following the recombination phase experienced after a solar flare (Russell et al., 2015). This causes the foot-points containing the magnetic field lines to move either closer to or away from each other, but most importantly, transverse to the solar surface. Particles travelling along these moving field lines, thought to be responsible for solar quake generation, should emit radiation. Kosovichev (2007) provided one such example (see Figure 4.4), where transverse motion of up to 50 km/s is observed through hard X-ray observations following the onset of the July 23 2002 solar flare, which produced a solar quake.

4.1.4   Motivation for Study

The mechanism(s) of solar flare generation are an integral part in understanding the workings of the Sun. Considering solar quakes are a direct energetic response to some high energy flares, it is natural they become an important area of interest. Their appearance on the solar surface as a series of anisotropic surface wave fronts (ripples) lends itself to investigation. The reproduction of this feature through 3D numerical modelling should help further the understanding around the mechanisms thought responsible for generating the quakes. These mechanisms are closely involved with the processes of the propagation and acceleration of electrons and ions, and may provide an insight into these phenomena. Further to this, and due to their intense nature and location, solar quakes have the ability to provide detailed local helioseismic data for magnetically active regions of the Sun. Thus, a greater understanding of their photospheric responses (surface ripples) becomes integral.

4.2   Ray Path Tracing: Acoustic Waves in a Quiet Sun Atmosphere

Regardless of the mechanism which leads to the production of a seismic transient, what follows an energetic impact with the photosphere is the motion of pressure waves through various sections of the Sun's interior to eventually re-emerge at the surface. It is therefore instructive to look at the path in which a typical wave would take as it propagates underneath
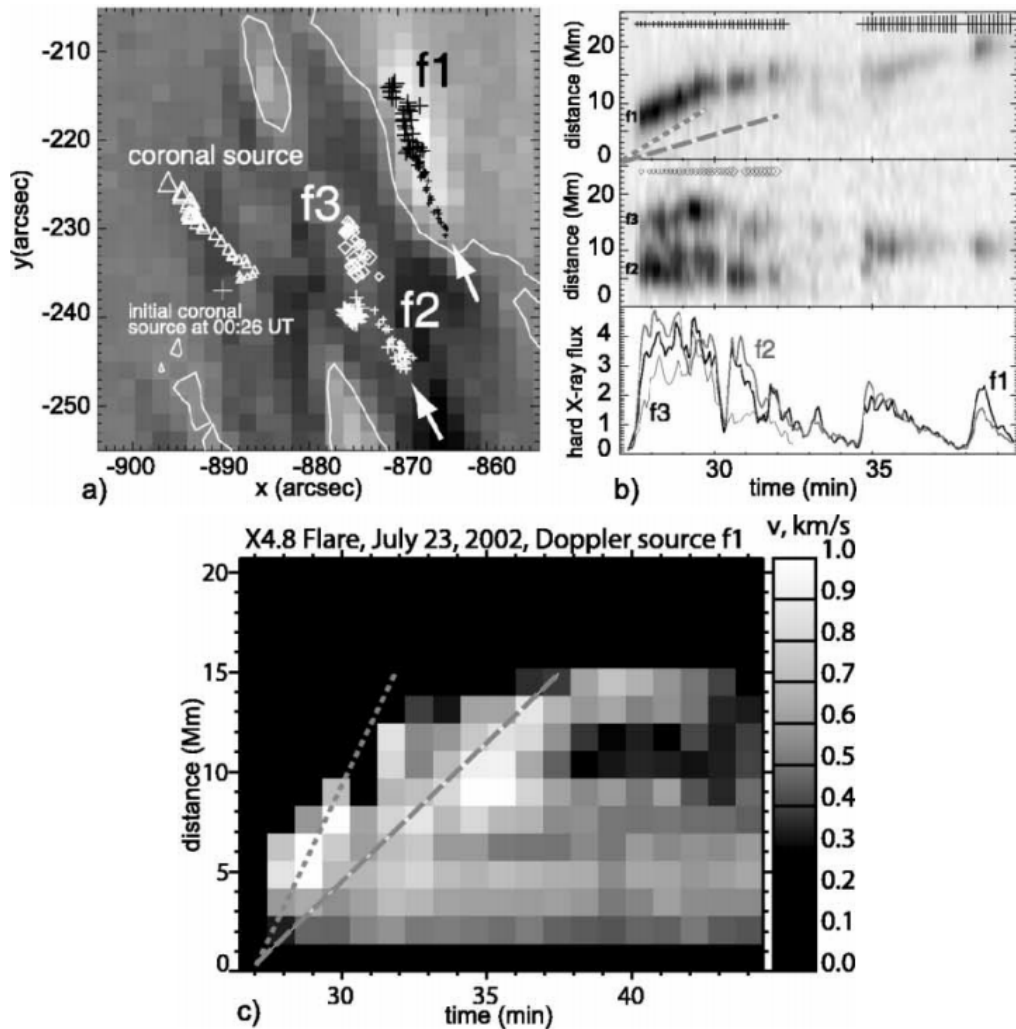
Figure 4.4: Observations from the July 23 2002 flare, which produced a solar quake. (a) Hard X-Ray source evolution. Increasing symbol size represents time progression from 00:26:35 to 00:39:07 UT. (b) Hard X-Ray profiles along the flare ribbons showing supersonic speeds - the grey dashed line depicts a speed of 25 km s^{-1} and the dotted line similarly for 50 km s^{-1}. (c) Doppler velocity profiles along the f1 ribbon, showing motion with an average speed of $\sim$ 25 km s^{-1}. Figure extracted from Kosovichev (2007).

the photosphere. Standard MHD ray theory, as related by Moradi and Cally (2008) and Newington and Cally (2010), is based on the dispersion function

$$\mathcal{D} = \omega^2 \omega_c^2 a_\perp^2 k_h^2 + (\omega^2 - a^2 k_\parallel^2) \times \Big[\omega^4 - (a^2 + c^2)\omega^2 k^2$$
$$+ a^2 c^2 k^2 k_\parallel^2 + c^2 N^2 k_h^2 - (\omega^2 - a_z^2 k^2)\omega_c^2 \Big]. \quad (4.3)$$

Here, ω is the angular frequency, k_h and $k_\parallel$ are the horizontal and field-aligned components of the wave vector respectively, a is the Alfvén speed, c is the sound speed, a_z is the vertical component of the Alfvén velocity, and $a_\perp$ is the component perpendicular to the plane containing the wave vector $\vec{k}$ and gravitational acceleration $\vec{g}$. N is the Brunt-Väisälä frequency, defined as

$$N = \sqrt{\frac{g}{H} - \frac{g^2}{c^2}}, \quad (4.4)$$

where H is the density scale height. The acoustic cut-off frequency, ω_c can have a variety of representations and this is discussed in detail through the introduction of Chapter 3. For this analysis we restrict ourselves to the traditional isothermal form

$$\omega_c = \omega_{ci} = \frac{c}{2H}. \quad (4.5)$$

The associated ray equations are

$$\frac{d\vec{x}}{d\tau} = \frac{\partial \mathcal{D}}{\partial \vec{k}}, \qquad \frac{d\vec{k}}{d\tau} = -\frac{\partial \mathcal{D}}{\partial \vec{x}}, \qquad \frac{dt}{d\tau} = -\frac{\partial \mathcal{D}}{\partial \omega}, \qquad \frac{dS}{d\tau} = \vec{k} \cdot \frac{dx}{d\tau}, \quad (4.6)$$

where $\vec{x} = (x, y, z)$ is position, S is phase, t is time, and τ is the parameterisation of the ray. The atmosphere is a smooth concatenation at the photosphere of two well known models: the subsurface layers are based on the Model S by Christensen-Dalsgaard et al. (1996) and the chromospheric layers are taken from the quiet Sun model listed in Avrett et al. (2015).

By specifying a height z and a frequency ω, then by allowing $k_z = 0$, equation (4.3) where $\mathcal{D} = 0$ will give a solution for k_x using a root finding mechanism. Now that k_x is defined, equation (4.6) can be integrated numerically to solve for the path of the ray. This method acts to 'shoot' the ray from its lower turning point at $x = 0$ in both horizontal directions. The integration is continued until both rays either reach the surface at $z = 0$ or their upper turn over height, i.e., when $dz/dt = 0$ is reached. By doing this, one full skip of the ray can be visualised, such as those presented in Figure 4.5. This formulation allows a time-distance analysis for injected rays to be investigated.
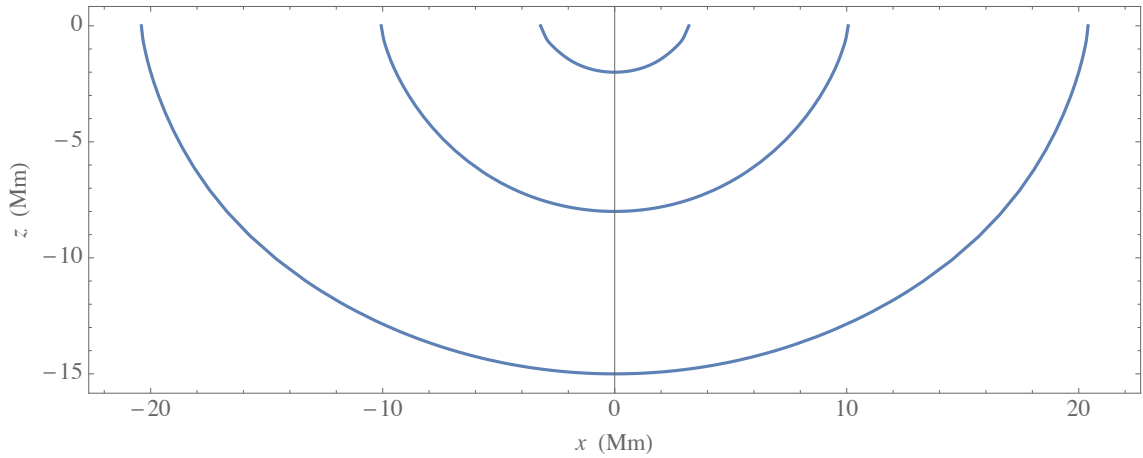
Figure 4.5: Typical ray paths showing the first horizontal skip in $x - z$ space with lower turning points at $z = -15, -8$ and -2 Mm. No background magnetic field is present and a frequency of 6 mHz is chosen.

4.2.1 Time-Distance Analysis

By utilising the above technique, injected rays may have their first skip distance and associated travel times recovered from the ray equations. Seismic sources as triggers of solar quakes have been detected at frequencies from 3-10 mHz (Zharkov et al., 2011). Rays with typical solar frequency values of $5 - 15$ mHz and a collection of appropriate lower turning point heights are chosen to be investigated. The heights were selected such that the horizontal first skip distance of the rays spanned a range of approximately $6 - 50$ Mm, sufficient to fully encompass the area of interest (this point is explained in detail in section 4.4.1). The time-distance relationships are shown in Figure 4.6.

The most striking feature of the time vs. skip distance plots is the non-linearity of the relationship between the two. Increasingly less time is required for the rays to travel a given distance as skip distance increases. As the rays travel deeper, they experience an acceleration due to the increasing sound speed with depth. Therefore, we expect to see the surface ripples accelerate with increasing distance from impact point, a feature noted as far back as the first solar quake observation by Kosovichev and Zharkova (1998). An increase in frequency also sees the rays travel slightly faster, more so at large skip distances. The implementation of a non-zero magnetic field showed a small increase in skip distance at later times for high magnitude strongly inclined fields. These types of atmospheres are very rarely observed and therefore the effect of magnetic field can essentially be ignored
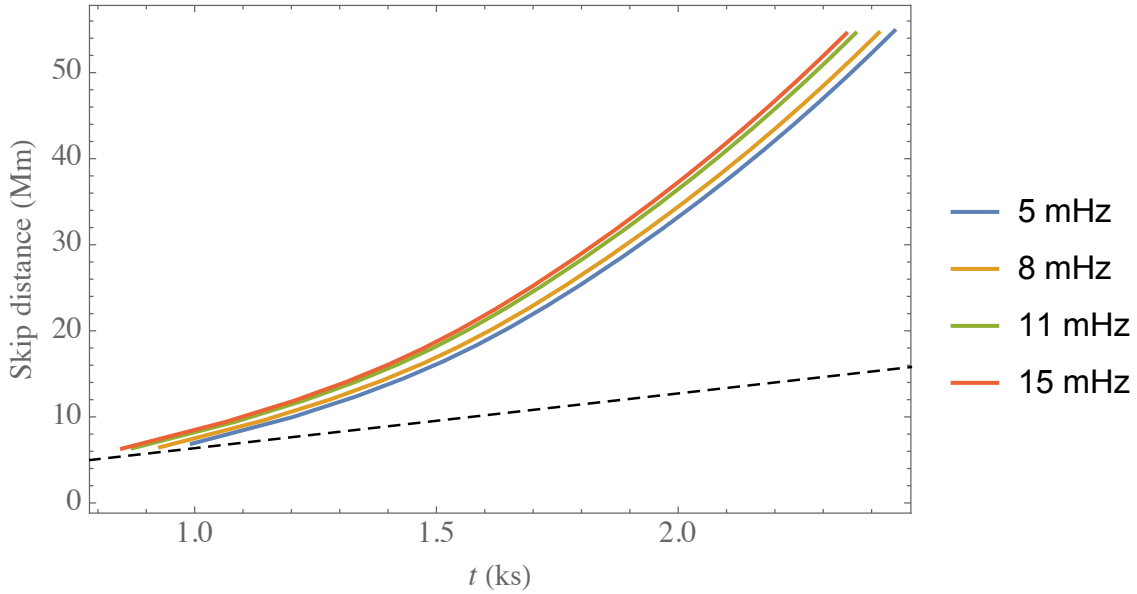
Figure 4.6: First skip distance plotted against time for rays with typical solar frequency values of $5 - 15$ mHz for an atmosphere with no background magnetic field. The dashed line shows the travel distance and time for a particle moving along the surface ($z = 0$) at the local sound speed $c = 8.18$ km/s.

for this purpose.

The main effect of using the isothermal acoustic cut off compared to alternate versions is that the rays will reflect higher near the surface and hence will be more affected by the magnetic field.

As these waves progress through the solar interior, they can lose or convert some of their energy before returning to the surface. The most prominent mechanism for this in the region of interest is mode transmission/conversion, the effects of which are now discussed in some detail.

4.2.2 Transmission and Conversion

Due to the constant solar granulation, a weak signal at the surface is likely to be lost in the background noise. Therefore, any loss of energy from the pressure waves between their initial production and their return to the surface should be taken into account. The most prominent form of energy loss when studying acoustic waves propagating through the magnetic solar interior occurs around the equipartition layer, where the sound speed

coincides with the Alfvén speed. At this point, the incoming acoustic ray splits its energy into two modes, acoustic and magnetic, a process known as linear mode conversion (Schunker and Cally, 2006). Only the formula will be introduced here as a full discussion of this phenomenon is related in detail through the introduction section of Chapter 2. The proportion of energy remaining on the prescribed ray path after interaction with the $a = c$ layer is described by the transmission coefficient

$$
\begin{aligned}
\mathcal{T} &= \exp\left[-\frac{\pi h K^2 k_\perp^2}{|k_z|(K^2 + k_\perp^2)}\right]_{a=c} \\
&\approx \exp\left(-\frac{\pi h k_\perp^2}{|k_z|}\right)_{a=c} \text{ for } |k_\perp| \ll K \\
&= \exp[-\pi K h_s \sin^2 \alpha]_{a=c},
\end{aligned}
\tag{4.7}
$$

where K is the wave number, k_z and $k_\perp$ are the vertical and perpendicular components of the wave vector respectively, a is the Alfvén speed, c is the sound speed, and $\alpha = \arcsin(k_\perp/K)$ is the attack angle, the angle that the wave vector makes with the magnetic field - the wave vector being tangent to the ray at any given point. Also implemented above is the equipartition scale height $h = [d(a^2/c^2)/dz]_{a=c}^{-1}$, the measure of thickness of the layers in which $a \approx c$, along with $h_s = [d(a^2/c^2)/ds]_{a=c}^{-1}$, the measure of thickness along the path traced out along the direction of the phase velocity $\hat{k}$. The first part of equation (4.7) is the exact formula, which is used for any calculations herein, whereas the final formula is an approximation used to help accentuate to the reader the effect of the attack angle α. A small attack angle, the angle between the wave vector and the magnetic field, leads to greater transmission from slow-fast or fast-slow modes. Figure 4.7 can be used to visualise the effect of linear mode conversion on rays with differing lower turning points and background magnetic field strengths - this image should be used for illustrative purposes only.

As the wave reaches the $a = c$ layer, its energy will be split into acoustic and magnetic modes. A given amount of acoustic energy will remain on the depicted ray path (transmission), whilst the remaining magnetic energy is funnelled along the magnetic field lines (conversion) into the solar interior and becomes lost for the purpose of this study. A large attack angle at the $a = c$ layer leads to less transmission and consequently less energy staying on the ray path and being carried back to the surface.

For a vertical magnetic field, the attack angle is increased when a) the trajectory of the ray is shallower and b) when the magnetic field is stronger. In fact, this is in general true

for most constant non-vertical magnetic fields with typical solar active region strengths and inclinations when looking at the first skip distances of importance. Figure 4.8 shows the transmission coefficients for various magnetic field arrangements, which highlight the points mentioned above. These values have been scaled by the inverse skip distance as any energy contained along this path will decrease inversely proportional to r, where r is the radial distance from the impact site. It can be seen that the magnetic field strength plays a greater role than the field inclination when considering these transmission values, especially at lower skip distances. This is an important result as both the magnitude and inclination of the magnetic field can vary greatly in atmospheres where solar quakes are commonly found, such as the magnetic canopy of a hosting sunspot. Sunspot magnetic fields can vary in magnitude from 700 - 3700 G (Livingston, 2002; Solanki, 2003) and their field lines can bend up to 35° from vertical at the penumbra/umbra boundary (Jurčák, 2011).

Any wave passing through the $a = c$ layer will of course pass back through this layer after reflecting at its lower turning point and before reaching the surface. At this point, a further splitting of the energy into the acoustic and magnetic modes will occur. For an upwards travelling wave, the proximity of the $a = c$ layer to the height of measurement ($z = 0$ surface) means these modes will be almost indistinguishable - this is especially true for magnetic fields with small inclination from vertical, as is common in solar atmospheres. It is not until higher up in the atmosphere where the plasma beta level drops significantly that it is possible to meaningfully separate the different wave modes. Therefore, it becomes difficult to draw meaningful conclusions from the mode conversion theory at this point and the nuances are considered more theoretical than practical. Any further development and application of the theory would be beyond the scope of the study at hand.

In line with the above considerations, it is important to reiterate that these findings and representations are only characteristic of the processes involved and should be used purely as a guide to assist in explaining any results forthcoming. The mode-conversion theory was also developed in a 2-D environment. It is thought to extend consistently to further dimensions but as of now, its results should only strictly be applied parallel to the plane of the magnetic field, i.e. with no azimuthal angle.
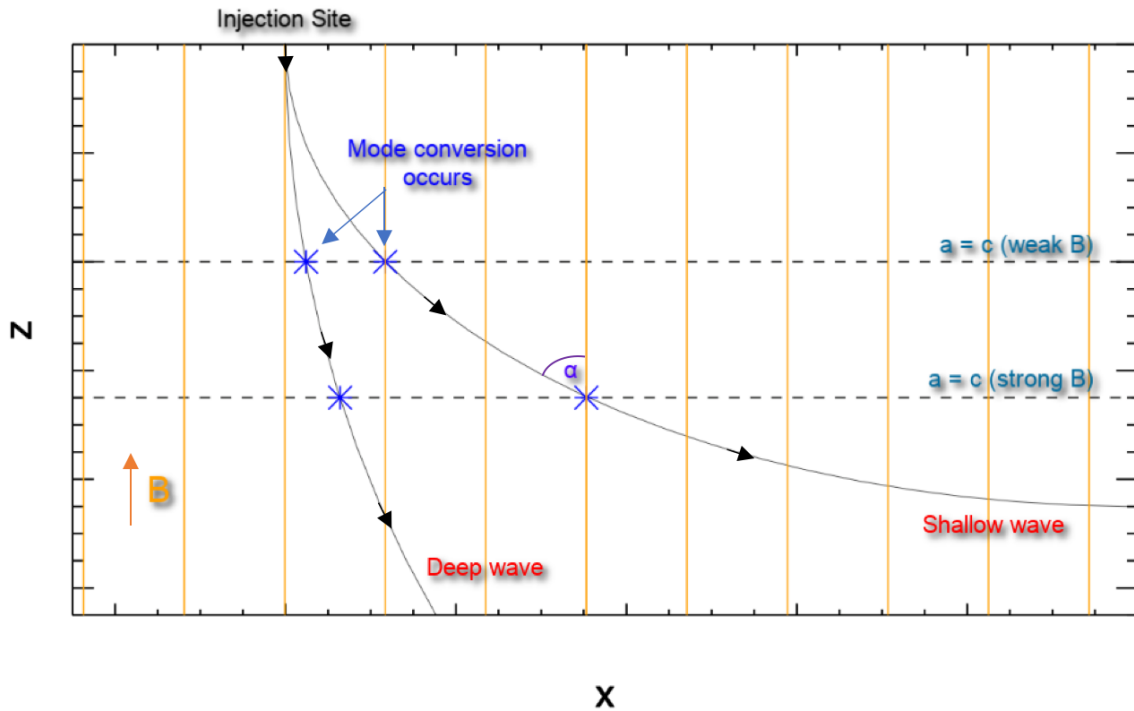
Figure 4.7: Illustrative image showing typical paths for shallow and deep rays (solid lines) injected at the same point at the top of the box. The dashed lines refer to two different potential $a = c$ layers - the stronger the magnetic field the deeper the location of this layer. The star points refer to the points where linear mode conversion will take place. The crucial 'attack angle' α is measured at these star points. The background orange lines depict the vertical magnetic field lines. For a vertical magnetic field, a larger attack angle occurs when the trajectory of the ray is shallower and when the magnetic field is stronger. The rays will pass through the $a = c$ layer again before returning to the surface (not shown).

4.3 2D Wave Equation

The analysis continued by looking at the solutions to the 2D wave equation for acoustic waves, described here as

$$\frac{\partial^2 u}{\partial t^2} = c^2 \nabla^2 u + v(x, y, t), \tag{4.8}$$

where u is the change in position from equilibrium, c is the sound speed, v is the input source function, t is time and (x, y) are the spatial positions. The solutions to this equation help to visualise the potential effects of constructive and destructive interference at the solar surface. It is important to note that this equation describes a two-dimensional set-up whereby the waves are constrained to travel along a horizontal (x, y) plane at the sound
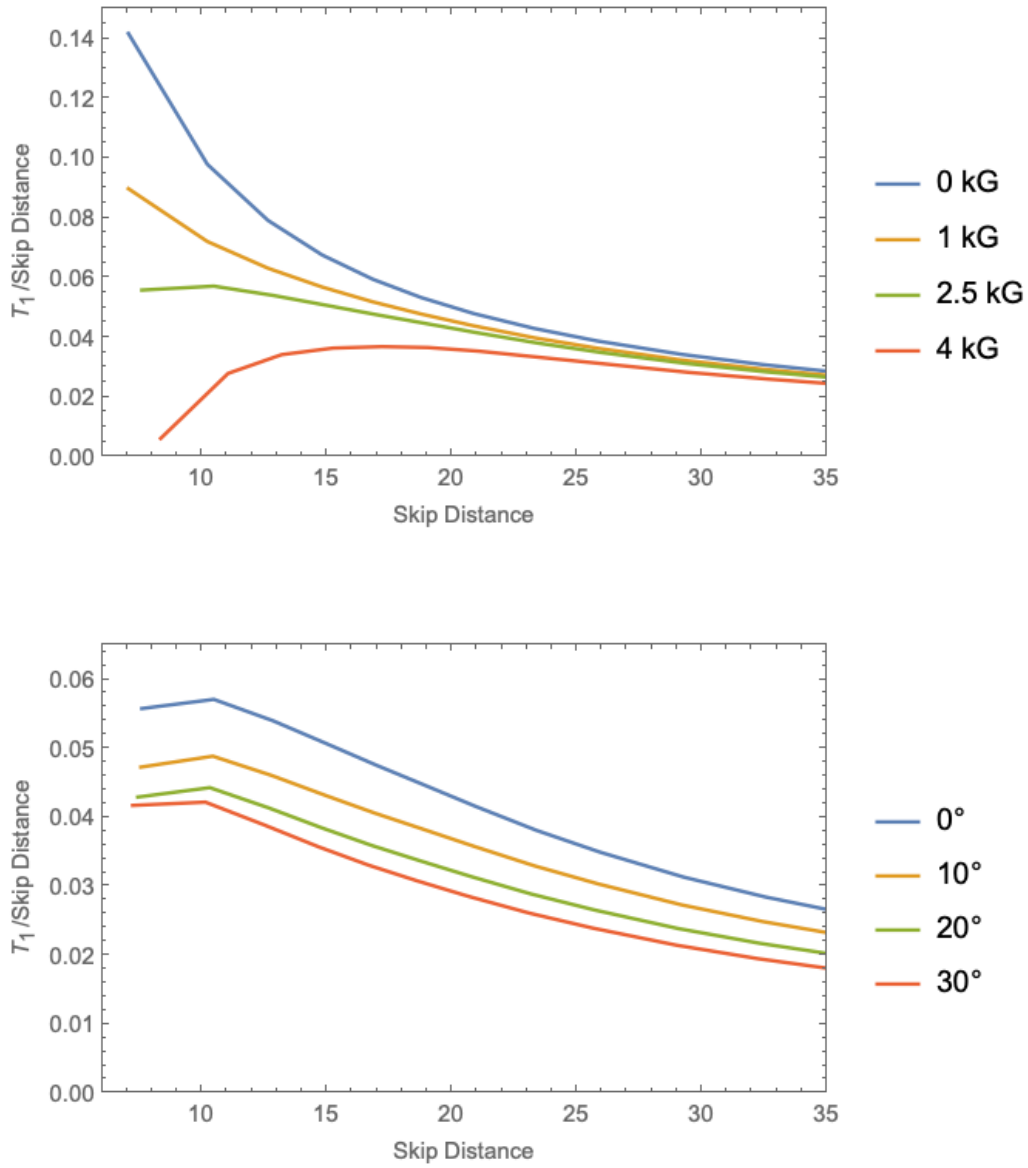
Figure 4.8: Transmission Coefficient $\mathcal{T}_1$ vs first skip distance for a 6 mHz ray travelling through various magnetic and non-magnetic atmospheres. The top image corresponds to a vertical magnetic field with magnitudes listed appropriately and the bottom image corresponds to a 2.5 kG magnetic field with inclinations from vertical listed appropriately. All values have been scaled by the inverse skip distance. The plots are truncated for small skip distance when a particular ray does not travel deep enough to intersect with the $a = c$ layer. Note: No $a = c$ layer exists for a non-magnetic field, in this case, $\mathcal{T}_1 = 1$.

speed. It was seen in subsection 4.2.1 that for increasing skip distance, the actual waves travel ever deeper into the solar interior and propagate at speeds much greater than the sound speed. The results presented should therefore be interpreted on a qualitatively instructive basis only.

The initial condition is

$$u = \frac{\partial u}{\partial t} = 0, \quad \text{at } t = 0$$

and the source function is given by

$$v = \delta(x - bt)\,\delta(y)\,e^{(-i\omega t - \sigma t)}, \quad \text{when } t > 0, \tag{4.9}$$

where δ is the delta function, b is the source speed in the x direction, ω is the angular frequency and σ is a source decay factor.

This is solved by taking the Laplace-Fourier Transform of equation (4.9), which gives the solution in Laplace-Fourier space as

$$u(k, l, s) = \frac{v(k, l, s)}{s^2 + c^2(k^2 + l^2)}, \tag{4.10}$$

where k and l are the x and y wavenumbers respectively, and s is the Laplace variable. By inverting the Fourier transform in l and then the Laplace transform in s separately, along with the application of the convolution theorem, gives

$$W(t) = \int_0^t F(k, y, t)\,G(k, t - \tau)d\tau. \tag{4.11}$$

Here, τ is a time parameter,

$$G(k, t) = \frac{\exp\left[-t(-ibk + \sigma + i\omega)\right]}{2c\sqrt{2\pi}}, \tag{4.12}$$

and

$$F(k, y, t) = J_\theta(ck\sqrt{t^2 - y^2/c^2})\,\theta(t - |y|/c), \tag{4.13}$$

where J_θ is the Bessel function of the first kind and θ is the Heaviside step function.

A final inverse Fourier Transform in k on the integrand $F(k, y, t)\,G(k, t)$, and further simplification produces the solution under these conditions as

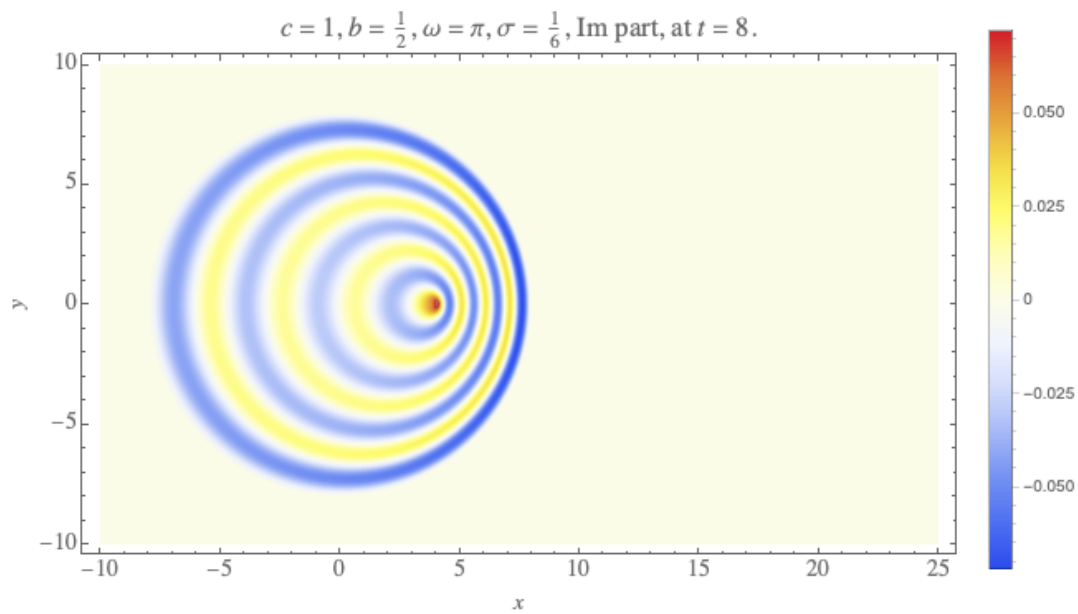$$u(x, y, t) = \int_0^t H(x, y, t, \tau)\,d\tau, \tag{4.14}$$

Figure 4.9: 2D wave equation results for a source moving at subsonic speed ($b = c/2$) with full equation parameters listed above.
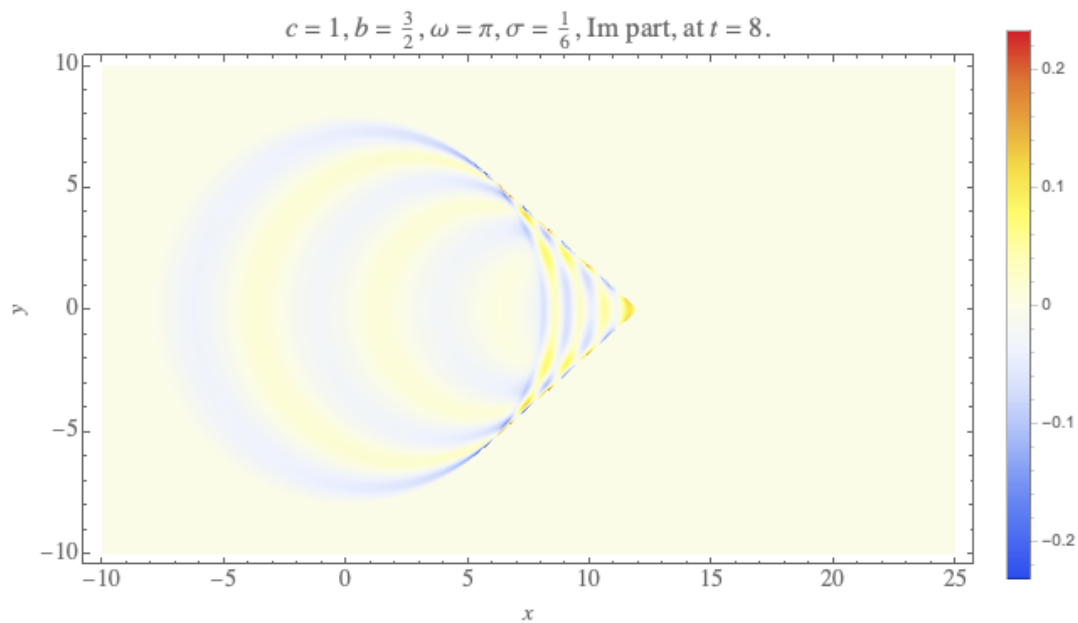

Figure 4.10: 2D wave equation results for a source moving at supersonic speed ($b = 3c/2$) with full equation parameters listed above.
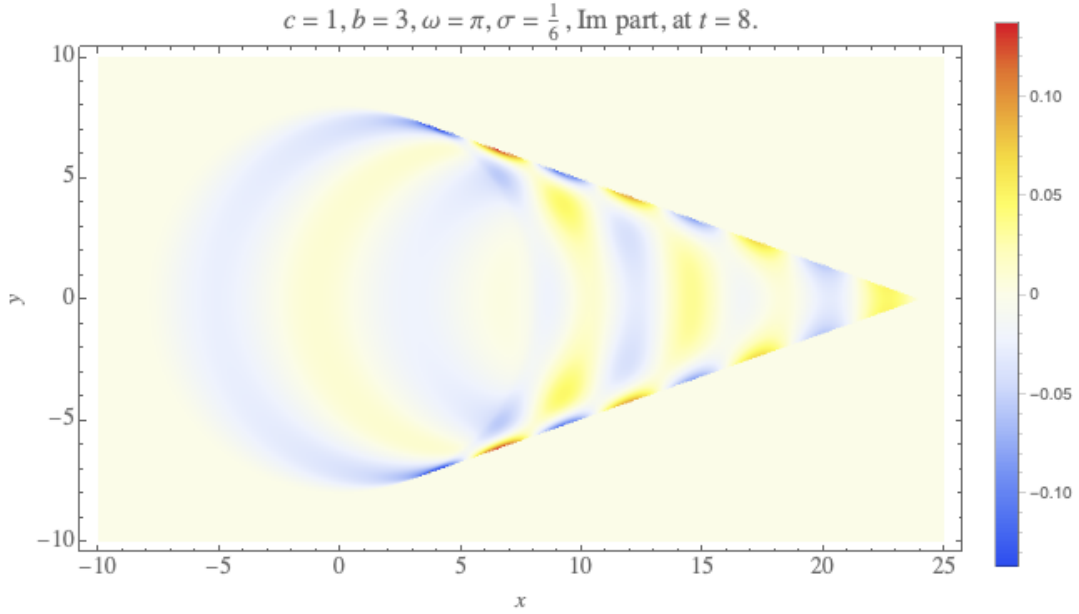
Figure 4.11: 2D wave equation results for a source moving at highly supersonic speed ($b = 3c$) with full equation parameters listed above.

where

$$H(x,y,t,\tau) = \begin{cases} \frac{\exp\left(-(t-\tau)(\sigma+i\omega)\right)}{2c\pi\sqrt{c^2\tau^2-(b(\tau-t)+x)^2-y^2}} & , \quad \text{if } c^2\tau^2 > (b(\tau-t)+x)^2 + y^2 \\ 0 & , \quad \text{otherwise.} \end{cases} \quad (4.15)$$

Cases with a variety of source speeds (here, the variation of parameter b) are chosen for investigation and selected examples are shown in Figures 4.9, 4.10 and 4.11. The values corresponding to the equation parameters are stated above each plot. For all cases, the sound speed $c = 1$, the frequency $\omega = \pi$, the decay factor $\sigma = 1/6$ and the solution output is the imaginary part (sine driver) given at time $t = 8$. These parameters have no real significance other than the decay factor. This value was chosen so that a decay in energy is affected, as predicted by the mode conversion theory, whilst not damping the signal too much to render it unobservable.

The stationary source with no decay factor (not shown) produces a set of unremarkable concentric rings as expected. This scenario represents seismic waves dispersing uniformly in all directions, which is rarely observed in the solar photosphere. The introduction of a moving source with subsonic velocity (Figure 4.9) shows the signal is preferentially strongest along the direction of motion. If the decay factor is removed, the signal is even

stronger on this side. A supersonic source (Figure 4.10) again shows the strongest signal along the direction of motion, however the constructive interference is beginning to spread across the envelope on this same side. When the source speed is highly supersonic (see Figure 4.11) the interference along the envelope is even further enhanced.

In conclusion, a simple implementation of the 2D wave equation has shown the strongest constructive interference to be found when using a moving source. This interference is found predominantly on the side aligned with the direction of motion of the source, although a change in the magnitude of the source speed (subsonic versus supersonic) results in differing coherence patterns. Areas of most intense signal migrate to the envelope as source speed is increased. Stronger signals are also found with zero decay factors, as expected, but this is in general unrealistic.

These results are important for studying the anisotropy of seismic ripples observed in the solar photosphere, where the constructive interference of waves can luckily render the seismic signal visible within the noisy background granulation of the quiet Sun. Through numerical modelling of waves imparted into model solar atmospheres, the effect of source movement, mode conversion and wave destructive/constructive interference on the ensuing surface wave fronts should be realised.

4.4 Numerical Model for Generating Solar Quakes

This section outlines the numerical procedure taken to produce solar quakes in model solar atmospheres with a variety of source functions. The computational modelling is conducted via the use of the SPARC MHD code, which solves the linearised 3D Euler equations in Cartesian geometry (Hanasoge, 2011). The numerical domain consists of 512 cells in both the x and y directions which span a length of 100 Mm in both directions. Perfectly Matched Layers or PMLs (see Berenger (1994, 1996) for the theoretical background and Hanasoge et al. (2010) for the implementation used here) over 10 grid cells are utilised on all side boundaries, which restrict the horizontal grid spacing to 203 km. The PMLs also require the use of a sponge, which calls into the question the notion of a 'perfectly matched' layer, however it has been shown to perform well for a variety of models studying linearised wave propagation (Felipe et al., 2010; Przybylski et al., 2015; Santamaria et al., 2015). There are 600 cells in the z direction, covering a span of heights from -15 Mm to 1.5 Mm and again, perfectly matched layers are implemented at the bottom (10 cells)

and top (15 cells) boundaries. The vertical grid spacing is variable and based on the local sound speed. At the temperature minimum, this spacing is as low as 10.3 km, and stretches to 69.6 km at the bottom of the computational box.

The comparatively large horizontal grid spacing is still sufficient for the computations at hand. We require $k_x \Delta x \ll 2\pi$, where k_x is the horizontal wave number, which is constant for each individual ray due to the homegeneity in the atmpsphere for horizontal directions. By choosing an extreme case with a shallow lower turning point at $z = -2.0$ Mm - these will return to the surface at radii $|x| \geq 6.0$ Mm - and a relatively high frequency of 15 mHz, it can be seen that $k_x \Delta x = 1.44$. Values for k_x will decrease for all deeper waves and also for those with lower frequencies - the bulk of the source driver's energy is imparted well below this value of 15 mHz (see Figure 4.12). Waves returning at radii $|x| < 6.0$ Mm are of less importance to this study and the reader is again referred to section 4.4.1 for an explanation of this.

To produce the initial hydrodynamic equilibrium, the same smoothly joined atmosphere as described previously in section 4.3 is implemented.

The driving source is the purely velocity based perturbation

$$v_z(x, y, z, t) = \begin{cases} A \exp\left[-\left(\frac{|\vec{r}-\vec{r_0}|^2}{2\vec{\sigma_r}}\right)\left(\frac{(t-t_0)^2}{2\sigma_{t_1}}\right)\right], \text{ when } t < t_0 \\ A \exp\left[-\left(\frac{|\vec{r}-\vec{r_0}|^2}{2\vec{\sigma_r}}\right)\left(\frac{(t-t_0)^2}{2\sigma_{t_2}}\right)\right], \text{ when } t \geq t_0 \end{cases} \tag{4.16}$$

where $\vec{r} = (x, y, z)$ are the spatial co-ordinates, $\sigma_r = (500, 500, 50)$ km, $\vec{r_0} = (x_0, y_0, z_0) = (0, 0, 0)$, t is time, $\sigma_{t_1} = 3.0$ s, $\sigma_{t_2} = 100.0$ s and $t_0 = 10.0$ s. If the moving pulse is implemented, then

$$x_0 = x_0 + s_x t, \tag{4.17}$$

where s_x is the horizontal speed responsible for shifting the site of the impacting source function. The amplitude A is ascribed a negative value, whilst due to the linearity of the numerical code, its actual magnitude is not important except to ensure numerical rounding is never realised throughout the computations. This piece-wise source function is implemented to best model the onset of the impacts based on observational results. The impacting pulse should reach its maximum amplitude quickly before decaying at a much slower rate. The Fourier transform for the source over its full driving time is displayed in Figure 4.12 and shows a broad spectrum of frequencies are imparted into the domain.
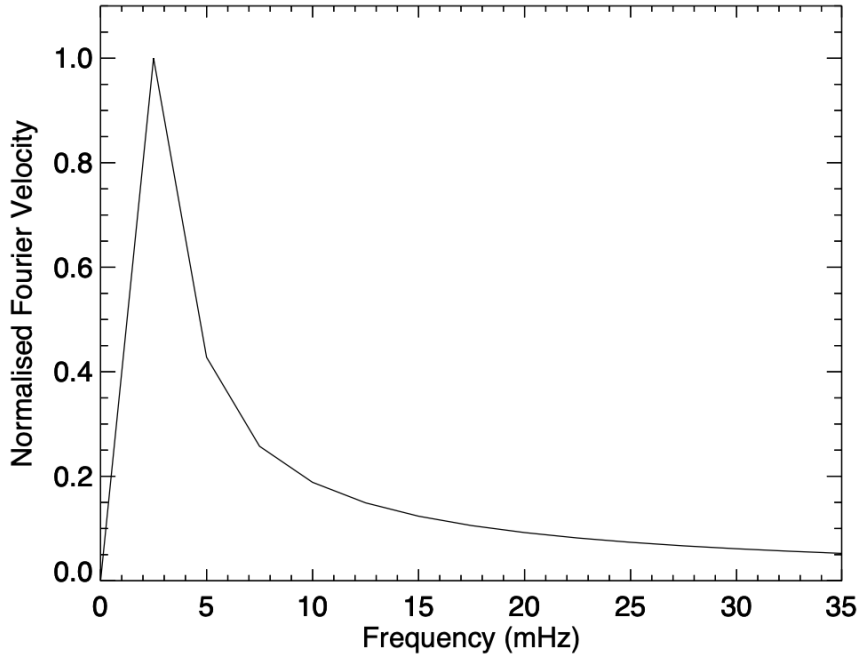
Figure 4.12: Normalised Fourier velocity spectrum for the driving source.

4.4.1 Restricted Signal Radius

There appears to be no information in the current literature that describes the minimum distance from impact site at which solar quake wave fronts have been observed. By looking through the various time-distance diagrams available in the literature, it is proposed that it is rare to see a signal within much less than 10 Mm of the initial source. There could be any number of reasons to explain this, one being due to the confounding effects imparted by the magnetic fields present in the photosphere and shallow subphotospheres. These magnetic fields suppress the photospheric signatures of acoustic waves from below and can shift their phases significantly, an effect known as the acoustic showerglass effect (Schunker et al., 2005; Lindsey and Braun, 2004, 2005a,b). At small radii, the waves responsible for any observed solar quake traverse predominantly through these shallow depths and would be most affected by such a phenomenon.

In any case, the presented results are often restricted to radii $|x| \geq 6.0$ Mm from the impacting site due to the observational evidence at present showing solar quake signatures almost exclusively at these distances and greater. This restriction also importantly provides the necessary leeway to conduct 3-D numerical modelling without the complicated set-ups that would be necessary to achieve the required numerical precision over such a large span

of horizontal distance.

4.5 Simulation Results

A variety of simple magnetic and non-magnetic atmospheres are chosen for investigation, coupled with the implementation of both stationary and moving sources. Observations have shown the existence of both source movement and anisotropic solar surface wave fronts in magnetically active regions and the simulation parameters are chosen to best investigate these phenomena. This leads to various surface measurements being presented here, which best elucidate the anisotropy observed in the simulated wave fronts. Each simulation is run for a total of 1.25 hours of simulated solar time.

4.5.1 Stationary Source

Initially, an acoustic (non-magnetic) atmosphere is used to develop a base line for comparison to further magnetic atmospheres. A general decrease in the amplitude of the vertical velocity v_z is observed moving radially out from the impacting site as would be expected. Following this, a constant vertical magnetic field is introduced with magnitudes of 1 kG and 2.5 kG, respectively. Figure 4.13 shows that as the magnetic field strength is increased, the amplitudes of the vertical velocity v_z in the surface wave fronts are decreased. Furthermore, the increased magnetic field strength leads to the location of the peak velocity being shifted to increasing spatial distances in the order of $10 - 20$ Mm. These observations match well with the theoretical work developed through subsection 4.2.2. The main argument is that the increased field strength leads to the $a = c$ layer being shifted deeper into the atmosphere. This causes the attack angle - at the first interaction with the mode conversion region - to increase, which leads to a decrease in the amount of energy eventually propagating back to the surface. This effect will be most prevalent for waves with high ℓ values, as is common in spherical harmonic analysis. These are waves which will return at small distances from the impacting site and it can be seen quite clearly that the results bear this out.

It is now chosen to set a constant magnetic field strength, whilst the angle of the field from vertical is varied from 0° - 30°, a feature commonly found in magnetically active regions. As shown in Figure 4.14, an increase in the magnetic field angle leads to a general decrease in velocities measured at the surface. This can be explained with the same logic
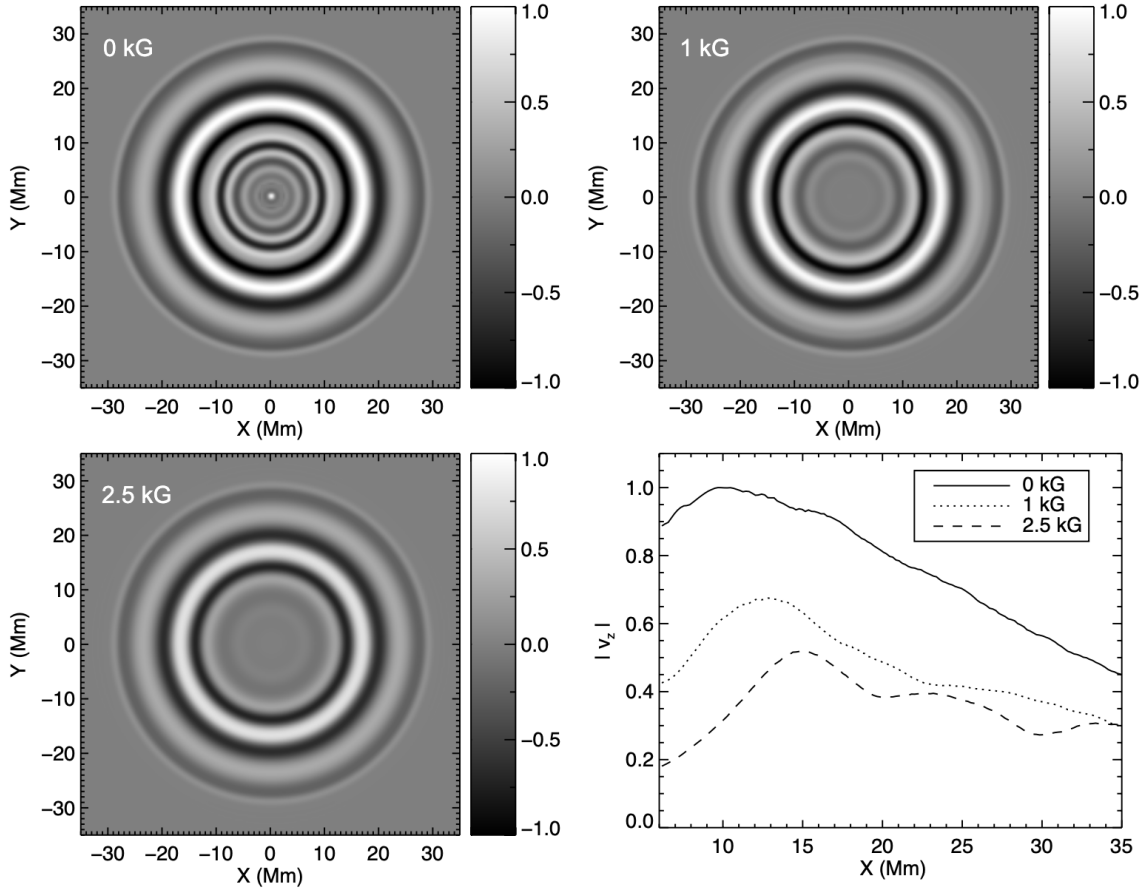
Figure 4.13: Vertical velocity v_z snapshots at the surface $z = 0$ from time $t = 27.5$ mins for a variety of non-magnetic and magnetic atmospheres. *Top-left*: No magnetic field. All surface plots have been normalised to the maximum value of this particular plot. *Top-right*: 1 kG constant vertical magnetic field. *Bottom-left*: 2.5 kG vertical magnetic field. *Bottom-right*: Vertical velocity magnitudes $|v_z|$ (normalised to the non-magnetic case) along the $y = 0$ central axis at the surface $z = 0$ for the magnetic field strengths listed, averaged over the entire duration of the simulation.

as above, in that the increasing field angle leads to an increased attack angle around the $a = c$ layer. This lowers the amount of transmission through those areas and less energy returns to the surface. The peak velocities for increasing inclination angle are shifted only slightly to greater horizontal distances from the impact site.
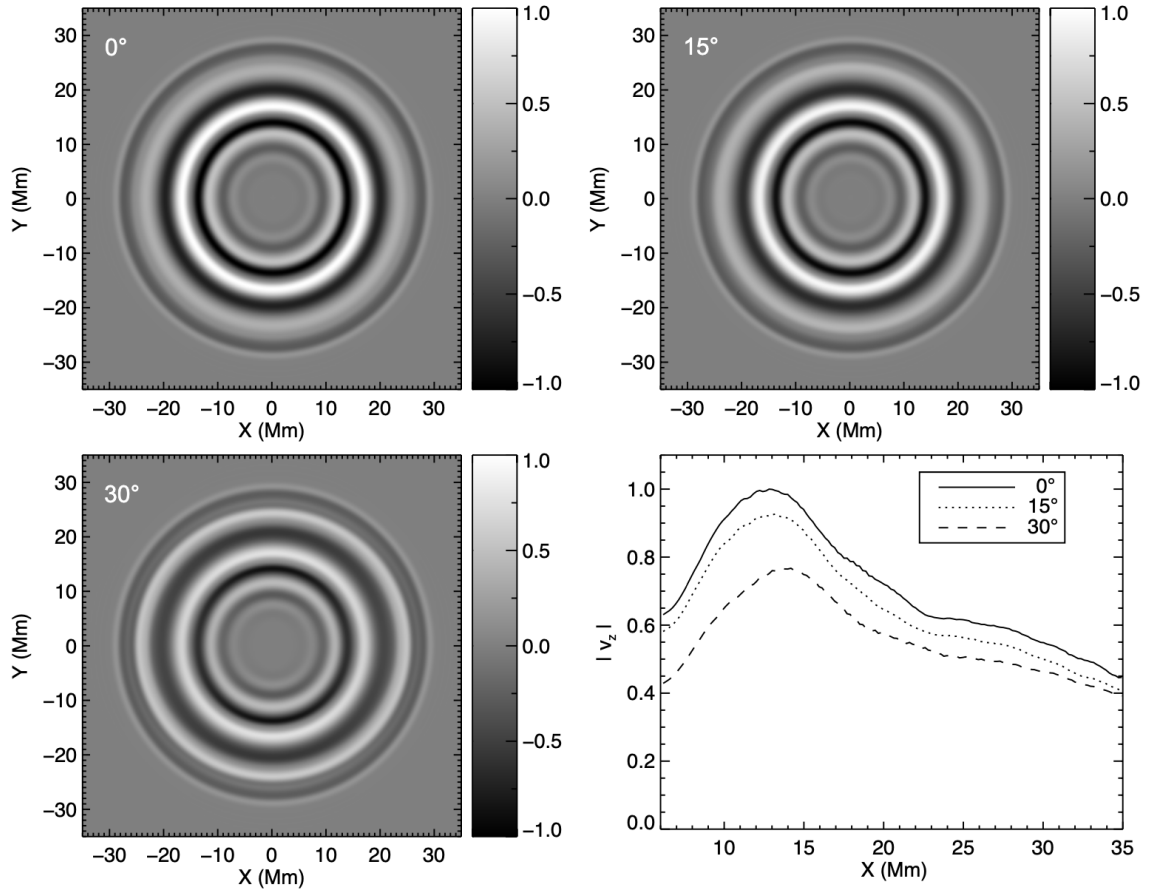

Figure 4.14: Vertical velocity v_z snapshots at the surface $z = 0$ from time $t = 27.5$ mins for 1 kG magnitude background magnetic fields. *Top-left*: Vertical magnetic field. All surface plots have been normalised to the maximum value of this particular plot. *Top-right*: 15° inclined field from vertical. *Bottom-left*: 30° inclined field from vertical. *Bottom-right*: Vertical velocity magnitudes $|v_z|$ (normalised to the vertical field case) along the $y = 0$ central axis at the surface $z = 0$ for the magnetic field inclinations listed, averaged over the entire duration of the simulation.

Also showing in the results for the non-vertical magnetic fields are slight anisotropies in the shape of the surface wave fronts when viewing in the y-direction compared to the x-direction, and also in the positive x-direction against the negative x-direction. Throughout

the area of interest especially, these differences are considered small enough to warrant little further investigation. This is to both limit the scope of the discussion and to concentrate on those effects which are considerably more pronounced.

4.5.2 Moving Source

In line with observations, a moving source function is introduced. This will move the impacting site towards the positive x-direction at a given speed s_x, which is varied from as low as a sub-sonic velocity up to greatly super-sonic velocities. The measurement of the local sound speed to quantify these speeds as sub and supersonic is taken only at the surface.

The sub-sonic source $s_x = \frac{c_s}{2}$ produces some enhancement of the signal along the direction of motion, especially at early times and hence, smaller distances from impact site (see Figure 4.15). By increasing the source speed to equal that of the sound speed, this effect becomes much clearer and up to $\sim$22.5 mins after impact, the maximum increase in signal compared to the stationary source is in excess of 100% (see Figure 4.16). Continual increase of the source speed to 20 km s^{-1} only further enhances the constructive interference. Here, the amplitude of the wave fronts can reach almost three times that produced from the stationary source (see Figure 4.17). If the source speed is continually increased, eventually the type of interference pattern is altered. Figure 4.18 shows a 50 km s^{-1} source speed, which depicts very different resulting wave fronts to those produced from the other moving sources. Multiple envelopes of interference are created, which are restricted to specific sectants of the surface. The strength of the signal centred directly along the direction of motion may appear to be suppressed, however this is due to the stark increase in amplitude of the signal in the developing envelopes. Hence, constructive interference is still present along the direction of motion.

The results presented for the moving source are consistent with the calculations developed in section 4.3. They show dramatic increases in signal strength at the surface through the effects of constructive and destructive interference. As predicted, the source speeds required to produce the same types of coherence patterns seen through the 2-D wave equation solutions become increasingly larger. This is due fundamentally to the waves travelling in a 3-D space, as they encounter increased local sound speeds for heights below the surface.
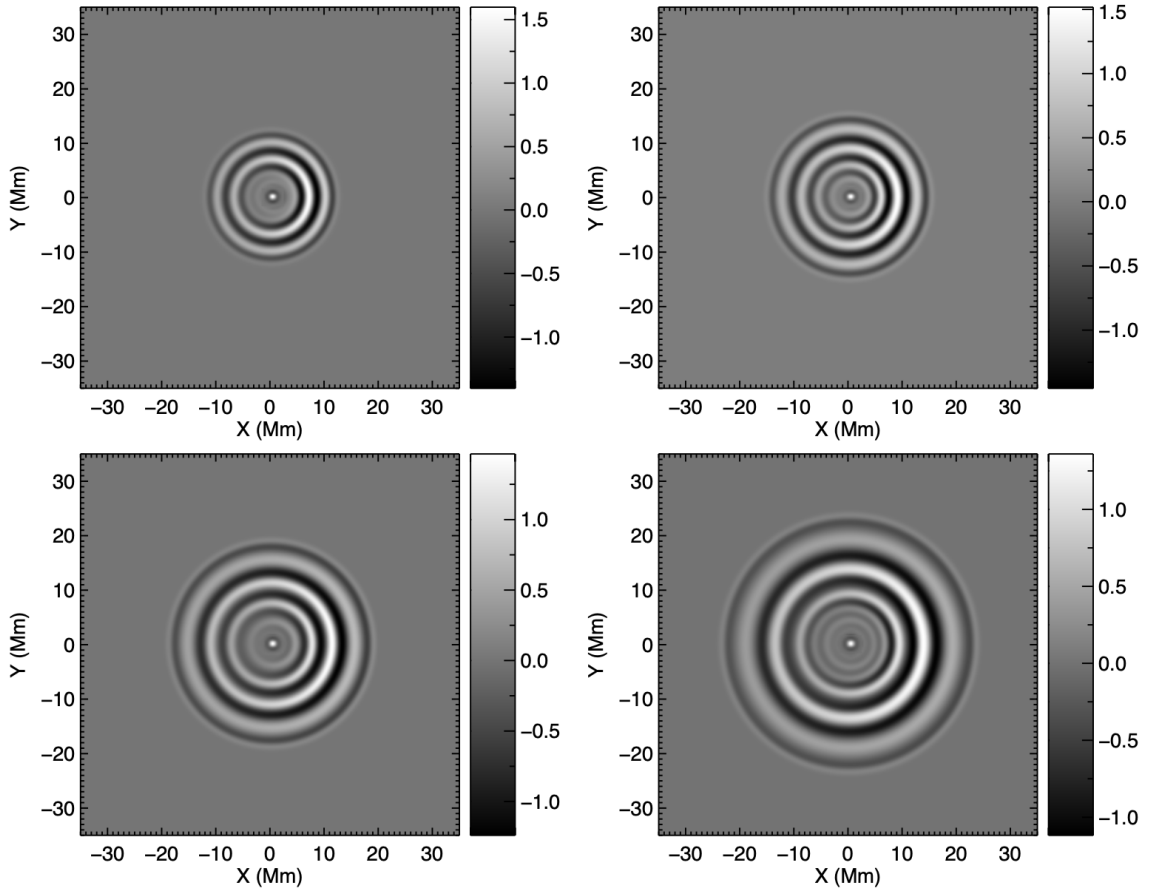
Figure 4.15: Measurements of v_z taken at the surface at times $t = 17.5$, 20.0, 22.5 and 25.0 mins from top-left to bottom-right, respectively. Horizontal velocity of the source function is well below the sound speed at the surface $s_x = \frac{c_s}{2} = 4.1$ km s^{-1}. There is no background magnetic field. The v_z values have been normalised against the maximum values recorded in the stationary source case for each corresponding time slice to highlight the magnitude increase.

Figure 4.16: Measurements of v_z taken at the surface at times $t = 17.5$, 20.0, 22.5 and 25.0 mins from top-left to bottom-right, respectively. Horizontal velocity of the source function is the sound speed at the surface $s_x = c_s = 8.2 \, \mathrm{km \, s^{-1}}$. There is no background magnetic field. The v_z values have been normalised against the maximum values recorded in the stationary source case for each corresponding time slice to highlight the magnitude increase. Note the anisotropy that builds up as the ripples expand.
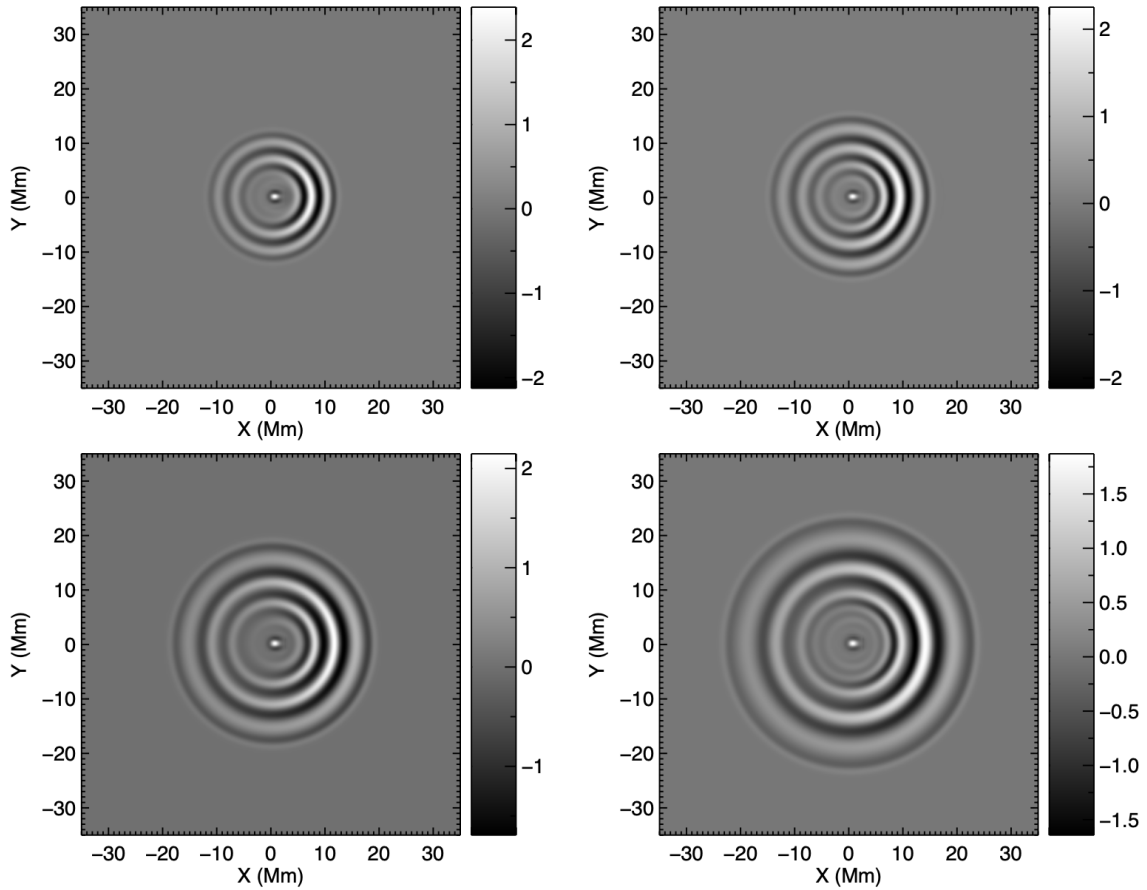
Figure 4.17: Measurements of v_z taken at the surface at times $t = 17.5, 20.0, 22.5$ and 25.0 mins from top-left to bottom-right, respectively. Horizontal velocity of the source function exceeds that of the sound speed at the surface $s_x = 20$ km s^{-1}. There is no background magnetic field. The v_z values have been normalised against the maximum values recorded in the stationary source case for each corresponding time slice to highlight the magnitude increase.
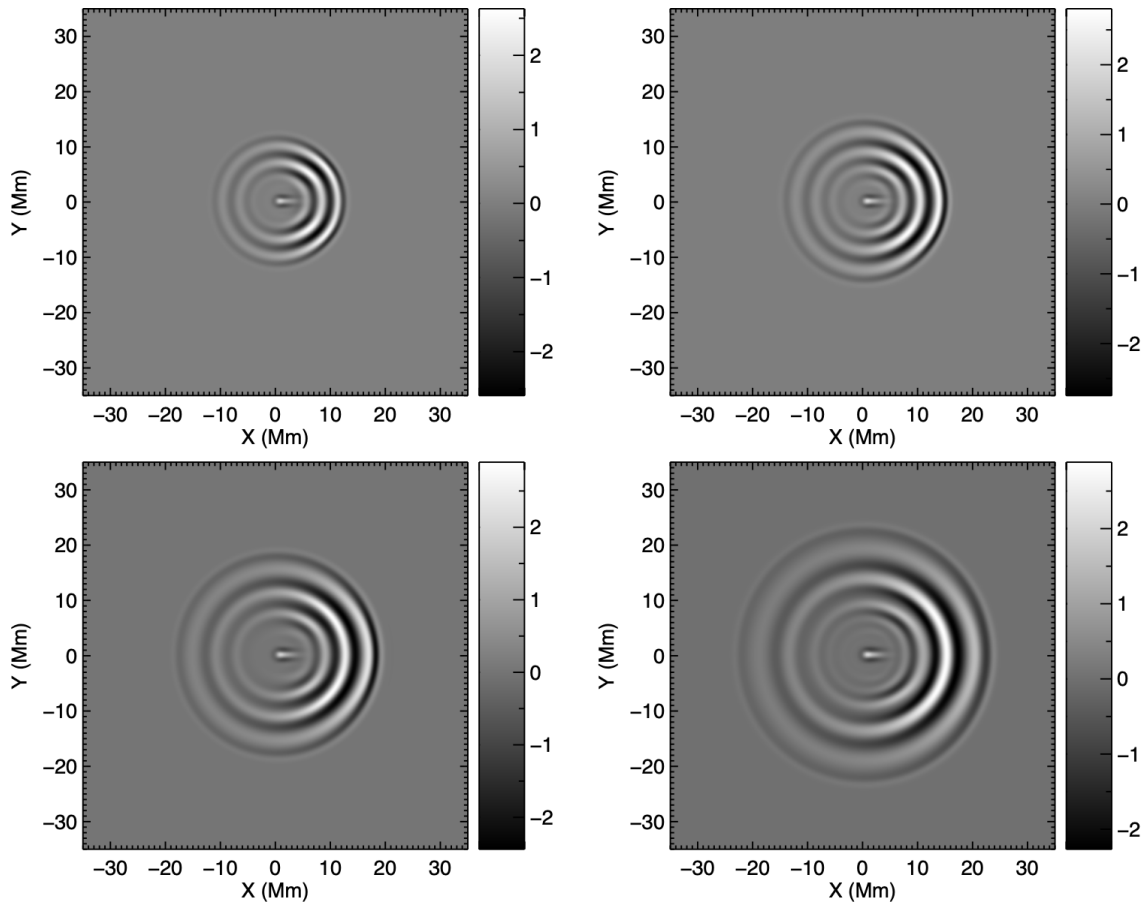
Figure 4.18: Measurements of v_z taken at the surface at times $t = 17.5, 20.0, 22.5$ and 25.0 mins from top-left to bottom-right, respectively. Horizontal velocity of the source function greatly exceeds that of the sound speed at the surface $s_x = 50$ km s^{-1}. There is no background magnetic field. The v_z values have been normalised against the maximum values recorded in the stationary source case for each corresponding time slice to highlight the magnitude increase.
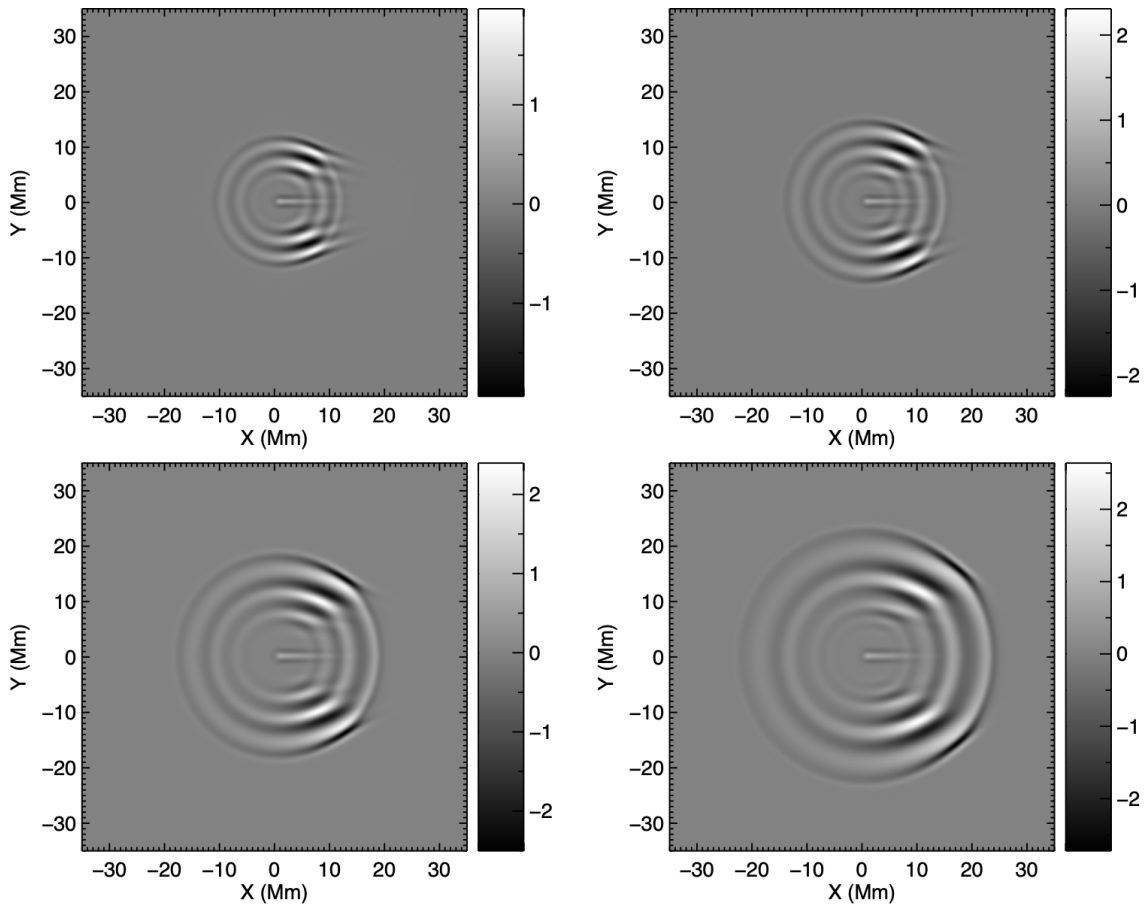
4.5.3 Wave Propagation Discussion

By viewing time-distance outputs for the non-magnetic case, the propagation of the various waves becomes apparent (see Figure 4.19). The most prominent waves are those involved in the first-skip. These can be seen to accelerate with increasing distance from impact site. In line with the above results, a general linear decrease in signal strength is also apparent. At further times, consecutive skips are observed with continually reduced signal strengths. Also faintly visible are the surface f-modes with dispersion relation $\omega^2 = gk$. These are incompressive gravity waves propagating horizontally and are independent of the sound speed. These form a minor component in the simulations and will be ignored for the purpose of our results. Figure 4.20 shows the same time-distance depictions for the variety of magnetic atmospheres used. The shifting of peak strength mentioned previously is readily apparent and a general loss of strength is seen throughout all atmospheres and especially for further skips. The f-modes have become negligible in strength and are not observed.

All listed variations in magnetic field strength and inclination showed little difference in the propagation speeds of the wave fronts. Figure 4.21 gives confirmation of this by tracking the peak of the wave front with the strongest signal as it progresses out radially from the impact site. The selection of this particular wave front is not significant - various other wave fronts were tried and gave essentially the same results. All measurements were transposed in space as to begin at $x = 6.2$ Mm from time $t = 0$. This is both for consistency as the wave fronts themselves are not unique between simulations and due also to the wave fronts not being clearly defined near the impact site. Tracking the wave fronts in any direction radially outwards from the impact source showed very little change in results. The wave fronts produced in the non-magnetic case show the slowest propagation speed. All magnetic cases are found to travel at similar speeds, whilst not being significantly faster than the non-magnetic case. This similarity in propagation speed is due to the strongly acoustic nature of the returning waves below the $a = c$ layer, which is where they spend most of their travel time. The continual increase in velocity of the wave fronts with distance from impact site is consistent with that found in subsection 4.2.1.
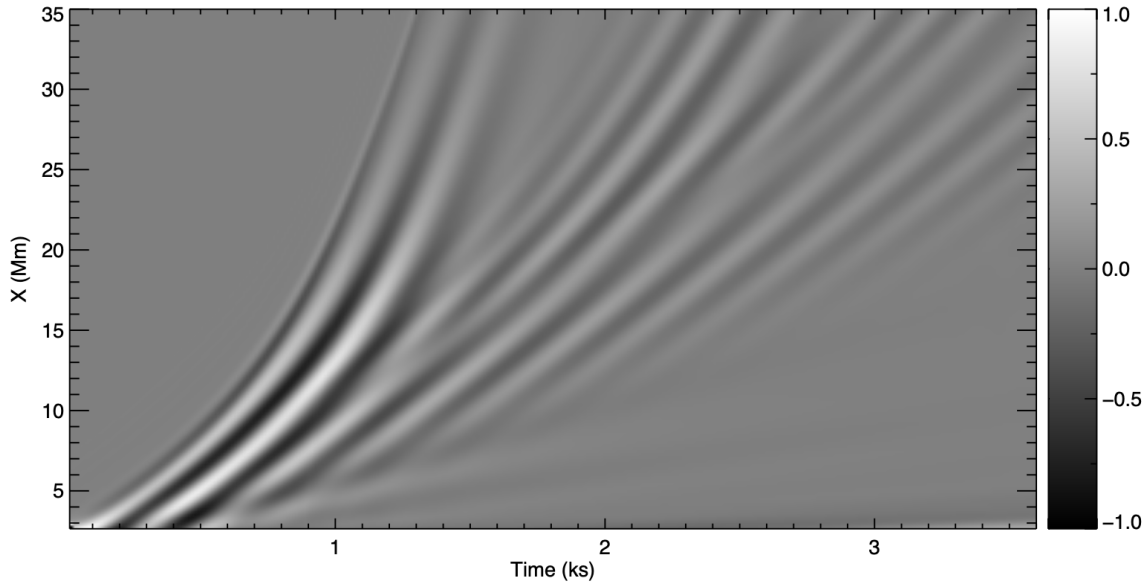
Figure 4.19: Normalised plots of v_z taken over the first hour of simulation in the positive x direction for the stationary source $s_x = 0$ with no background magnetic field.

4.6 Conclusion

Gaussian based perturbations in vertical velocity were introduced into a variety of simple magnetic fields, characteristic of the conditions observed in solar atmospheres. Utilising the mode-conversion theory, coupled with visualisations of the surface wave fronts, several anisotropic features of the wave fronts owing to the various magnetic field configurations were elucidated and discussed.

Due to the constant background solar granulation, only strongly enhanced signals are currently detectable at the solar surface. This is thought to be the reason why only the highly energetic M and X-class solar flares have been known to produce solar quakes. However, even some of the strongest observed flares do not produce quakes. The results presented herein depict the conditions under which a conceivable explanation for this phenomenon can be reached. The theory must now meet with observations.

An increase in both magnetic field strength and inclination play little role in altering the propagation speeds of the surface wave fronts, yet they do lead to weaker amplitudes being observed. However, these effects are considered secondary in importance. It is concluded that the cause of the greatest anisotropies in the surface wave fronts can be attributed to the motion of the impacting source. Constructive and destructive interference occurs in
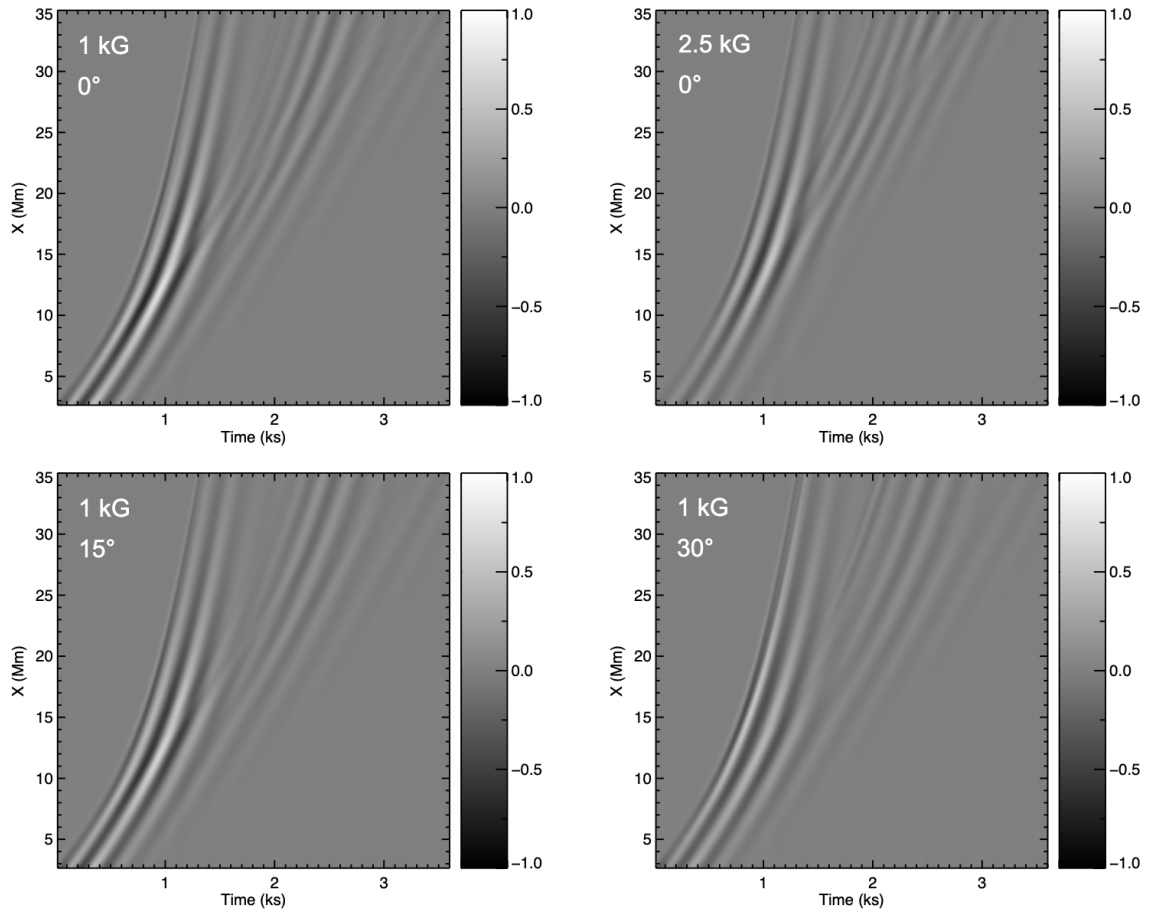
Figure 4.20: Plots of v_z taken over the first hour of simulation in the positive x direction for the stationary source $s_x = 0$. The background magnetic field strengths and inclinations are from top-left to bottom-right: 1 kG 0°, 2.5 kG 0°, 1 kG 15°, 1 kG 30°. All plots have been normalised to the non-magnetic case shown in Figure 4.19.

such a way as to enhance the acoustic signal along the direction of motion. There exists different patterns and strength of interference, which can be explained by the variation in source speed. Increasing the speed of the source generally acts to enhance the signal. Increasing the source speed sufficiently (> 20 km s^{-1}), eventually leads to the development of envelopes of enhanced signal.

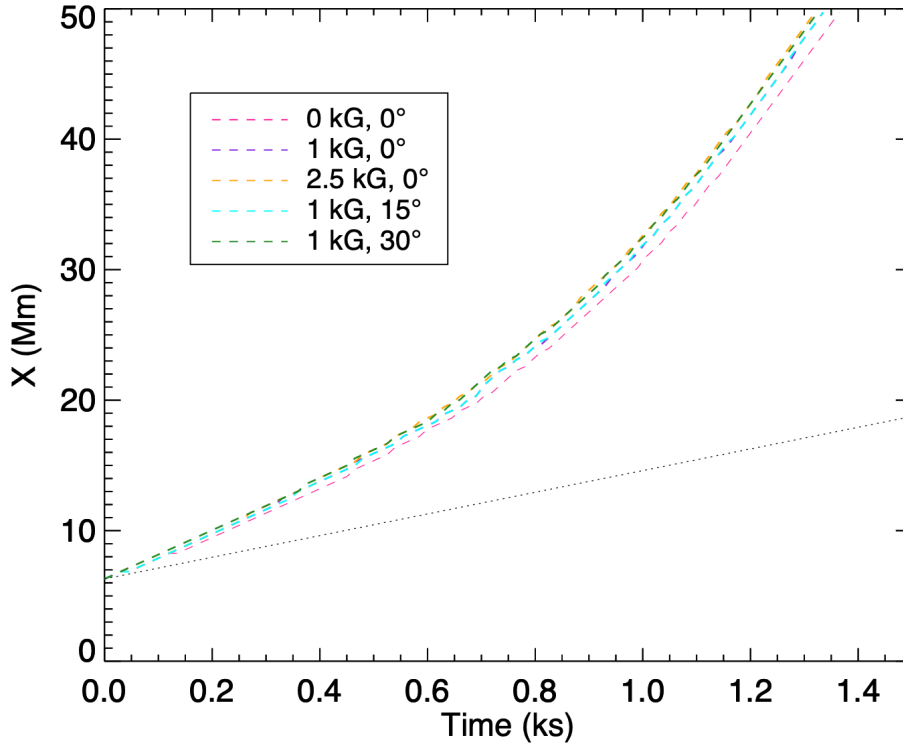Figure 4.21: Time distance plot taken from tracking the most prominent first-skip wave front from each simulation. The black dotted line shows the travel distance and time for a particle moving along the surface ($z = 0$) at the local sound speed $c_s = 8.18$ km s^{-1}.

4.7   Implications and Further Research

- The area of interest and that of most discussion was restricted to radii greater than $\sim$6 Mm from the impact site, which is outside the area proposed to be dominated by the shower glass effect. Modelling the area closer to the impact site would take either a) the implementation of an adaptive grid or b) separate higher resolution runs joined smoothly to the current simulations, which at present only accurately model greater radii. Observations from areas so close to the flare site are dominated by complex magnetic structures of the host active region, with strong signatures of flares also present. Investigation of this area is more relevant to studying the morphology of the seismic source itself. Most solar quake ripples are observed sufficiently far from the impact site and the study focuses on these areas.

- Recent research by Macrae et al. (2018); Stefan and Kosovichev (2019) has focused on an electron beam triggering mechanism hypothesis. This theory, in part, could

rely on both impulsive and gradual transfers of momentum depending at which height in the solar atmosphere the energy is imparted. Zharkova and Zharkov (2015) found that electron beams can penetrate as far as 5000 km below the photosphere. With these points in mind, a whole host of possible source excitation depths and structures can be envisaged for investigation, which extend beyond the scope of the simulations conducted here.

- The mode-conversion theories presented herein have been derived strictly in 2-D. Whilst only used as a guide to explain the results presented, further development of the theory to incorporate the third spatial dimension could allow for greater insight into the results.

- The code used only solved the linear equations of motion. Shocks have been reported to exist within the chromosphere and would require non-linear modelling. It has been reported on earlier in this study that shocks passing through the a=c layer can have a variety of energetic consequences depending on the background magnetic field structure. These structures are known to vary greatly within active regions.

- Now that we know the conditions that produce strongest signal enhancements (anisotropies), the way has been paved to implement these sources into a realistic active region atmosphere with background perturbations to mimic the solar granulation. This would enable a lower bound for the impulsive energy requirements needed to produce a signal sufficiently strong enough to be detectable with current instrumentation.

Concluding Remarks

This work comprised of conducting a host of multi-dimensional numerical simulations with the use of supercomputer facilities. Whilst the topics were varied, they all encompassed the modelling of MHD waves as they propagate through the layers of the solar atmosphere. The results were able to partially confirm/reject a newly proposed mathematical formulation for MHD shock wave smoothing through the equipartition layer; provide further evidence for the existence of resonating chromospheric cavities; and elucidate the main parameters influencing the anisotropy of solar quake surface wave fronts.

It has been well studied that as MHD waves in the linear regime travel through the layers where the sound and Alfvén speed coincide, they split their energy into two distinct branches, the slow mode and the fast mode. Simulations of non-linear MHD shock waves presented herein suggest that this splitting remains but is also accompanied by a smoothing of the slow wave, whilst the fast wave continues to propagate unhindered. This is in only partial agreement with a newly proposed mathematical formulation, which suggested both wave modes should be smoothed. A smoothing of the slow wave suggests higher frequency components are being lost or transferred to the fast wave, which has consequences for the energy budget of each mode. More energy in the fast mode has the potential to lead to enhanced fast-Alfvén conversion higher up in the solar atmosphere. Alfvén waves have been proposed to carry some of the energy required to heat the outer solar atmosphere.

Doppler measurements taken from within the solar atmosphere provide a meaningful way to measure and infer the velocities, amplitudes and energies of waves that are travelling through respective regions. These velocities are attributed mainly to upwards travelling waves, as one would expect due to their origins being internal to the Sun. However, it has become apparent that the existence of standing or downwards travelling waves must not be ignored. Physical sharp gradients in the solar atmosphere, especially at the transition region, can provide impedance to acoustic waves and act as reflection sites for them. Multiple reflection sites can create a cavity in which these waves can resonate. Simulations show that in a model solar atmosphere, potential reflection sites can be identified and given the local parameters, a cavity frequency can be inferred. The amplitudes of the waves of this frequency from within the cavity are seen to grow significantly. This suggests any measurements of wave amplitudes within these areas must take into account the resonating effect of any cavities.

Solar quakes are a recently discovered phenomena, their first appearance being noted only as far back as 1998. The new field of research opened up by the discovery of the first solar quake can be conferred to still be in its infancy. Due to their inherent connection to the impulsive stages of solar flares, a heavily active topic of solar physics research, any further understanding of solar quakes should prove invaluable. A striking feature of most solar quakes observed to date has been the anisotropy of the wave fronts observed on the solar surface through Doppler imaging. Simulations show that the ray paths of the majority of the waves responsible for these surface wave fronts pass through the equipartition layer. At this point, some energy is converted and lost to downward propagating waves, weakening the amplitudes of the waves that will eventually return to the solar surface. This effect is moderated by the 'attack angle', a prominent feature discussed throughout the works presented here. A stronger and/or more inclined magnetic field will lead to a general increase in the attack angle and more energy being lost to downward propagating waves.

However, it was found that this effect, whilst important, may often play a secondary role in the appearance of anisotropy in the surface wave fronts. Simulations show that by altering the speed of the source, constructive interference can act to amplify the signal recorded along the axis of motion. Altering the source speed can lead to signal amplitudes almost triple that of those produced by a stationary source. As the source speed continues to increase well above the local sound speed, the interference patterns are altered and a variety of anisotropies are discovered and presented. These results can hopefully prove useful in back-tracing to prove or reject theories about the triggering mechanisms for solar flares.

One of the greatest mysteries of the Sun to date has been the 'coronal heating problem', which dates back over 50 years. All three of the topics explored herein, and the simulations presented alongside them each provide, in their own way, another piece of the puzzle needed to resolve this problem. MHD shock waves can pass their energy between slow and fast modes, which carry and supply energy through different pathways; chromospheric cavities can influence the amplitudes of certain frequency acoustic waves within them; solar quake anisotropies can provide information about the flares that host them, which in turn eject matter and energy into the outer solar atmosphere. Coupled with observations and theoretical frameworks, many more numerical simulations are needed to solve not only the coronal heating problem but a myriad of other unknown solar phenomena. This work should act as but one small piece in the grand puzzle that is the working of Earth's

life-bringer, the Sun.

List of Figures

Bibliography

Afanasyev, A. N. and Nakariakov, V. M. (2015). Cut-off period for slow magnetoacoustic waves in coronal plasma structures. *Astronomy and Astrophysics*, 582:A57.

Allred, J. C., Hawley, S. L., Abbett, W. P., and Carlsson, M. (2005). Radiative Hydrodynamic Models of the Optical and Ultraviolet Emission from Solar Flares. *The Astrophysical Journal*, 630(1):573–586.

Alvarado-Gómez, J. D., Buitrago-Casas, J. C., Martínez-Oliveros, J. C., Lindsey, C., Hudson, H., and Calvo-Mozo, B. (2012). Magneto-Acoustic Energetics Study of the Seismically Active Flare of 15 February 2011. *Solar Physics*, 280(2):335–345.

Antia, H. M. and Basu, S. (1994). Nonasymptotic helioseismic inversion for solar structure. *Astronomy and Astrophysics Supplementary Series*, 107:421–444.

Arber, T. D., Longbottom, A. W., Gerrard, C. L., and Milne, A. M. (2001). A Staggered Grid, Lagrangian-Eulerian Remap Code for 3-D MHD Simulations. *Journal of Computational Physics*, 171:151–181.

Aschwanden, M. J., Brown, J. C., and Kontar, E. P. (2002). Chromospheric density and height measurements of the 2002-Feb-20 flare observed with RHESSI. In Wilson, A., editor, *Solar Variability: From Core to Outer Frontiers*, volume 1 of *ESA Special Publication*, pages 275–278.

Aulanier, G., Janvier, M., and Schmieder, B. (2012). The standard flare model in three dimensions. I. Strong-to-weak shear transition in post-flare loops. *Astronomy and Astrophysics*, 543:A110.

Aulanier, G., Török, T., Démoulin, P., and DeLuca, E. E. (2010). Formation of Torus-Unstable Flux Ropes and Electric Currents in Erupting Sigmoids. *The Astrophysical Journal*, 708(1):314–333.

Avrett, E., Tian, H., Landi, E., Curdt, W., and Wülser, J. P. (2015). Modeling the Chromosphere of a Sunspot and the Quiet Sun. *The Astrophysical Journal*, 811(2):87.

Avrett, E. H. and Loeser, R. (2008). Models of the Solar Chromosphere and Transition Region from SUMER and HRTS Observations: Formation of the Extreme-Ultraviolet Spectrum of Hydrogen, Carbon, and Oxygen. *The Astrophysical Journal Supplement Series*, 175(1):229–276.

Bahcall, J. N., Pinsonneault, M. H., Basu, S., and Christensen-Dalsgaard, J. (1997). Are Standard Solar Models Reliable? *Physical Review Letters*, 78(2):171–174.

Balmforth, N. J. and Gough, D. O. (1990). Effluent Stellar Pulsation. *The Astrophysical Journal Letters*, 362:256.

Banerjee, D., Erdélyi, R., Oliver, R., and O'Shea, E. (2007). Present and future observing trends in atmospheric magnetoseismology. *Solar Physics*, 246(1):3–29.

Banerjee, D., O'Shea, E., Goossens, M., Doyle, J. G., and Poedts, S. (2002). On the theory of MAG waves and a comparison with sunspot observations from CDS/SoHO. *Astronomy and Astrophysics*, 395:263–277.

Basu, S. (1998). Effects of errors in the solar radius on helioseismic inferences. *Monthly Notices of the Royal Astronomical Society*, 298(3):719–728.

Basu, S. and Antia, H. M. (1997). Seismic measurement of the depth of the solar convection zone. *Monthly Notices of the Royal Astronomical Society*, 287(1):189–198.

Basu, S. and Antia, H. M. (2004). Constraining Solar Abundances Using Helioseismology. *The Astrophysical Journal Letters*, 606(1):L85–L88.

Beckers, J. M. and Tallant, P. E. (1969). Chromospheric inhomogeneities in sunspot umbrae. *Solar Physics*, 7(3):351–365.

Bel, N. and Leroy, B. (1977). Analytical Study of Magnetoacoustic Gravity Waves. *Astronomy and Astrophysics*, 55:239.

Belcher, J. W. and Davis, Leverett, J. (1971). Large-amplitude Alfvén waves in the interplanetary medium, 2. *Journal of Geophysical Research*, 76(16):3534.

Bender, C. M. and Orszag, S. A. (1978). *Advanced Mathematical Methods for Scientists and Engineers*. Springer-Verlag.

Berenger, J.-P. (1994). A Perfectly Matched Layer for the Absorption of Electromagnetic Waves. *Journal of Computational Physics*, 114(2):185–200.

Berenger, J.-P. (1996). Three-Dimensional Perfectly Matched Layer for the Absorption of Electromagnetic Waves. *Journal of Computational Physics*, 127(2):363–379.

Bhattacharya, J. and Hanasoge, S. M. (2016). Strategies in Seismic Inference of Supergranular Flows on the Sun. *The Astrophysical Journal*, 826(2):105.

Bogdan, T. J. (2000). Sunspot Oscillations: A Review - (Invited Review). *Solar Physics*, 192:373–394.

Bogdan, T. J., Brown, T. M., Lites, B. W., and Thomas, J. H. (1993). The Absorption of p-Modes by Sunspots: Variations with Degree and Order. *The Astrophysical Journal*, 406:723.

Boris, J. P. (1970). A Physically Motivated Solution of the Alfveń Problem. In *NRL Memorandum Report 2167*.

Borrero, J. M. and Ichimoto, K. (2011). Magnetic structure of sunspots. *Living Reviews in Solar Physics*, 8(1):4.

Botha, G. J. J., Arber, T. D., Nakariakov, V. M., and Zhugzhda, Y. D. (2011). Chromospheric Resonances above Sunspot Umbrae. *The Astrophysical Journal*, 728(2):84.

Braun, D. C. (1995). Scattering of p-Modes by Sunspots. I. Observations. *The Astrophysical Journal*, 451:859.

123

Braun, D. C., Duvall, T. L., J., and Labonte, B. J. (1987). Acoustic Absorption by Sunspots. *The Astrophysical Journal Letters*, 319:L27.

Braun, D. C., Duvall, T. L., J., and Labonte, B. J. (1988). The Absorption of High-Degree p-Mode Oscillations in and around Sunspots. *The Astrophysical Journal*, 335:1015.

Braun, D. C., Duvall, T. L., J., Labonte, B. J., Jefferies, S. M., Harvey, J. W., and Pomerantz, M. A. (1992). Scattering of p-Modes by a Sunspot. *The Astrophysical Journal Letters*, 391:L113.

Braun, D. C. and Lindsey, C. (2000). Phase-sensitive Holography of Solar Activity. *Solar Physics*, 192:307–319.

Brown, T. M. and Morrow, C. A. (1987). Depth and Latitude Dependence of Solar Rotation. *The Astrophysical Journal Letters*, 314:L21.

Brynildsen, N., Maltby, P., Foley, C. R., Fredvik, T., and Kjeldseth-Moe, O. (2004). Oscillations in the Umbral Atmosphere. *Solar Physics*, 221(2):237–260.

Cally, P. S. (1995). Effects of Weak-to-Moderate Vertical Magnetic Fields on Solar f- and p-Modes. *The Astrophysical Journal*, 451:372.

Cally, P. S. (2000). Modelling p-Mode Interaction with a Spreading Sunspot Field. *Solar Physics*, 192:395–401.

Cally, P. S. (2001). Note on an Exact Solution for Magnetoatmospheric Waves. *The Astrophysical Journal*, 548(1):473–481.

Cally, P. S. (2005). Local magnetohelioseismology of active regions. *Monthly Notices of the Royal Astronomic Society*, 358(2):353–362.

Cally, P. S. (2006). Dispersion relations, rays and ray splitting in magnetohelioseismology. *Philosophical Transactions of the Royal Society of London Series A*, 364(1839):333–349.

Cally, P. S. (2007). What to look for in the seismology of solar active regions. *Astronomische Nachrichten*, 328(3-4):286–291.

Cally, P. S. (2008). Phase jumps in local helioseismology. *Solar Physics*, 254(2):241.

Cally, P. S. and Bogdan, T. J. (1993). Solar p-Modes in a Vertical Magnetic Field: Trapped and Damped pi -Modes. *The Astrophysical Journal*, 402:721.

Cally, P. S. and Bogdan, T. J. (1997a). Simulation of f- and p-Mode Interactions with a Stratified Magnetic Field Concentration. *The Astrophysical Journal Letters*, 486(1):L67–L70.

Cally, P. S. and Bogdan, T. J. (1997b). Simulation of f- and p-Mode Interactions with a Stratified Magnetic Field Concentration. *The Astrophysical Journal Letters*, 486(1):L67–L70.

Cally, P. S., Bogdan, T. J., and Zweibel, E. G. (1994). Umbral Oscillations in Sunspots: Absorption of p-Modes and Active Region Heating by Mode Conversion. *The Astrophysical Journal*, 437:505.

Cally, P. S., Crouch, A. D., and Braun, D. C. (2003). Probing sunspot magnetic fields with p-mode absorption and phase shift data. *The Monthly Notices of the Royal Astronomic Society*, 346(2):381–389.

Cally, P. S. and Goossens, M. (2008). Three-Dimensional MHD Wave Propagation and Conversion to Alfvén Waves near the Solar Surface. I. Direct Numerical Solution. *Solar Physics*, 251:251–265.

Cally, P. S. and Hansen, S. C. (2011). Benchmarking Fast-to-Alfvén Mode Conversion in a Cold Magnetohydrodynamic Plasma. *The Astrophysical Journal*, 738:119–+.

Cally, P. S. and Khomenko, E. (2018). Fast-to-Alfvén Mode Conversion in the Presence of Ambipolar Diffusion. *The Astrophysical Journal*, 856(1):20.

Cally, P. S., Moradi, H., and Rajaguru, S. P. (2016). p-Mode Interaction with Sunspots. *Washington DC American Geophysical Union Geophysical Monograph Series*, 216:489–502.

Cameron, R., Gizon, L., and Daiffallah, K. (2007). Slim: a code for the simulation of wave propagation through an inhomogeneous, magnetised solar atmosphere. *Astronomische Nachrichten*, 328(3-4):313–318.

Cameron, T. G. and Jackel, B. (2019). Using a numerical mhd model to improve solar wind time shifting. *Space Weather*, 17(5):662–671.

Centeno, R., Collados, M., and Trujillo Bueno, J. (2006). Spectropolarimetric Investigation of the Propagation of Magnetoacoustic Waves and Shock Formation in Sunspot Atmospheres. *The Astrophysical Journal*, 640(2):1153–1162.

Chernoff, P. R. (1980). Pointwise convergence of fourier series. *The American Mathematical Monthly*, 87(5):399–400.

Christensen-Dalsgaard, J., Dappen, W., Ajukov, S. V., Anderson, E. R., and al, e. (1996). The current state of solar modeling. *Science*, 272(5266):1286. Copyright - Copyright American Association for the Advancement of Science May 31, 1996; Last updated - 2017-10-31; CODEN - SCIEAS.

Christensen-Dalsgaard, J., Gough, D. O., and Thompson, M. J. (1991). The Depth of the Solar Convection Zone. *The Astrophysical Journal*, 378:413.

Christopoulou, E. B., Georgakilas, A. A., and Koutchmy, S. (2000). Oscillations and running waves observed in sunspots. *Astronomy and Astrophysics*, 354:305–314.

Colonius, T. (2004). Modeling artificial boundary conditions for compressible flow. *Annual Review of Fluid Mechanics*, 36(1):315–345.

Courant, R., Friedrichs, K., and Lewy, H. (1928). Über die partiellen Differenzengleichungen der mathematischen Physik. *Mathematische Annalen*, 100:32–74.

Cowling, T. G. (1945). On the Sun's general magnetic field. *Monthly Notices of the Royal Astronomical Society*, 105:166.

Crouch, A. D. and Cally, P. S. (2003). Mode Conversion of Solar p Modes in non-Vertical Magnetic Fields - i. two-Dimensional Model. *Solar Physics*, 214(2):201–226.

Crouch, A. D. and Cally, P. S. (2005). Mode Conversion of Solar p-Modes in Non-Vertical Magnetic Fields. *Solar Physics*, 227(1):1–26.

De Hoffmann, F. and Teller, E. (1950). Magneto-hydrodynamic shocks. *Physical Review*, 80:692–703.

De Pontieu, B., Erdélyi, R., and De Moortel, I. (2005). How to Channel Photospheric Oscillations into the Corona. *The Astrophysical Journal Letters*, 624(1):L61–L64.

De Pontieu, B., Erdélyi, R., and James, S. P. (2004). Solar chromospheric spicules from the leakage of photospheric oscillations and flows. *Nature*, 430(6999):536–539.

Deubner, F. L. (1975). Observations of low wavenumber nonradial eigenmodes of the sun. *Astronomy and Astrophysics*, 44(2):371–375.

Deubner, F.-L. and Gough, D. (1984). Helioseismology: Oscillations as a Diagnostic of the Solar Interior. *Annual Review of Astronomy and Astrophysics*, 22:593–619.

Dikpati, M. and Charbonneau, P. (1999). A Babcock-Leighton Flux Transport Dynamo with Solar-like Differential Rotation. *The Astrophysical Journal*, 518(1):508–520.

Domingo, V., Fleck, B., and Poland, A. I. (1995). The SOHO Mission: an Overview. *Solar Physics*, 162(1-2):1–37.

Donea, A. (2011). Seismic Transients from Flares in Solar Cycle 23. *Space Science Review*, 158(2-4):451–469.

Donea, A. C., Besliu-Ionescu, D., Cally, P. S., Lindsey, C., and Zharkova, V. V. (2006). Seismic Emission from A M9.5-Class Solar Flare. *Solar Physics*, 239(1-2):113–135.

Donea, A. C., Braun, D. C., and Lindsey, C. (1999). Seismic Images of a Solar Flare. *The Astrophysical Journal Letters*, 513(2):L143–L146.

Donea, A. C. and Lindsey, C. (2005). Seismic Emission from the Solar Flares of 2003 October 28 and 29. *The Astrophysical Journal*, 630(2):1168–1183.

D'Silva, S. (1996). Theoretical Foundations of Time-Distance Helioseismology. *The Astrophysical Journal*, 469:964.

Duvall, T. L., J., Jefferies, S. M., Harvey, J. W., and Pomerantz, M. A. (1993). Time-distance helioseismology. *Nature*, 362(6419):430–432.

Duvall, T. L., D'Silva, S., Jefferies, S. M., Harvey, J. W., and Schou, J. (1996). Downflows under sunspots detected by helioseismic tomography. *Nature*, 379(6562):235–237.

Dziembowski, W. A., Pamyatnykh, A. A., and Sienkiewicz, R. (1990). Solar model from helioseismology and the neutrino flux problem. *Monthly Notices of the Royal Astronomical Society*, 244:542–550.

Elsworth, Y., Broomhall, A.-M., Gosain, S., Roth, M., Jefferies, S. M., and Hill, F. (2015). The Importance of Long-Term Synoptic Observations and Data Sets for Solar Physics and Helioseismology. *Space Science Reviews*, 196(1-4):137–166.

Elsworth, Y., Howe, R., Isaak, G. R., McLeod, C. P., and New, R. (1990). Evidence from solar seismology against non-standard solar-core models. *Nature*, 347(6293):536–539.

Elsworth, Y., Howe, R., Isaak, G. R., McLeod, C. P., and New, R. (1991). Low-l p-mode solar eigenfrequency measurements from the Birmingham Network. *Monthly Notices of the Royal Astronomical Society*, 251:7P–9P.

Evans, J. W. and Michard, R. (1962a). Observational Study of Macroscopic Inhomogeneities in the Solar Atmosphere. I. Velocity Displacements of Fraunhofer Lines as a Function of Line Strength and Position on Disk. *The Astrophysical Journal*, 135:812.

Evans, J. W. and Michard, R. (1962b). Observational Study of Macroscopic Inhomogeneities in the Solar Atmosphere. I. Velocity Displacements of Fraunhofer Lines as a Function of Line Strength and Position on Disk. *The Astrophysical Journal*, 135:812.

Farrugia, C. J., Lavraud, B., Torbert, R. B., Argall, M., Kacem, I., Yu, W., Alm, L., Burch, J., Russell, C. T., Shuster, J., Dorelli, J., Eastwood, J. P., Ergun, R. E., Fuselier, S., Gershman, D., Giles, B. L., Khotyaintsev, Y. V., Lindqvist, P. A., Matsui, H., Marklund, G. T., Phan, T. D., Paulson, K., Pollock, C., and Strangeway, R. J. (2016). Magnetospheric Multiscale Mission observations and non-force free modeling of a flux transfer event immersed in a super-Alfvénic flow. *Geophysical Research Letters*, 43(12):6070–6077.

Fedun, V., Shelyag, S., and Erdélyi, R. (2011). Numerical Modeling of Footpoint-driven Magneto-acoustic Wave Propagation in a Localized Solar Flux Tube. *The Astrophysical Journal*, 727(1):17.

Felipe, T. (2012). Three-dimensional Numerical Simulations of Fast-to-Alfvén Conversion in Sunspots. *The Astrophsysical Journal*, 758(2):96.

Felipe, T. (2019). Origin of the chromospheric three-minute oscillations in sunspot umbrae. *Astronomy and Astrophysics*, 627:A169.

Felipe, T., Khomenko, E., and Collados, M. (2010). Magneto-acoustic Waves in Sunspots: First Results From a New Three-dimensional Nonlinear Magnetohydrodynamic Code. *The Astrophysical Journal*, 719(1):357–377.

Felipe, T., Kuckein, C., and Thaler, I. (2018). Height variation of the cutoff frequency in a sunspot umbra. *Astronomy and Astrophysics*, 617:A39.

Ferraro, C. A. and Plumpton, C. (1958). Hydromagnetic Waves in a Horizontally Stratified Atmosphere. V. *The Astrophysical Journal*, 127:459.

Finsterle, W., Jefferies, S. M., Cacciani, A. r., Rapex, P., Giebink, C., Knox, A., and Dimartino, V. (2004). Seismology of the solar atmosphere. *Solar Physics*, 220(2):317–331.

Fisher, G. H., Bercik, D. J., Welsch, B. T., and Hudson, H. S. (2012). Global Forces in Eruptive Solar Flares: The Lorentz Force Acting on the Solar Atmosphere and the Solar Interior. In *American Astronomical Society Meeting Abstracts #220*, volume 220 of *American Astronomical Society Meeting Abstracts*, page 204.40.

Fitzpatrick, R. (2014). *Plasma Physics: An Introduction*. CRC Press, Boca Raton.

Fontenla, J. M., Curdt, W., Haberreiter, M., Harder, J., and Tian, H. (2009). Semiempirical Models of the Solar Atmosphere. III. Set of Non-LTE Models for Far-Ultraviolet/Extreme-Ultraviolet Irradiance Computation. *The Astrophysical Journal*, 707(1):482–502.

Foukal, P. V. (2004). *Solar Astrophysics, 2nd, Revised Edition*. John Wiley & Sons, Ltd.

Freij, N., Dorotovič, I., Morton, R. J., Ruderman, M. S., Karlovský, V., and Erdélyi, R. (2016). On the Properties of Slow MHD Sausage Waves within Small-scale Photospheric Magnetic Structures. *The Astrophysical Journal*, 817(1):44.

Fukuda, Y., Hayakawa, T., Ichihara, E., Inoue, K., Ishihara, K., Ishino, H., Itow, Y., Kajita, T., Kameda, J., Kasuga, S., Kobayashi, K., Kobayashi, Y., Koshio, Y., Miura, M., Nakahata, M., Nakayama, S., Okada, A., Okumura, K., Sakurai, N., Shiozawa, M., Suzuki, Y., Takeuchi, Y., Totsuka, Y., Yamada, S., Earl, M., Habig, A., Kearns, E., Messier, M. D., Scholberg, K., Stone, J. L., Sulak, L. R., Walter, C. W., Goldhaber, M., Barszczak, T., Casper, D., Gajewski, W., Halverson, P. G., Hsu, J., Kropp, W. R.,

Price, L. R., Reines, F., Smy, M., Sobel, H. W., Vagins, M. R., Ganezer, K. S., Keig, W. E., Ellsworth, R. W., Tasaka, S., Flanagan, J. W., Kibayashi, A., Learned, J. G., Matsuno, S., Stenger, V. J., Takemori, D., Ishii, T., Kanzaki, J., Kobayashi, T., Mine, S., Nakamura, K., Nishikawa, K., Oyama, Y., Sakai, A., Sakuda, M., Sasaki, O., Echigo, S., Kohama, M., Suzuki, A. T., Haines, T. J., Blaufuss, E., Kim, B. K., Sanford, R., Svoboda, R., Chen, M. L., Conner, Z., Goodman, J. A., Sullivan, G. W., Hill, J., Jung, C. K., Martens, K., Mauger, C., McGrew, C., Sharkey, E., Viren, B., Yanagisawa, C., Doki, W., Miyano, K., Okazawa, H., Saji, C., Takahata, M., Nagashima, Y., Takita, M., Yamaguchi, T., Yoshida, M., Kim, S. B., Etoh, M., Fujita, K., Hasegawa, A., Hasagawa, T., Hatakeyama, S., Iwamoto, T., Koga, M., Maruyama, T., Ogawa, H., Shirai, J., Suzuki, A., Tsushima, F., Koshiba, M., Nemoto, M., Nishijima, K., Futagami, T., Hayato, Y., Kanaya, Y., Kaneyuki, K., Watanabe, Y., Kielczewska, D., Doyle, R. A., George, J. S., Stachyra, A. L., Wai, L. L., Wilkes, R. J., and Young, K. K. (1999). Constraints on Neutrino Oscillation Parameters from the Measurement of Day-Night Solar Neutrino Fluxes at Super-Kamiokande. *Physical Review Letters*, 82(9):1810–1814.

García, R. A., Turck-Chièze, S., Jiménez-Reyes, S. J., Ballot, J., Pallé, P. L., Eff-Darwich, A., Mathur, S., and Provost, J. (2007). Tracking Solar Gravity Modes: The Dynamics of the Solar Core. *Science*, 316(5831):1591.

Gelfreikh, G., Grechnev, V., Kosugi, T., and Shibasaki, K. (1999). Detection of periodic oscillations in sunspot-associated radio sources. *Solar Physics*, 185(1):177–191.

Gizon, L. and Birch, A. C. (2002). Time-Distance Helioseismology: The Forward Problem for Random Distributed Sources. *The Astrophysical Journal*, 571(2):966–986.

Gizon, L. and Birch, A. C. (2005). Local Helioseismology. *Living Reviews in Solar Physics*, 2(1):6.

Goedbloed, J. P. H. and Poedts, S. (2004). *Principles of Magnetohydrodynamics*. Cambridge University Press.

Gurman, J. B. (1987). Sunspot umbral oscillations in Mg ii k. *Solar Physics*, 108(1):61–75.

Hanasoge, S. M. (2008). Seismic Halos around Active Regions: A Magnetohydrodynamic Theory. *The Astrophysical Journal*, 680(2):1457–1466.

Hanasoge, S. M. (2011). SPARC: Seismic Propagation through Active Regions and Convection.

Hanasoge, S. M., Duvall, T. L., J., and Couvidat, S. (2007). Validation of Helioseismology through Forward Modeling: Realization Noise Subtraction and Kernels. *The Astrophysical Journal*, 664(2):1234–1243.

Hanasoge, S. M., Komatitsch, D., and Gizon, L. (2010). An absorbing boundary formulation for the stratified, linearized, ideal MHD equations based on an unsplit, convolutional perfectly matched layer. *Astronomy and Astrophysics*, 522:A87.

Hanasoge, S. M., Larsen, R. M., Duvall, T. L., J., De Rosa, M. L., Hurlburt, N. E., Schou, J., Roth, M., Christensen-Dalsgaard, J., and Lele, S. K. (2006). Computational Acoustics in Spherical Geometry: Steps toward Validating Helioseismology. *The Astrophysical Journal*, 648(2):1268–1275.

Hansen, S. and Cally, P. (2009). An exact test of generalised ray theory in local helioseismology. *Solar Physics*, 255:193–202.

Hansen, S. C. and Cally, P. S. (2012). Benchmarking Fast-to-Alfvén Mode Conversion in a Cold MHD Plasma. II. How to Get Alfvén Waves through the Solar Transition Region. *The Astrophysical Journal*, 751(1):31.

Hansen, S. C., Cally, P. S., and Donea, A.-C. (2015). On mode conversion, reflection, and transmission of magnetoacoustic waves from above in an isothermal stratified atmosphere. *Monthly Notices of the Royal Astronomical Society*, 456(2):1826–1836.

Hathaway, D. H., Gilman, P. A., Harvey, J. W., Hill, F., Howard, R. F., Jones, H. P., Kasher, J. C., Leibacher, J. W., Pintar, J. A., and Simon, G. W. (1996). GONG Observations of Solar Surface Flows. *Science*, 272(5266):1306–1309.

Heggland, L., Hansteen, V. H., De Pontieu, B., and Carlsson, M. (2011). Wave Propagation and Jet Formation in the Chromosphere. *The Astrophysical Journal*, 743(2):142.

Hill, F., Stark, P. B., Stebbins, R. T., Anderson, E. R., Antia, H. M., Brown, T. M., Duvall, T. L., J., Haber, D. A., Harvey, J. W., Hathaway, D. H., Howe, R., Hubbard, R. P., Jones, H. P., Kennedy, J. R., Korzennik, S. G., Kosovichev, A. G., Leibacher, J. W., Libbrecht, K. G., Pintar, J. A., Rhodes, E. J., J., Schou, J., Thompson, M. J., Tomczyk, S., Toner,

C. G., Toussaint, R., and Williams, W. E. (1996). The Solar Acoustic Spectrum and Eigenmode Parameters. *Science*, 272(5266):1292–1295.

Hood, A. W. (2010). *Coronal Heating*, volume 793, page 109. Berlin Springer Verlag.

Horace, L. (1909). On the theory of waves propagated vertically in the atmosphere. *Proceedings of the London Mathematical Society*, s2-7(1):122–141.

Howe, R., Christensen-Dalsgaard, J., Hill, F., Komm, R. W., Larsen, R. M., Schou, J., Thompson, M. J., and Toomre, J. (2000). Dynamic Variations at the Base of the Solar Convection Zone. *Science*, 287(5462):2456–2460.

Hurford, G. J., Schwartz, R. A., Krucker, S., Lin, R. P., Smith, D. M., and Vilmer, N. (2003). First Gamma-Ray Images of a Solar Flare. *The Astrophysical Journal Letters*, 595(2):L77–L80.

Ionescu, D. (2006). *Seismic Emissions from Solar Flares*. PhD thesis, Monash University.

Jackson, J. D. (1975). *Classical electrodynamics*. John Wiley & Sons.

Jacoutot, L., Kosovichev, A. G., Wray, A., and Mansour, N. N. (2008). Realistic Numerical Simulations of Solar Convection and Oscillations in Magnetic Regions. *The Astrophysical Journal Letters*, 684(1):L51.

Jain, R., Tripathy, S. C., Watson, F. T., Fletcher, L., Jain, K., and Hill, F. (2012). Variation of solar oscillation frequencies in solar cycle 23 and their relation to sunspot area and number. *Astronomy and Astrophysics*, 545:A73.

Janvier, M. (2017). Three-dimensional magnetic reconnection and its application to solar flares. *Journal of Plasma Physics*, 83(1):535830101.

Jefferies, S. M., McIntosh, S. W., Armstrong, J. D., Bogdan, T. J., Cacciani, A. r., and Fleck, B. (2006). Magnetoacoustic Portals and the Basal Heating of the Solar Chromosphere. *The Astrophysical Journal Letters*, 648(2):L151–L155.

Jensen, J. M. (2003). Time-distance: what does it tell us? In Sawaya-Lacoste, H., editor, *GONG+ 2002. Local and Global Helioseismology: the Present and Future*, volume 517 of *ESA Special Publication*, pages 61–70.

Jess, D. B., Morton, R. J., Verth, G., Fedun, V., Grant, S. D. T., and Giagkiozis, I. (2015). Multiwavelength Studies of MHD Waves in the Solar Chromosphere. An Overview of Recent Results. *Space Science Reviews*, 190(1-4):103–161.

Jess, D. B., Snow, B., Houston, S. J., Botha, G. J. J., Fleck, B., Krishna Prasad, S., Asensio Ramos, A., Morton, R. J., Keys, P. H., Jafarzadeh, S., Stangalini, M., Grant, S. D. T., and Christian, D. J. (2019). A chromospheric resonance cavity in a sunspot mapped with seismology. *Nature Astronomy*, 4:220–227.

Ji, H., Yamada, M., Hsu, S., and Kulsrud, R. (1998). Experimental Test of the Sweet-Parker Model of Magnetic Reconnection. *Physical Review Letters*, 80(15):3256–3259.

Jiménez, A., García, R. A., and Pallé, P. L. (2011). The Acoustic Cutoff Frequency of the Sun and the Solar Magnetic Activity Cycle. *The Astrophysical Journal*, 743(2):99.

Jurčák, J. (2011). Azimuthal variations of magnetic field strength and inclination on penumbral boundaries. *Astronomy and Astrophysics*, 531:A118.

Kalkofen, W., Rossi, P., Bodo, G., and Massaglia, S. (1994). Propagation of acoustic waves in a stratified atmosphere, 1. *Astronomy & Astrophysics*, 284.

Khomenko, E. (2015). Beyond MHD: modeling and observation of partially ionized solar plasma processes. In *Highlights of Spanish Astrophysics VIII*, pages 677–688.

Khomenko, E. and Cally, P. S. (2012). Numerical Simulations of Conversion to Alfvén Waves in Sunspots. *The Astrophysical Journal*, 746(1):68.

Khomenko, E. and Collados, M. (2008). Magnetohydrostatic Sunspot Models from Deep Subphotospheric to Chromospheric Layers. *The Astrophysical Journal*, 689(2):1379–1387.

Khomenko, E. and Collados, M. (2015). Oscillations and Waves in Sunspots. *Living Reviews in Solar Physics*, 12(1):6.

Kinsler, L., Kinsler, L., Frey, A., Coppens, A., and Sanders, J. (2000). *Fundamentals of Acoustics*. Wiley.

Kliem, B., Su, Y. N., van Ballegooijen, A. A., and DeLuca, E. E. (2013). Magnetohydrodynamic Modeling of the Solar Eruption on 2010 April 8. *The Astrophysical Journal*, 779(2):129.

Kolobov, D. Y., Chelpanov, A. A., and Kobanov, N. I. (2016). Peculiarity of the Oscillation Stratification in Sunspot Penumbrae. *Solar Physics*, 291(11):3339–3347.

Komm, R., Corbard, T., Durney, B. R., González Hernández, I., Hill, F., Howe, R., and Toner, C. (2004). Solar Subsurface Fluid Dynamics Descriptors Derived from Global Oscillation Network Group and Michelson Doppler Imager Data. *The Astrophysical Journal*, 605(1):554–567.

Kosovichev, A. G. (2006). Properties of Flares-Generated Seismic Waves on the Sun. *Solar Physics*, 238(1):1–11.

Kosovichev, A. G. (2007). The Cause of Photospheric and Helioseismic Responses to Solar Flares: High-Energy Electrons or Protons? *The Astrophysical Journal Letters*, 670(1):L65–L68.

Kosovichev, A. G. (2009). Solar Oscillations. In Guzik, J. A. and Bradley, P. A., editors, *American Institute of Physics Conference Series*, volume 1170 of *American Institute of Physics Conference Series*, pages 547–559.

Kosovichev, A. G. (2015). *Sunquakes: Helioseismic response to solar flares*, pages 306–322. Cambridge University Press.

Kosovichev, A. G., Duvall, T. L. _Jr., J., and Scherrer, P. H. (2000). Time-Distance Inversion Methods and Results - (Invited Review). *Solar Physics*, 192:159–176.

Kosovichev, A. G. and Zharkova, V. V. (1998). X-ray flare sparks quake inside Sun. *Nature*, 393(6683):317–318.

Kráskiewicz, J., Murawski, K., and Musielak, Z. E. (2019). Cutoff periods of magnetoacoustic waves in the solar atmosphere. *Astronomy and Astrophysics*, 623:A62.

Kumar, B., Tripathy, S. C., Jain, R., and Deshpand e, M. R. (2000). On the power and frequency of p-modes in sunspots. *Bulletin of the Astronomical Society of India*, 28:93.

Kuperus, M. (1969). The Heating of the Solar Corona. *Space Science Reviews*, 9(5):713–739.

Leighton, R. B., Noyes, R. W., and Simon, G. W. (1962). Velocity Fields in the Solar Atmosphere. I. Preliminary Report. *The Astrophysical Journal*, 135:474.

Lindsey, C. and Braun, D. C. (1990). Helioseismic Imaging of Sunspots at Their Antipodes. *Solar Physics*, 126(1):101–115.

Lindsey, C. and Braun, D. C. (2000). Basic Principles of Solar Acoustic Holography - (Invited Review). *Solar Physics*, 192:261–284.

Lindsey, C. and Braun, D. C. (2004). The Acoustic Showerglass and Diagnostics of Active Region Subphotospheres. In *American Astronomical Society Meeting Abstracts #204*, volume 204 of *American Astronomical Society Meeting Abstracts*, page 53.10.

Lindsey, C. and Braun, D. C. (2005a). The Acoustic Showerglass. I. Seismic Diagnostics of Photospheric Magnetic Fields. *The Astrophysical Journal*, 620(2):1107–1117.

Lindsey, C. and Braun, D. C. (2005b). The Acoustic Showerglass. II. Imaging Active Region Subphotospheres. *The Astrophysical Journal*, 620(2):1118–1131.

Lindsey, C. and Donea, A. C. (2008). Mechanics of Seismic Emission from Solar Flares. *Solar Physics*, 251(1-2):627–639.

Lites, B. W. and Skumanich, A. (1982). A model of a sunspot chromosphere based on OSO 8 observations. *The Astrophysical Journal Supplement Series*, 49:293–315.

Livingston, W. (2002). Sunspots Observed to Physically Weaken in 2000-2001. *Solar Physics*, 207(1):41–45.

Löhner-Böttcher, J. and Bello González, N. (2015). Signatures of running penumbral waves in sunspot photospheres. *Astronomy and Astrophysics*, 580:A53.

Macrae, C., Zharkov, S., Zharkova, V., Druett, M., Matthews, S., and Kawate, T. (2018). Lost and found sunquake in the 6 September 2011 flare caused by beam electrons. *Astronomy and Astrophysics*, 619:A65.

Maltby, P., Avrett, E. H., Carlsson, M., Kjeldseth-Moe, O., Kurucz, R. L., and Loeser, R. (1986). A New Sunspot Umbral Model and Its Variation with the Solar Cycle. *The Astrophysical Journal*, 306:284.

Martínez-Oliveros, J. C., Moradi, H., and Donea, A. C. (2008). Seismic Emissions from a Highly Impulsive M6.7 Solar Flare. *Solar Physics*, 251(1-2):613–626.

Maurya, R. A. (2013). Chromospheric Doppler Velocity Oscillations in a Sunspot. In Jain, K., Tripathy, S. C., Hill, F., Leibacher, J. W., and Pevtsov, A. A., editors, *Fifty Years of Seismology of the Sun and Stars*, volume 478 of *Astronomical Society of the Pacific Conference Series*, page 339.

McDonald, A. B., Ahmad, Q. R., Allen, R. C., Andersen, T. C., Anglin, J. D., Barton, J. C., Beier, E. W., Bercovitch, M., Bigu, J., Biller, S. D., Black, R. A., Blevis, I., Boardman, R. J., Boger, J., Bonvin, E., Boulay, M. G., Bowler, M. G., Bowles, T. J., Brice, S. J., Browne, M. C., Bullard, T. V., Bühler, G., Cameron, J., Chan, Y. D., Chen, H. H., Chen, M., Chen, X., Cleveland, B. T., Clifford, E. T. H., Cowan, J. H. M., Cowen, D. F., Cox, G. A., Dai, X., Dalnoki-Veress, F., Davidson, W. F., Doe, P. J., Doucas, G., Dragowsky, M. R., Duba, C. A., Duncan, F. A., Dunford, M., Dunmore, J. A., Earle, E. D., Elliott, S. R., Evans, H. C., Ewan, G. T., Farine, J., Fergani, H., Ferraris, A. P., Ford, R. J., Formaggio, J. A., Fowler, M. M., Frame, K., Frank, E. D., Frati, W., Gagnon, N., Germani, J. V., Gil, S., Graham, K., Grant, D. R., Hahn, R. L., Hallin, A. L., Hallman, E. D., Hamer, A. S., Hamian, A. A., Handler, W. B., Haq, R. U., Hargrove, C. K., Harvey, P. J., Hazama, R., Heeger, K. M., Heintzelman, W. J., Heise, J., Helmer, R. L., Hepburn, J. D., Heron, H., Hewett, J., Hime, A., Howe, M., Hykawy, J. G., Isaac, M. C. P., Jagam, P., Jelley, N. A., Jillings, C., Jonkmans, G., Kazkaz, K., Keener, P. T., Klein, J. R., Knox, A. B., Komar, R. J., Kouzes, R., Kutter, T., Kyba, C. C. M., Law, J., Lawson, I. T., Lay, M., Lee, H. W., Lesko, K. T., Leslie, J. R., Levine, I., Locke, W., Luoma, S., Lyon, J., Majerus, S., Mak, H. B., Maneira, J., Manor, J., Marino, A. D., McCauley, N., McDonald, D. S., McFarlane, K., McGregor, G., Meijer Drees, R., Mifflin, C., Miller, G. G., Milton, G., Moffat, B. A., Moorhead, M., Nally, C. W., Neubauer, M. S., Newcomer, F. M., Ng, H. S., Noble, A. J., Norman, E. B., Novikov, V. M., O'Neill, M., Okada, C. E., Ollerhead, R. W., Omori, M., Orrell, J. L., Oser, S. M., Poon, A. W. P., Radcliffe, T. J., Roberge, A., Robertson, B. C., Robertson, R. G. H., Rosendahl, S. S. E., Rowley, J. K., Rusu, V. L., Saettler, E., Schaffer, K. K., Schwendener, M. H., Schülke, A., Seifert, H., Shatkay, M., Simpson, J. J., Sims, C. J., Sinclair, D., Skensved, P., Smith, A. R., Smith, M. W. E., Spreitzer, T., Starinsky, N., Steiger, T. D., Stokstad, R. G., Stonehill, L. C., Storey, R. S., Sur, B., Tafirout, R., Tagg, N., Tanner, N. W., Taplin, R. K., Thorman, M., Thornewell, P. M., Trent, P. T., Tserkovnyak, Y. I., van Berg, R., van de Water, R. G., Virtue, C. J., Waltham, C. E., Wang, J. X., Wark, D. L., West, N., Wilhelmy, J. B., Wilkerson, J. F., Wilson, J. R., Wittich, P., Wouters, J. M., and Yeh,

M. (2002). Direct Evidence for Neutrino Flavor Transformation from Neutral-Current Interactions in SNO. In Elias, V., Epp, R., and Myers, R. C., editors, *Theoretical Physics: MRST 2002*, volume 646 of *American Institute of Physics Conference Series*, pages 43–58.

McLellan, Alden, I. and Winterberg, F. (1968). Magneto-Gravity Waves and the Heating of the Solar Corona. *Solar Physics*, 4(4):401–408.

Melrose, D. B. (1977). Mode coupling in the solar corona. III. Alfvén and magnetoacoustic waves. *Australian Journal of Physics*, 30:495–507.

Mishonov, T. M., Stoev, M. V., and Maneva, Y. G. (2007). On the origin of solar wind. Alfvén waves induced jump of coronal temperature. *European Physical Journal D*, 44(3):533–536.

Moore, R. L. (1981). Dynamic phenomena in sunspots. In Cram, L. E. and Thomas, J. H., editors, *The Physics of Sunspots*, pages 259–311.

Moradi, H. and Cally, P. S. (2008). Three-dimensional ray propagation in a toy sunspot. In *Journal of Physics Conference Series*, volume 118 of *Journal of Physics Conference Series*, page 012037.

Moradi, H. and Cally, P. S. (2013). Helioseismic Implications of Mode Conversion. In Jain, K., Tripathy, S. C., Hill, F., Leibacher, J. W., and Pevtsov, A. A., editors, *Fifty Years of Seismology of the Sun and Stars*, volume 478 of *Astronomical Society of the Pacific Conference Series*, page 263.

Moradi, H. and Cally, P. S. (2014). Sensitivity of Helioseismic Travel Times to the Imposition of a Lorentz Force Limiter in Computational Helioseismology. *The Astrophysical Journal Letters*, 782(2):L26.

Moradi, H., Donea, A., Besliu-Ionescu, D., Cally, P., Lindsey, C., and Leka, K. (2006). *Magnetohelioseismic Analysis of AR10720 Using Helioseismic Holography*, volume 354 of *Astronomical Society of the Pacific Conference Series*, page 168. Astronomical Society of the Pacific Conference Series.

Moradi, H., Donea, A. C., Lindsey, C., Besliu-Ionescu, D., and Cally, P. S. (2007). Helioseismic analysis of the solar flare-induced sunquake of 2005 January 15. *Monthly Notices Royal Astronomical Society*, 374(3):1155–1163.

Murawski, K. (2002). *Analytical and Numerical Methods for Wave Propagation in Fluid Media*. Series on stability, vibration, and control of systems. World Scientific.

Murawski, K. (2011). Numerical solutions of magnetohydrodynamic equations. *Bulletin of the Polish Academy of Sciences. Technical Sciences*, 59.

Musielak, Z. E., Musielak, D. E., and Mobashi, H. (2006). Method to determine cutoff frequencies for acoustic waves propagating in nonisothermal media. *Physical Review*, 73(3):036612.

Nagashima, K., Sekii, T., Kosovichev, A. G., Shibahashi, H., Tsuneta, S., Ichimoto, K., Katsukawa, Y., Lites, B., Nagata, S., Shimizu, T., Shine, R. A., Suematsu, Y., Tarbell, T. D., and Title, A. M. (2007). Observations of Sunspot Oscillations in G Band and CaII H Line with Solar Optical Telescope on Hinode. *Publications of the Astronomical Society of Japan*, 59:S631.

Nandy, D. and Choudhuri, A. R. (2002). Explaining the Latitudinal Distribution of Sunspots with Deep Meridional Flow. *Science*, 296(5573):1671–1673.

Narain, U. and Ulmschneider, P. (1996). Chromospheric and Coronal Heating Mechanisms II. *Space Science Reviews*, 75(3-4):453–509.

Newington, M. E. and Cally, P. S. (2010). Reflection and conversion of magnetogravity waves in the solar chromosphere: windows to the upper atmosphere. *Monthly Notices of the Royal Astronomical Society*, 402(1):386–394.

Núñez, M. (2019). Smoothing of shocks in wave conversion of magnetosonic waves. *Europhysics Letters*, 125:44002.

Ofman, L., Romoli, M., Poletto, G., Noci, G., and Kohl, J. L. (1997). Ultraviolet Coronagraph Spectrometer Observations of Density Fluctuations in the Solar Wind. *The Astrophysical Journal Letters*, 491(2):L111–L114.

Orta, J. A., Huerta, M. A., and Boynton, G. C. (2003). Magnetohydrodynamic Shock Heating of the Solar Corona. *The Astrophysical Journal*, 596(1):646–655.

O'Shea, E., Banerjee, D., Doyle, J. G., Fleck, B., and Murtagh, F. (2001). Active region oscillations. *Astronomy and Astrophysics*, 368:1095–1107.

Parker, E. N. (1957). Sweet's Mechanism for Merging Magnetic Fields in Conducting Fluids. *Journal of Geophysical Research*, 62(4):509–520.

Pennicott, J. D. and Cally, P. S. (2019). Smoothing of MHD shocks in mode conversion. *The Astrophysical Journal Letters*, 881(1):L21.

Pesnell, W. D., Thompson, B. J., and Chamberlin, P. C. (2012). The Solar Dynamics Observatory (SDO). *Solar Physics*, 275(1-2):3–15.

Prasad, A., Bhattacharyya, R., and Kumar, S. (2017). Magnetohydrodynamic Modeling of Solar Coronal Dynamics with an Initial Non-force-free Magnetic Field. *The Astrophysical Journal*, 840(1):37.

Priest, E. (1984). *Solar Magnetohydrodynamics*. Geophysics and Astrophysics Monographs. Springer Netherlands.

Przybylski, D., Shelyag, S., and Cally, P. S. (2015). Spectropolarimetrically Accurate Magnetohydrostatic Sunspot Model for Forward Modeling in Helioseismology. *The Astrophysical Journal*, 807(1):20.

Rempel, M. (2012). Numerical models of sunspot formation and fine structure. *Philosophical Transactions of the Royal Society of London Series A*, 370(1970):3114–3128.

Rempel, M. and Schlichenmaier, R. (2011). Sunspot modeling: From simplified models to radiative mhd simulations. *Living Reviews in Solar Physics*, 8(1):3.

Rempel, M., Schüssler, M., and Knölker, M. (2009). Radiative Magnetohydrodynamic Simulation of Sunspot Structure. *The Astrophysical Journal*, 691(1):640–649.

Rendtel, J., Staude, J., and Curdt, W. (2003). Observations of oscillations in the transition region above sunspots. *Astronomy and Astrophysics*, 410:315–321.

Reznikova, V. E. and Shibasaki, K. (2012). Spatial Structure of Sunspot Oscillations Observed with SDO/AIA. *The Astrophysical Journal*, 756(1):35.

Rhodes, E. J., J., Ulrich, R. K., and Simon, G. W. (1977). Observations of nonradial p-mode oscillations on the sun. *The Astrophysical Journal*, 218:901–919.

Richard, O., Dziembowski, W. A., Sienkiewicz, R., and Goode, P. R. (1998). On the accuracy of helioseismic determination of solar helium abundance. *Astronomy and Astrophysics*, 338:756–760.

Roberts, B. (1983). Wave propagation in intense flux tubes. *Solar Physics*, 87(1):77–93.

Roberts, B. (2004). MHD Waves in the Solar Atmosphere. In Lacoste, H., editor, *SOHO 13 Waves, Oscillations and Small-Scale Transients Events in the Solar Atmosphere: Joint View from SOHO and TRACE*, volume 547 of *ESA Special Publication*, page 1.

Roberts, B. (2006). Slow magnetohydrodynamic waves in the solar atmosphere. *Philosophical Transactions of the Royal Society of London Series A*, 364(1839):447–460.

Roddier, F. (1975). Principle of production of an acoustic hologram of the solar surface. *Academie des Sciences Paris Comptes Rendus Serie B Sciences Physiques*, 281(4):93–95.

Russell, A. J. B., Simões, P. J. A., and Fletcher, L. (2015). A unified view of coronal loop contraction and oscillation in flares. *Astronomy and Astrophysics*, 581:A8.

Santamaria, I. C., Khomenko, E., and Collados, M. (2015). Magnetohydrodynamic wave propagation from the subphotosphere to the corona in an arcade-shaped magnetic field with a null point. *Astronomy and Astrophysics*, 577:A70.

Santos, A. R. G., Cunha, M. S., Avelino, P. P., Chaplin, W. J., and Campante, T. L. (2017). A thorough analysis of the short- and mid-term activity-related variations in the solar acoustic frequencies. *Monthly Notices of the Royal Astronomic Society*, 464(4):4408–4414.

Schmelz, J. T., Holman, G. D., Brosius, J. W., and Willson, R. F. (1994). Coronal Magnetic Structures Observing Campaign. III. Coronal Plasma and Magnetic Field Diagnostics Derived from Multiwaveband Active Region Observations. *The Astrophysical Journal*, 434:786.

Schmitz, F. and Fleck, B. (1998). On wave equations and cut-off frequencies of plane atmospheres. *Astronomy and Astrophysics*, 337:487–494.

Schmitz, F. and Fleck, B. (2003). Towards an explanation of features in the diagnostic diagram of a model atmosphere. I. Linear wave equations with convenient invariants. *Astronomy and Astrophysics*, 399:723–730.

Schuessler, M. (1981). The solar torsional oscillation and dynamo models of the solar cycle. *Astronomy and Astrophysics*, 94(2):L17.

Schunker, H., Braun, D. C., Cally, P. S., and Lindsey, C. (2005). The Local Helioseismology of Inclined Magnetic Fields and the Showerglass Effect. *The Astrophysical Journal Letters*, 621(2):L149–L152.

Schunker, H. and Cally, P. S. (2006). Magnetic field inclination and atmospheric oscillations above solar active regions. *Monthly Notices of the Royal Astronomical Society*, 372(2):551–564.

Serenelli, A. M. and Basu, S. (2010). Determining the Initial Helium Abundance of the Sun. *The Astrophysical Journal*, 719(1):865–872.

Sharykin, I. N. and Kosovichev, A. G. (2019). Sunquakes of Solar Cycle 24. *arXiv e-prints*, page arXiv:1911.04197.

Sharykin, I. N., Kosovichev, A. G., Sadykov, V. M., Zimovets, I. V., and Myshyakov, I. I. (2017). Investigation of Relationship between High-energy X-Ray Sources and Photospheric and Helioseismic Impacts of X1.8 Solar Flare of 2012 October 23. *The Astrophysical Journal*, 843(1):67.

Shelyag, S., Zharkov, S., Fedun, V., Erdélyi, R., and Thompson, M. J. (2009). Acoustic wave propagation in the solar sub-photosphere with localised magnetic field concentration: effect of magnetic tension. *Astronomy and Astrophysics*, 501(2):735–743.

Snow, B., Botha, G. J. J., and Régnier, S. (2015). Chromospheric seismology above sunspot umbrae. *Astronomy and Astrophysics*, 580:A107.

Snow, B. and Hillier, A. (2020). Mode conversion of two-fluid shocks in a partially-ionised, isothermal, stratified atmosphere. *arXiv e-prints*, page arXiv:2004.02550.

Solanki, S. K. (2003). Sunspots: An overview. *The Astronomy and Astrophysics Review*, 11(2-3):153–286.

Soler, R., Carbonell, M., Ballester, J. L., and Terradas, J. (2013). Alfvén Waves in a Partially Ionized Two-fluid Plasma. *The Astrophysical Journal*, 767(2):171.

Somov, B. V. (2010). CONFERENCES AND SYMPOSIA Magnetic reconnection in solar flares. *Physics Uspekhi*, 53(9):954–958.

Spruit, H. C. (1991). Absorption of p-mode waves by magnetic fields. In Gough, D. and Toomre, J., editors, *Challenges to Theories of the Structure of Moderate-Mass Stars*, pages 121–134, Berlin, Heidelberg. Springer Berlin Heidelberg.

Spruit, H. C. and Bogdan, T. J. (1992). The Conversion of p-Modes to Slow Modes and the Absorption of Acoustic Waves by Sunspots. *The Astrophysical Journal Letters*, 391:L109.

Staude, J. (1981). A unified working model for the atmospheric structure of large sunspot umbrae. *Astronomy and Astrophysics*, 100(2):284–290.

Staude, J. (1991). Solar Research at Potsdam: Papers on the Structure and Dynamics of Sunspots. *Reviews in Modern Astronomy*, 4:69–89.

Stefan, J. T. and Kosovichev, A. G. (2019). Estimation of Key Sunquake Parameters through Hydrodynamic Modeling and Cross-Correlation Analysis. *arXiv e-prints*, page arXiv:1911.06839.

Stein, R. F. and Leibacher, J. (1974). Waves in the solar atmosphere. *Annual Review of Astronomy and Astrophysics*, 12:407–435.

Sudol, J. J. and Harvey, J. W. (2005). Longitudinal Magnetic Field Changes Accompanying Solar Flares. *The Astrophysical Journal*, 635(1):647–658.

Sweet, P. A. (1950). The effect of turbulence on a magnetic field. *Monthly Notices of the Royal Astronomical Society*, 110:69–83.

Sych, R. (2016). MHD Wave in Sunspots. *Washington DC American Geophysical Union Geophysical Monograph Series*, 216:467–487.

Sych, R. and Nakariakov, V. M. (2014). Wave dynamics in a sunspot umbra. *Astronomy and Astrophysics*, 569:A72.

Sych, R., Nakariakov, V. M., Karlicky, M., and Anfinogentov, S. (2009). Relationship between wave processes in sunspots and quasi-periodic pulsations in active region flares. *Astronomy and Astrophysics*, 505(2):791–799.

Thomas, J. H. (1982). The local dispersion relation for magneto-atmospheric waves. *The Astrophysical Journal*, 262:760–767.

Thomas, J. H., Cram, L. E., and Nye, A. H. (1984). Dynamical phenomena in sunspots. I - Observing procedures and oscillatory phenomena. *The Astrophysical Journal*, 285:368–385.

Thomas, J. H., Lites, B. W., and Bogdan, T. J. (1997). Velocity and Magnetic Field Fluctuations in the Photosphere of a Sunspot. In *AAS/Solar Physics Division Meeting #28*, AAS/Solar Physics Division Meeting, page 02.36.

Thompson, M. J., Christensen-Dalsgaard, J., Miesch, M. S., and Toomre, J. (2003). The Internal Rotation of the Sun. *Annual Review of Astronomy and Astrophysics*, 41:599–643.

Tomczyk, S., McIntosh, S. W., Keil, S. L., Judge, P. G., Schad, T., Seeley, D. H., and Edmondson, J. (2007). Alfvén Waves in the Solar Corona. *Science*, 317(5842):1192.

Tóth, G. (1996). *A General Code for Modeling MHD Flows on Parallel Computers: Versatile Advection Code*, pages 471–472. Springer Netherlands, Dordrecht.

Tracy, E. R., Kaufman, A. N., and Brizard, A. J. (2003). Ray-based methods in multidimensional linear wave conversion. *Physics of Plasmas*, 10:2147–2154.

Tritschler, A., Schmidt, W., Langhans, K., and Kentischer, T. (2002). High-resolution solar spectroscopy with TESOS - Upgrade from a double to a triple system. *Solar Physics*, 211(1):17–29.

Tsap, Y. T., Stepanov, A. V., and Kopylova, Y. G. (2011). Energy Flux of Alfvén Waves in Weakly Ionized Plasma and Coronal Heating of the Sun. *Solar Physics*, 270(1):205–211.

Tsuneta, S., Ichimoto, K., Katsukawa, Y., Nagata, S., Otsubo, M., Shimizu, T., Suematsu, Y., Nakagiri, M., Noguchi, M., Tarbell, T., Title, A., Shine, R., Rosenberg, W., Hoffmann, C., Jurcevich, B., Kushner, G., Levay, M., Lites, B., Elmore, D., Matsushita, T., Kawaguchi, N., Saito, H., Mikami, I., Hill, L. D., and Owens, J. K. (2008).

The Solar Optical Telescope for the Hinode Mission: An Overview. *Solar Physics*, 249(2):167–196.

Turck-Chièze, S., Basu, S., Brun, A. S., Christensen-Dalsgaard, J., Eff-Darwich, A., Lopes, I., Pérez Hernández, F., Berthomieu, G., Provost, J., Ulrich, R. K., Baudin, F., Boumier, P., Charra, J., Gabriel, A. H., Garcia, R. A., Grec, G., Renaud, C., Robillot, J. M., and Roca Cortés, T. (1997). First View of the Solar Core from GOLF Acoustic Modes. *Solar Physics*, 175(2):247–265.

Uchida, Y. and Sakurai, T. (1975). Oscillations in sunspot umbrae due to trapped Alfvén waves excited by overstability. *Astronomical Society of Japan*, 27(2):259–274.

Ulrich, R. K. and Rhodes, E. J., J. (1977). The sensitivity of nonradial p mode eigenfrequencies to solar envelope structure. *The Astrophysical Journal*, 218:521–529.

Vecchio, A., Cauzzi, G., and Reardon, K. P. (2008). The solar chromosphere at high resolution with ibis. *Astronomy and Astrophysics*, 494(1):269–286.

Vernazza, J. E., Avrett, E. H., and Loeser, R. (1981). Structure of the solar chromosphere. III. Models of the EUV brightness components of the quiet sun. *The Astrophysical Journal Supplement Series*, 45:635–725.

Verwichte, E., Foullon, C., and Nakariakov, V. M. (2006). Fast magnetoacoustic waves in curved coronal loops. II. Tunneling modes. *Astronomy and Astrophysics*, 449(2):769–779.

Verwichte, E., Marsh, M., Foullon, C., Van Doorsselaere, T., De Moortel, I., Hood, A. W., and Nakariakov, V. M. (2010). Periodic Spectral Line Asymmetries in Solar Coronal Structures from Slow Magnetoacoustic Waves. *The Astrophysical Journal Letters*, 724(2):L194–L198.

Vitense, E. (1953). Die Wasserstoffkonvektionszone der Sonne. Mit 11 Textabbildungen. *Zeitschrift für Astrophysik*, 32:135.

Vorontsov, S. V., Baturin, V. A., and Pamiatnykh, A. A. (1991). Seismological measurement of solar helium abundance. *Nature*, 349(6304):49–51.

Vranjes, J., Poedts, S., Pandey, B. P., and de Pontieu, B. (2008). Energy flux of Alfvén waves in weakly ionized plasma. *Astronomy and Astrophysics*, 478(2):553–558.

Wang, H., Ji, H., Schmahl, E. J., Qiu, J., Liu, C., and Deng, N. (2002). Sudden Disappearance of a Small Sunspot Associated with the 2002 February 20 M2.4 Flare. *The Astrophysical Journal Letters*, 580(2):L177–L180.

Weinberg, S. (1962). Eikonal Method in Magnetohydrodynamics. *Physical Review*, 126(6):1899–1909.

Yamada, M. (2007). Progress in understanding magnetic reconnection in laboratory and space astrophysical plasmas. *Physics of Plasmas*, 14(5):058102–058102.

Yamada, M., Kulsrud, R., and Ji, H. (2010). Magnetic reconnection. *Reviews of Modern Physics*, 82(1):603–664.

Yu, C. P. (1965). Magneto-atmospheric waves in a horizontally stratified conducting medium. *The Physics of Fluids*, 8(4):650–656.

Yuan, D., Sych, R., Reznikova, V. E., and Nakariakov, V. M. (2014). Multi-height observations of magnetoacoustic cut-off frequency in a sunspot atmosphere. *Astronomy and Astrophysics*, 561:A19.

Zharkov, S., Green, L. M., Matthews, S. A., and Zharkova, V. V. (2011). 2011 February 15: Sunquakes Produced by Flux Rope Eruption. *The Astrophysical Journal Letters*, 741(2):L35.

Zharkova, V. and Zharkov, S. (2015). On the Generation of Hydrodynamic Shocks by Mixed Beams and Occurrence of Sunquakes in Flares. *Solar Physics*, 290(11):3163–3188.

Zharkova, V. V. and Zharkov, S. I. (2007). On the Origin of Three Seismic Sources in the Proton-rich Flare of 2003 October 28. *The Astrophysical Journal*, 664(1):573–585.

Zhugzhda, Y. D. (2007). Three-minute oscillations in sunspots: Seismology of sunspot atmospheres. *Astronomy Letters*, 33(9):622–643.

Zhugzhda, Y. D. (2008). Seismology of a Sunspot Atmosphere. *Solar Physics*, 251(1-2):501–514.

Zweibel, E. G. and Yamada, M. (2009). Magnetic Reconnection in Astrophysical and Laboratory Plasmas. *Annual Review of Astronomy and Astrophysics*, 47(1):291–332.